# AN EFFICIENT ALGORITHM FOR BLADE LOSS SIMULATIONS APPLIED TO A HIGH-ORDER ROTOR DYNAMICS PROBLEM

A Thesis

by

NIKHIL KAUSHIK PARTHASARATHY

Submitted to the Office of Graduate Studies of
Texas A&M University
in partial fulfillment of the requirements for the degree of

MASTER OF SCIENCE

December 2003

Major Subject: Mechanical Engineering

# AN EFFICIENT ALGORITHM FOR BLADE LOSS SIMULATIONS APPLIED TO A HIGH-ORDER ROTOR DYNAMICS PROBLEM

A Thesis

by

NIKHIL KAUSHIK PARTHASARATHY

Submitted to the Office of Graduate Studies of
Texas A&M University
in partial fulfillment of the requirements for the degree of

MASTER OF SCIENCE

Approved as to style and content by:

| | |
|---|---|
| Alan Palazzolo<br>(Chair of Committee) | Chii-Der Suh<br>(Member) |
| Moo-Hyun Kim<br>(Member) | Dennis O'Neal<br>(Interim Department Head) |

December 2003

Major Subject: Mechanical Engineering

# ABSTRACT

An Efficient Algorithm for Blade Loss Simulations
Applied to a High-Order Rotor Dynamics Problem. (December 2003)
Nikhil Kaushik Parthasarathy, B.S., Bangalore University, India
Chair of Advisory Committee: Dr. Alan B. Palazzolo

In this thesis, a novel approach is presented for blade loss simulation of an aircraft gas turbine rotor mounted on rolling element bearings with squeeze film dampers, seal rub and enclosed in a flexible housing. The modal truncation augmentation (MTA) method provides an efficient tool for modeling this large order system with localized nonlinearities in the ball bearings. The gas turbine engine, which is composed of the power turbine and gas generator rotors, is modeled with 38 lumped masses. A nonlinear angular contact bearing model is employed, which has ball and race degrees of freedom and uses a modified Hertzian contact force between the races and balls and for the seal rub. This combines a dry contact force and viscous damping force. A flexible housing with seal rub is also included whose modal description is imported from ANSYS.

Prediction of the maximum contact load and the corresponding stress on an elliptical contact area between the races and balls is made during the blade loss simulations. A finite-element based squeeze film damper (SFD), which determines the pressure profile of the oil film and calculates damper forces for any type of whirl orbit is utilized in the simulation. The new approach is shown to provide efficient and accurate predictions of whirl amplitudes, maximum contact load and stress in the bearings, transmissibility, thermal growths, maximum and minimum damper pressures and the amount of unbalanced force for incipient oil film cavitation. It requires about 4 times less computational time than the traditional approaches and has an error of less than 5 %.

## ACKNOWLEDGMENTS

I would like to thank Dr. Alan Palazzolo for his countless hours of instruction, patience and dedication in my research. My appreciation goes to Dr. Chii-Der Suh and Dr. Moo-Hyun Kim for their guidance and for serving on my advisory committee.

I gratefully acknowledge Andy Provenza, Charles Lawrence and Kelly Carney of NASA – Glenn, Ohio for providing support to this research. I extend my gratitude to the personnel of the Vibration Control and Electromechanics Laboratory, specifically, Dr. Guangyoung Sun, for providing much needed assistance during the course of this investigation.

Last but definitely not least, I would like to especially thank my parents for all their support and encouragement throughout my master's program.

# TABLE OF CONTENTS

## TABLE OF CONTENTS (CONTINUED)

## TABLE OF CONTENTS (CONTINUED)

## LIST OF FIGURES

## LIST OF FIGURES (CONTINUED)

## LIST OF FIGURES (CONTINUED)

## LIST OF FIGURES (CONTINUED)

## LIST OF FIGURES (CONTINUED)

# LIST OF TABLES

# CHAPTER I
# INTRODUCTION

## 1.1 Overview

Today, engineers are becoming increasingly valuable to the manufacturing industry because of their ability to analyze practical machines with the efficiency and accuracy that were not possible just a couple of decades ago. Each year, millions of dollars are saved by the application of computer techniques to aid in the design and in the analysis of turbo machinery for better performance and reliability. The goal of achieving lighter weight construction and higher output power has resulted in more and more flexible rotor and housing support designs. Vibration dynamics in this new breed of machinery is important and must be analyzed with sophisticated analytical tools that are capable of handling computer simulation models consisting of more than a thousand degrees of freedom. In high performance rotating machinery such as gas turbine engine, the design trend has been toward high power output and high efficiency. The requirements for the design trends result in the design of rotors which are lighter, flexible and operating above bending critical speeds.

The most familiar rotor dynamic problem involves the analysis of a single rotor revolving in fluid films or rolling element bearings which are themselves mounted on a rigid foundation. Theoretically, this situation lends itself readily to the solution of the beam equation for the rotating shaft and is conveniently analyzed by methods developed for beam structures. Sometimes, more complex problems are encountered. For example, in aerospace applications, the development of the multi-spool gas turbine engines requires two or more concentrically rotating rotors to be analyzed simultaneously. In some cases, high flexibility in the rotor housing and support system can have a significant effect on the vibration characteristics. Provisions must be given such that the

---

This thesis follows the style and format of the *Journal of Sound and Vibration.*

rotor and the support housing system may be treated together to generate acceptable theoretical results. Therefore, it is rather complex to analyze two rotors rotating at different speeds and interacting through the support system and the intermediate bearings efficiently. An increasing amount of attention for blade loss simulations of aircraft gas turbine engine has been paid because of the increased operating speed and need for reliability demand.

From this motivation, a high fidelity ball bearing and SFD model is applied to blade loss simulation in an aircraft turbine engine. To predict accurate dynamic response of an aircraft turbine engine under high imbalanced load, a good model of a high order flexible dual rotor is necessary in addition to a high fidelity bearing and SFD model. The gas turbine engine, which is composed of the power turbine and gas generator rotors, is modeled with 38 lumped masses. A flexible housing is included whose modal description has been imported into TAMU code from ANSYS. The support system for the rotors is modeled with a high fidelity ball bearing and SFD model, while the intermediate bearings and support bearings for the gas generator rotor are modeled with linear stiffness and damper. There is also a seal rub included in the simulation which protects the bearings from permanent damage. The blade loss simulation results provide the whirl amplitude of the power turbine rotor, contact load and stress in the bearings, transmissibility, SFD pressures and temperature growths of the bearings.

## 1.2 Literature Review

Several methods of analysis are available to tackle these large and complex problems. Perhaps the most widely used technique for general purpose structural analysis is the direct matrix approach in which the structure is divided into a finite number of elements. The equation of motion is developed in matrix form by an assembly of the element mass, stiffness and damping matrices using either a finite element or a discretized mass representation. This matrix equation of motion is then solved directly with high speed digital computers. The use of finite element method in rotor dynamics

was introduced by Ruhl and Booker [1]. Internal damping effects were incorporated into the finite element rotor model by Zorzi and Nelson [2]. However, the direct matrix approach requires large amounts of computer storage and execution time.

A reduction of the system size that the computer has to handle at one time can be accomplished by the component mode approach. In this method, a large structure is partitioned into a number of substructures. The modal information for each individual substructure is derived either analytically or from vibration tests. The structure is reassembled in the modal coordinates by using only a truncated number of modes for each substructure. In a large structure, the potential of this method lies not only in the ability to represent substructures containing thousands of degrees of freedom by a handful of normal modes, but also on the capability that enable analysts to build up accurate analytical model of a complex structure by treating only one portion of the total structure at a time.

Dynamic analysis by component mode synthesis is used extensively in the aerospace industry for the calculation of undamped natural frequencies of large air-frame structures. Hurty [3] and Craig et al. [4] are among the early investigators using this method. The primary emphasis in this analysis is directed towards the matching of the displacements or forces exerting at the connection boundaries that bond the substructures together. To satisfy system continuity at the connections, it requires the substructures to share the common degrees of freedom at these points. Accordingly, a set of constraint equations equal in number to the pairs of common degrees of freedom is derived that expresses the kinematic dependencies among the generalized coordinates relating to the various substructures.

When the total number of degrees of freedom in a complex structure is too large for even modern digital computers to handle economically, recourse is sometimes taken in which a structure is sometimes represented by its vibration modes. The advantage of a modal representation is that only a few of the lower frequency modes are usually required to give a good approximate description of a structure. The assumption is that a dynamic system is unlikely to vibrate in its higher frequency modes because of the

relatively high energy requirement. Thus, with only a few of the vibration modes, the problem size is significantly decreased. Unfortunately, the reduction process alters the modal representation of the applied loading and can adversely affect the quality of the calculated responses. Two methods that attempt to improve the truncated modal representation of the loading are the mode acceleration (MA) and the modal truncation augmentation (MTA) method. The mode acceleration method is used primarily by aerospace engineers for coupled load analyses and has not been used extensively outside of this field of specialization. The modal truncation augmentation method is much newer and is only beginning to be implemented in all fields of structural vibration analysis.

Dickens, Nakagawa and Wittbrodt [5] have compared both the Modal Truncation Augmentation (MTA) method [6] and the Modal Acceleration (MA) method [7] theoretically and numerically, and have concluded that the MTA method is superior to the MA method due to the following reasons: (a) the MA method is an approximation of the MTA method; (b) due to added dynamics, the MTA method gives overall better results than the MA method.

There are few papers, in which blade loss simulations using an aircraft power turbine model with dual rotors were conducted. Stallone, M. J., et al. [8] developed an analytical method based on the modal synthesis to predict the transient response of an aircraft engine when a fan blade is lost and validated their results against experimental data. The analytical tool accounts for rotor-casing rubs, high damping and rapid deceleration rates associated with blade loss events. Alam, M., and Nelson, H. D. [9] presented a shock spectrum procedure to estimate the peak displacement response of linear flexible-rotor systems due to blade loss and applied to three types of rotors including dual-shaft system. However, the detail of time transient responses were not shown, and simple linear stiffness and damping were used for the support system. This thesis attempts to use the MTA method and further modify it to perform an efficient and accurate simulation of a blade loss event on a dual rotor aircraft gas turbine engine with an enhanced support system.

The model for the support system is utilized from Sun [10] which employs a nonlinear angular contact bearing model which has ball and race degrees of freedom and uses a modified Hertzian contact force between the races and balls. A heat transfer network is established and the corresponding thermal equations are derived using thermal resistances and nodes so that the thermal growth is analyzed. The thermal model considers thermal heat sources such as power loss from mechanical contact between high-speed rotor and inner races and from drag torque.

From the literature reviews in the blade loss simulation, it becomes evident that even though rolling element bearings are one of essential components in an aircraft gas turbine rotor-support system, most papers on the numerical analysis for the blade loss simulation have not considered a large order model with a detailed ball bearing and damper model.

## 1.3 Objectives

A blade out event is dramatic, complex and fast moving. In this thesis, physics-based modeling is used to predict the complex interactions between the fan rotor, the high fidelity bearings, and the engine casing during a blade loss. Key objectives of this research include minimizing danger to the aircraft by accurately predicting destructive loads due to the imbalanced load following a blade loss, preventing bearing damage after a blade out event and simulating the response of the overall system in the most computationally efficient manner. The primary problem being addressed is the accurate simulation of a blade-out event in the most efficient manner. Reliable simulations of the loss of a blade are required to ensure structural integrity during flight as well as to guarantee successful blade-out certification testing. The results generated by these analyses are critical for the teams designing several airplane components, including the engine, nacelle, strut, and wing.

In this research, a novel approach is presented for the accurate blade loss simulation of an aircraft gas turbine rotor mounted on high fidelity bearings with finite

element squeeze film dampers, seal rub and enclosed in a flexible casing. The Staggering Analysis scheme implementing the modal truncation augmentation (MTA) method provides an efficient tool for modeling this large order system with localized nonlinearities in the ball bearings. Thus, the objectives for this thesis can be summarized as follows:

- Integrate High Fidelity Bearings with stress, temperature predictions and seal rub into a large order modal based structural model.
- Import the modal description of a flexible housing from any other commercially program like ANSYS, NASTRAN, etc into TAMU code.
- Apply Modal Truncation Augmentation method to high order rotor dynamics problem and compare with other existing methods.
- Validate the Staggering Analysis scheme and implement it to conduct long duration simulations (~ 2 min actual time following blade loss) with temperature prediction.
- Increase computational efficiency for repeated simulation of system dynamics.

## 1.4 Outline

Chapter II introduces the model used in the analysis and develops the fundamentals of the finite element (FE) approach used in this thesis. It describes the Timoshenko beam element in detail and uses it to develop the stiffness matrix, the mass matrix and the gyroscopic damping matrix. The second part of Chapter II describes the gas turbine rotor system, the support system and the FE model of the system used in the initial analysis. The two spool aircraft gas turbine engine is taken as an example to illustrate the accurate and efficient prediction of the blade out event.

In Chapter III, the preliminary structural analyses are performed on the model to help understand the dynamics of the model better. These include the static analysis, the undamped modal analysis, the gyroscopic damped mode shape prediction, the critical

speed analysis and the steady state harmonic analysis. A brief description with the general equations used is provided in this chapter along with the results.

The blade-out response analysis using modal based solution algorithms are described in Chapter IV. The response of a structure can be evaluated using the modal response method which is a relatively simple and well established method. This method reduces the model to a much smaller number of dynamic degrees of freedom. Unfortunately, the reduction process alters the modal representation of the applied loading and can adversely affect the quality of the results. This has been tried to overcome by implementing and comparing three methods viz. Modal Displacement method, Mode Acceleration method and the Modal Truncation Augmentation method. The response is predicted using a non linear equation of motion and two high fidelity bearings at the main power turbine locations. A parametric study is also done to understand the effect of varying unbalanced load on different output parameters.

Chapter V discusses the methodology and implementation of the staggered analysis scheme which would enable efficient prediction of system response for an extended blade loss simulation. This method enhances the advantages of the modal truncation augmentation method by performing intermittent thermal and thermo-mechanical analysis. This method is also validated by comparing it to a standard modal based solution algorithm without any staggering and the results with the time savings are tabulated.

Chapter VI briefly discusses the flexible housing with the undamped modes as it is imported from ANSYS. It also describes the modified Hertzian contact force and equivalent damping used in simulating the seal rub in the model.

In Chapter VII, the FE model of the overall system is discussed in detail and an analysis is performed to simulate the overall system response when a blade is lost on the power turbine. This is done by sudden application of a large unbalanced load at the blade loss location. The simulation includes seal rub, temperature prediction, stress prediction, etc. The results of the simulation are presented with detailed explanations.

The conclusions drawn from the work in this thesis are summarized in Chapter VIII.

# CHAPTER II
# FINITE ELEMENT MODEL OF THE SYSTEM

The requirement of high specific power output for gas turbine engines has resulted in highly flexible rotor designs with rotors typically operating above several critical speeds. The use of rolling element bearings, with low inherent damping, makes it difficult to reduce vibrational amplitudes and dynamic loads transmitted to the rotor supporting structure. Operation over a wide range of speed and power levels aggravates the dynamic problems that are often encountered.

The analysis of an aircraft engine is considerably more complex than that of a conventional turbo rotor. It is complicated by having two rotors which rotate at different speeds and interact through the intermediate differential bearings. Because the motion of one rotor is affected by the other dynamic analysis must be performed on both rotors simultaneously. The two spool aircraft engine is an example of a class of machinery that may be modeled by two rotating shaft structures connected laterally in parallel with each other.

In this chapter, the gas turbine rotor system is described in detail along with the methodology used for modeling the system. The system here refers to the rotating shaft structures with their intermediate bearings and the support system

## 2.1 Evaluation of System Matrices

### 2.1.1 Timoshenko Beam Element

The beam element [11] will be assumed to be a straight bar of uniform cross section capable of resisting axial forces, bending moments about the two principal axes in the plane of its cross section, and twisting moments about its centroidal axis. The following forces are acting on the beam: axial forces $F_1$ and $F_7$; shearing forces $F_2$, $F_3$, $F_8$ and $F_9$; bending moments $F_5$, $F_6$, $F_{11}$ and $F_{12}$; and twisting moments (torques) $F_4$ and $F_{10}$. The location and positive directions of these forces are shown in Fig.2.1. The corresponding displacements $u_1 \ldots u_{12}$ will be taken to be positive in the positive directions of the forces. The position and attitude of the beam element in space will be

specified the co ordinates of the pth end of beam and by the direction cosines of the x axis (pq direction) and the y axis, both taken with respect to some convenient datum system co ordinate system, the latter being required to locate the directions of principal axes of the cross section.

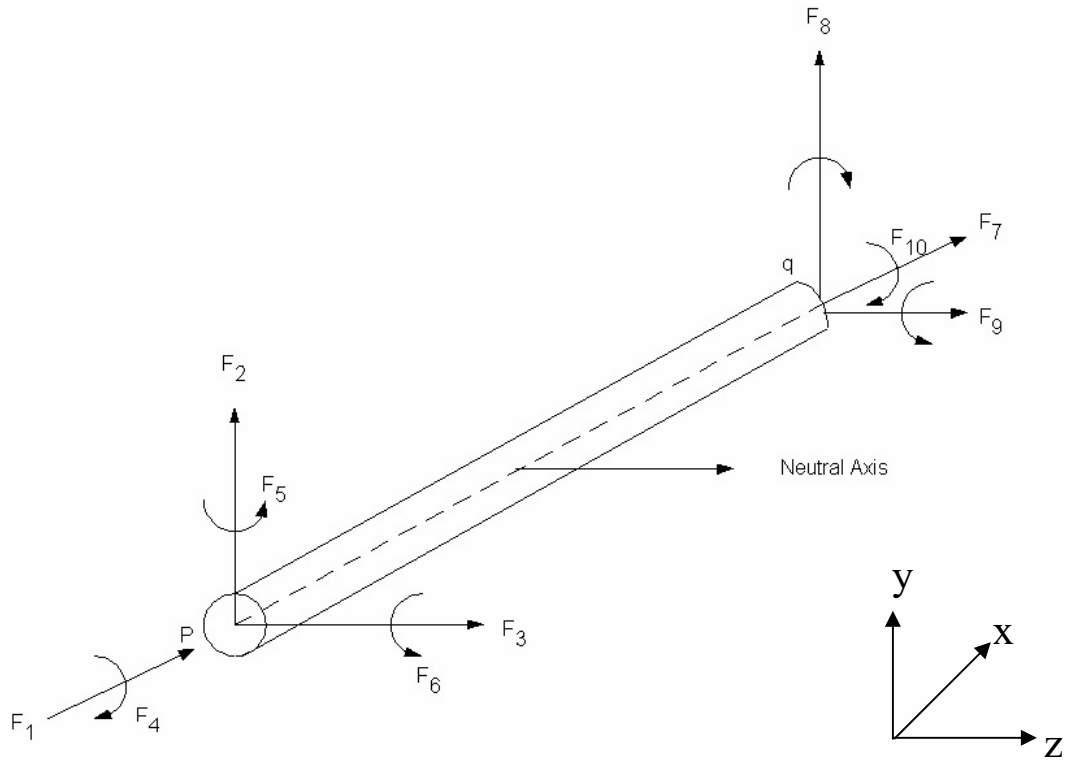


Fig 2.1. Timoshenko beam element

- Axial Forces ($F_1$ and $F_7$)

  The differential equation for the axial displacement *u* of the uniform beam is:

$$F_1 = -\frac{du}{dx} EA \qquad 2.1$$

where E – Modulus of Elasticity

A – Area of cross section

l – length of the element

Integrating directly,

$$F_1 x = -uEA + C_1 \qquad 2.2$$

where $C_1$ is a constant of integration. Assuming that the left end of the beam at x=0 has a displacement $u_1$ while the displacement is zero at x=l,

$$C_1 = F_1 l \qquad 2.3$$

Using Eq. 2.2 and 2.3 for x=0, we get,

$$F_1 = \frac{EA}{l} u_1 \qquad 2.4$$

Also from the equation of equilibrium in the x direction it follows that

$$F_1 = -F_7 \qquad 2.5$$

The individual stiffness coefficients $k_{ij}$ represent the element force $F_i$ due to unit displacement $u_j$ when all other displacements are equal to zero. Hence,

$$k_{1,1} = \left(\frac{F_1}{u_1}\right) = \frac{EA}{l}$$
$$k_{7,1} = \left(\frac{F_7}{u_1}\right) = \frac{-EA}{l} \qquad 2.6$$

while all other coefficients in the first column of the stiffness matrix are equal to zero. Similarly, if $u_1 = 0$ and we allow $u_7$ to be non zero, it can be shown from symmetry that

$$k_{7,7} = \frac{EA}{l} \qquad 2.7$$

- Twisting Moments ($F_4$ and $F_{10}$)

  The differential equation for the twist θ on the beam is

$$F_4 = -GJ \frac{d\theta}{dx} \qquad 2.8$$

where G – Shear Modulus

J – Torsional Moment of Inertia = $\int_A (y^2 + z^2) dA$

Integrating Eq. 2.8, we get

$$F_4 x = -GJ\theta + C_1 \qquad 2.9$$

and then by using the boundary condition θ = 0 at x = l we find that the constant of integration is given by

$$C_1 = F_4 l \tag{2.10}$$

Since θ = $u_1$ at x = 0, it follows from Eq. 2.9 and 2.10 that

$$F_4 = \frac{GJ}{l} u_4 \tag{2.11}$$

Using the equilibrium conditions for the twisting moments, we have

$$F_{10} = -F_4 \tag{2.12}$$

Hence,

$$k_{4,4} = \frac{F_4}{u_4} = \frac{GJ}{l} \tag{2.13}$$

$$k_{10,4} = \frac{F_{10}}{u_4} = \frac{-GJ}{l} \tag{2.14}$$

while all other co-efficients in the fourth column of k are equal to zero. Similarly, if $u_4$ = 0 it can be demonstrated that

$$k_{10,10} = \frac{GJ}{l} \tag{2.15}$$

- Shearing Forces ($F_2$ and $F_8$)

The lateral deflection $v$ on the beam subjected to shearing forces and associated moments is given by:

$$v = v_b + v_s \tag{2.16}$$

where $v_b$ is the lateral deflection due to bending strains and $v_s$ is the additional deflection due to shearing strains, such that:

$$\frac{dv_s}{dx} = \frac{-F_2}{GA_s} \tag{2.17}$$

with $A_s$ representing the beam cross sectional area effective in shear. The bending deflection for the beam held rigid at the right hand side is governed by the differential equation

$$EI \ \frac{d^2 v_b}{dx^2} = F_2 x - F_6 \tag{2.18}$$

where I – Normal Shear Area

It has been assumed that the cross section has the same properties about the z and the y axes. Thus I is given by

$$I = \frac{A}{K} \tag{2.19}$$

where the shear co-efficient K is defined as [12]

$$K = \frac{(7+6\mu)(1+(r_i/r_o)^2)^2 + (20+12\mu)(r_i/r_o)^2}{6(1+\mu)(1+(r_i/r_o)^2)^2} \tag{2.20}$$

where μ - Poisson's Ratio

$\frac{r_i}{r_o}$ - Ratio of inner radius to outer radius

From integration of Eq. 2.17 and 2.18, it follows that

$$EI\ v = \frac{F_2 x^3}{6} - \frac{F_6 x^2}{2} + C_2 + \left(C_1 - \frac{F_2 EI}{GA_s}\right)x \tag{2.21}$$

where $C_1$ and $C_2$ are the constants of integration. Using the boundary conditions,

$$\frac{dv}{dx} = \frac{dv_s}{dx} = \frac{-F_2}{GA_s} \text{ at } x=0,\ x=l \tag{2.22}$$

$$v=0 \text{ at } x=l \tag{2.23}$$

Eq. 2.21 becomes

$$EIv = \frac{F_2 x^3}{6} - \frac{F_6 x^2}{2} - \frac{F_2 \Phi x l^2}{12} + (1+\Phi)\frac{l^3 F_2}{12} \tag{2.24}$$

where $F_6 = \frac{F_2 l}{2}$ 2.25

and $\Phi = \frac{12EI}{GA_s l^2}$ 2.26

The remaining forces acting on the beam can be determined from the equations of equilibrium.

$$F_8 = -F_2 \tag{2.27}$$

and $F_{12} = -F_6 + F_2 l$ 2.28

Now at $x = 0,\ v = u_2$ and hence from Eq. 2.24

$$u_2 = (1+\Phi)\frac{l^3 F_2}{12EI} \tag{2.29}$$

Using Eqs. 2.25 and 2.27 to 2.29, we have

$$k_{2,2} = \frac{F_2}{u_2} = \frac{12EI}{(1+\Phi)l^3} \tag{2.30}$$

$$k_{6,2} = \frac{F_6}{u_2} = \frac{F_2 l}{2u_2} = \frac{6EI}{(1+\Phi)l^2} \tag{2.31}$$

$$k_{8,2} = \frac{F_8}{u_2} = \frac{-12EI}{(1+\Phi)l^3} \tag{2.32}$$

$$k_{12,2} = \frac{F_{12}}{u_2} = \left(\frac{-F_6 + F_2 l}{u_2}\right) = \frac{6EI}{(1+\Phi)l^2} \tag{2.33}$$

while the remaining co-efficients in the second column are equal to zero.

Similarly, if the left hand side of the beam is fixed, it can be shown from symmetry that

$$\begin{aligned} k_{8,8} &= k_{2,2} \\ k_{12,8} &= -k_{6,2} \end{aligned} \tag{2.34}$$

- Bending Moments ($F_6$ and $F_{12}$)

In order to determine the stiffness co-efficients associated with the rotations $u_6$ and $u_{12}$, the beam is subjected to bending moments and associated shears. The deflections can be determined from Eq. 2.21, but the constants $C_1$ and $C_2$ in these equations must be evaluated from a different set of boundary conditions which are:

$$v = 0 \text{ at } x=0,\ x=l \tag{2.35}$$

and

$$\frac{dv}{dx} = \frac{dv_s}{dx} = -\frac{F_2}{GA_s} \text{ at } x=l \tag{2.36}$$

Eq. 2.21 becomes

$$\begin{aligned} EIv &= \frac{F_2}{6}(x^3 - l^2 x) + \frac{F_6}{2}(lx - x^2) \\ F_2 &= \frac{6F_6}{(4+\Phi)l} \end{aligned} \tag{2.37}$$

As before, the remaining forces acting on the beam can be determined from the equations of equilibrium, i.e., Eq. 2.27 and 2.28. Now at $x=0$

$$\frac{dv_b}{dx} = \frac{dv}{dx} - \frac{dv_s}{dx} = u_6 \tag{2.38}$$

so that

$$u_6 = \frac{F_6(1+\Phi)l}{EI(4+\Phi)} \qquad 2.39$$

Hence, from Eqs. 2.27, 2.28, 2.37 to 2.39,

$$\begin{aligned} k_{6,6} &= \frac{F_6}{u_6} = \frac{(4+\Phi)EI}{(1+\Phi)l} \\ k_{8,6} &= \frac{F_8}{u_6} = \frac{-F_2}{u_6} = -\frac{6EI}{(1+\Phi)l^2} \\ k_{12,6} &= \frac{F_{12}}{u_6} = \left(\frac{-F_6 + F_2 l}{u_6}\right) = \frac{(2-\Phi)EI}{(1+\Phi)l} \end{aligned} \qquad 2.40$$

If the deflection of the left hand end of the beam is equal to zero, it is evident from symmetry that

$$k_{12,12} = k_{6,6} \qquad 2.41$$

- Shearing Forces ($F_3$ and $F_9$)

The stiffness co-efficients associated with the displacements $u_3$ and $u_9$ can be derived directly from previous results. It should be observed, however, that with the sign convention adopted in Fig. 2.1 the directions of the positive bending moments in the yx and zx planes are different. Therefore

$$\begin{aligned} k_{3,3} &= k_{2,2} \\ k_{5,3} &= -k_{6,2} \\ k_{9,3} &= k_{8,2} \\ k_{11,3} &= -k_{12,2} \\ k_{9,9} &= k_{8,8} \\ k_{11,9} &= -k_{12,8} \end{aligned} \qquad 2.42$$

- Bending Moments ($F_5$ and $F_{11}$)

Here the same remarks apply as in the preceding section; thus we have

$$\begin{aligned} k_{5,5} &= k_{6,6} \\ k_{9,5} &= -k_{8,6} \\ k_{11,5} &= k_{12,6} \end{aligned} \qquad 2.43$$

2.1.2 Stiffness Matrix

The results obtained in the previous sub sections can now be compiled into a matrix equation relating the element forces to their corresponding displacements i.e. **{F}=[K]{u}**. The stiffness matrix from this relationship is given by

$$K = \begin{bmatrix} \frac{AE}{L} & 0 & 0 & 0 & 0 & 0 & -\frac{AE}{L} & 0 & 0 & 0 & 0 & 0 \\ 0 & a & 0 & 0 & 0 & c & 0 & b & 0 & 0 & 0 & c \\ 0 & 0 & a & 0 & d & 0 & 0 & 0 & b & 0 & d & 0 \\ 0 & 0 & 0 & \frac{GJ}{L} & 0 & 0 & 0 & 0 & 0 & -\frac{GJ}{L} & 0 & 0 \\ 0 & 0 & d & 0 & e & 0 & 0 & 0 & c & 0 & f & 0 \\ 0 & c & 0 & 0 & 0 & e & 0 & d & 0 & 0 & 0 & f \\ -\frac{AE}{L} & 0 & 0 & 0 & 0 & 0 & \frac{AE}{L} & 0 & 0 & 0 & 0 & 0 \\ 0 & b & 0 & 0 & 0 & d & 0 & a & 0 & 0 & 0 & d \\ 0 & 0 & b & 0 & c & 0 & 0 & 0 & a & 0 & c & 0 \\ 0 & 0 & 0 & -\frac{GJ}{L} & 0 & 0 & 0 & 0 & 0 & \frac{GJ}{L} & 0 & 0 \\ 0 & 0 & d & 0 & f & 0 & 0 & 0 & c & 0 & e & 0 \\ 0 & c & 0 & 0 & 0 & f & 0 & d & 0 & 0 & 0 & e \end{bmatrix} \quad 2.44$$

where

$$a = \frac{12EI}{L^3(1+\Phi)} = -b$$

$$c = \frac{6EI}{L^2(1+\Phi)} = -d \quad 2.45$$

$$e = \frac{(4+\Phi)EI}{L\ (1+\Phi)}$$

$$f = \frac{(2-\Phi)EI}{L\ (1+\Phi)}$$

2.1.3 Mass Matrix

- Consistent Mass Matrix

The mass matrix M derived from the weighted integral formulation of the governing equation is called the consistent mass matrix, and it is symmetric, positive definite and non diagonal. The components of the mass matrix are usually of the form

$$M_{ij} = \int N_i \rho N_j d\Omega \qquad 2.46$$

where N is the shape function and ρ the density. Calculating and assembling these components, we get

$$M = \begin{bmatrix}
\rho AL/3 & & & & & & & & & & & \\
0 & a & & & & & & & & & & \\
0 & 0 & a & & & & & S & Y & M & & \\
0 & 0 & 0 & \rho JL/3 & & & & & & & & \\
0 & 0 & b & 0 & c & & & & & & & \\
0 & b & 0 & 0 & 0 & c & & & & & & \\
\rho AL/6 & 0 & 0 & 0 & 0 & 0 & \rho AL/3 & & & & & \\
0 & d & 0 & 0 & 0 & e & 0 & a & & & & \\
0 & 0 & d & 0 & e & 0 & 0 & 0 & a & & & \\
0 & 0 & 0 & \rho JL/6 & 0 & 0 & 0 & 0 & 0 & \rho JL/3 & & \\
0 & 0 & -e & 0 & f & 0 & 0 & 0 & -b & 0 & c & \\
0 & -e & 0 & 0 & 0 & f & 0 & -b & 0 & 0 & 0 & c
\end{bmatrix} \qquad 2.47$$

Where

$$\begin{aligned}
a &= \Psi_m^u * 156 + \Psi_m^\theta * 36 \\
b &= \Psi_m^u * 22L + \Psi_m^\theta * 3L \\
c &= \Psi_m^u * 4L^2 + \Psi_m^\theta * 4L^2 \\
d &= \Psi_m^u * 54 - \Psi_m^\theta * 36 \\
e &= \Psi_m^u * 13L - \Psi_m^\theta * 3L \\
f &= -\Psi_m^u * 3L^2 - \Psi_m^\theta * L^2 \\
\Psi_m^u &= \rho AL/420 \\
\Psi_m^\theta &= \rho I /30L
\end{aligned} \qquad 2.48$$

in the transverse direction.

- Lumped Mass Matrix

Diagonal mass matrices are known as Lumped Mass Matrices. The use of a lumped mass matrix in a transient analysis saves computational time in two ways. First, for forward difference schemes, lumped mass matrices result in explicit algebraic equations, not requiring matrix inversions. Second, the critical time step required for conditionally stable schemes is larger, and hence less computational time is required when lumped mass matrices are used. The lumped mass matrix for the Timoshenko Beam element is given by:

$$M = \frac{1}{2}\begin{bmatrix} Mt & 0 & 0 & 0 & 0 & 0 & 0 & 0 & 0 & 0 & 0 & 0 \\ 0 & Mt & 0 & 0 & 0 & 0 & 0 & 0 & 0 & 0 & 0 & 0 \\ 0 & 0 & Mt & 0 & 0 & 0 & 0 & 0 & 0 & 0 & 0 & 0 \\ 0 & 0 & 0 & Ip & 0 & 0 & 0 & 0 & 0 & 0 & 0 & 0 \\ 0 & 0 & 0 & 0 & It & 0 & 0 & 0 & 0 & 0 & 0 & 0 \\ 0 & 0 & 0 & 0 & 0 & It & 0 & 0 & 0 & 0 & 0 & 0 \\ 0 & 0 & 0 & 0 & 0 & 0 & Mt & 0 & 0 & 0 & 0 & 0 \\ 0 & 0 & 0 & 0 & 0 & 0 & 0 & Mt & 0 & 0 & 0 & 0 \\ 0 & 0 & 0 & 0 & 0 & 0 & 0 & 0 & Mt & 0 & 0 & 0 \\ 0 & 0 & 0 & 0 & 0 & 0 & 0 & 0 & 0 & Ip & 0 & 0 \\ 0 & 0 & 0 & 0 & 0 & 0 & 0 & 0 & 0 & 0 & It & 0 \\ 0 & 0 & 0 & 0 & 0 & 0 & 0 & 0 & 0 & 0 & 0 & It \end{bmatrix} \qquad 2.49$$

where

A – cross sectional area

L – Elemental length

$Mt = \rho AL$

Ip – Mass Moment of Inertia in the axial x direction

It – Mass Moment of Inertia in the transverse y or z directions

2.1.4 Damping Matrix

The Damping matrix is a sum of the structural damping matrix, $[C_b]$ and the gyroscopic damping matrix, [G].

$$[C] = [C_b] + [G] \qquad 2.50$$

- Gyroscopic Damping Matrix

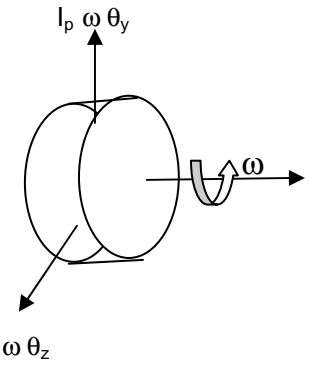


Fig. 2.2 Gyroscopic moments

The gyroscopic matrix for an axi symmetric rigid body rotating about its axis of symmetry, (assumed to be the x-axis) as shown in fig. 2.2 is:

$$G = \begin{bmatrix} 0 & 0 & 0 & 0 & 0 & 0 \\ 0 & 0 & 0 & 0 & 0 & 0 \\ 0 & 0 & 0 & 0 & 0 & 0 \\ 0 & 0 & 0 & 0 & 0 & 0 \\ 0 & 0 & 0 & 0 & 0 & I_p\omega \\ 0 & 0 & 0 & 0 & -I_p\omega & 0 \end{bmatrix} \qquad 2.51$$

where,

$I_p$ - Polar Moment of Inertia about the axis of spin

ω – Speed of rotation about the x-axis

This is a skew symmetric matrix, i.e. $G^T = -G$.

## 2.2 Description of the Dual Rotor System

### 2.2.1 Description of the Gas Turbine Rotor System

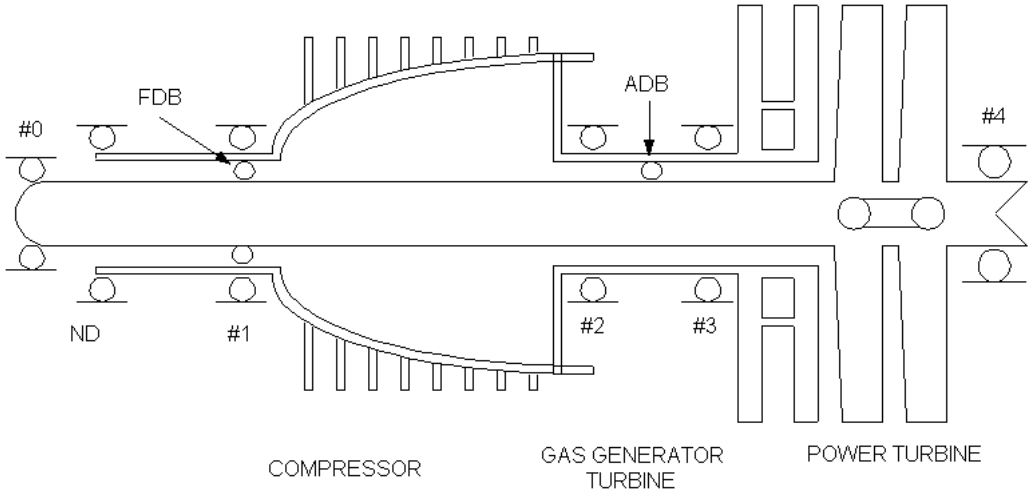


Fig. 2.3 Two spool aircraft turbine engine with 8 bearings

Figure 2.3 represents a schematic drawing of the two-spool gas turbine engine [13] used in this analysis. The basic engine consists of an inner core rotor called the power turbine, which is supported by two main bearings located at shaft extremities. There are two intermediate differential bearings connecting the core power turbine to the gas generator rotor. The gas generator rotor consists of a two stage generator turbine which drives an axial compressor. It is supported principally by rolling element bearings at four locations. The typical operating speed for the gas generator is 15,000 RPM and the power turbine is 16,000 RPM.

### 2.2.2 Support System

A nonlinear angular contact bearing model is employed, which has ball and race degrees of freedom and uses a modified Hertzian contact force between the races and balls. This combines a dry contact force and an equivalent viscous damping force. Prediction of the maximum contact load and the corresponding stress on an elliptical contact area between the races and balls is made during the blade loss simulations. A finite-element based squeeze film damper (SFD), which determines the pressure profile of oil film and calculates damper forces for any type of whirl orbit is utilized in the

simulations. Thermal growths during blade loss in the support bearings and SFD oil film of the gas turbine engine are also estimated.

### 2.2.3 FE Model of Complete System

The computer model shown in Fig. 2.4 has a total of 38 lumped masses (for the rotors) with power turbine divided up into 22 nodes and the gas generator divided up into 16 nodes. Each node is allowed to have 3 translational and 3 rotational degrees of freedom. The system has a total of 228 degrees of freedom. Polar moments of inertia in the rotors are considered only at the turbine and compressor stages. The bearings #0 and #4 are modeled as high fidelity bearings, while four bearings in the gas generator and two intermediate differential bearings are modeled with simple linear stiffness and dampers. The arrows on Fig. 2.4 indicate the locations of imbalanced load. Both the imbalanced loads are out of phase by $180^0$.

Tables 2.1 and 2.2 show the physical and cross-sectional properties of the power rotor and the gas generator rotor respectively.

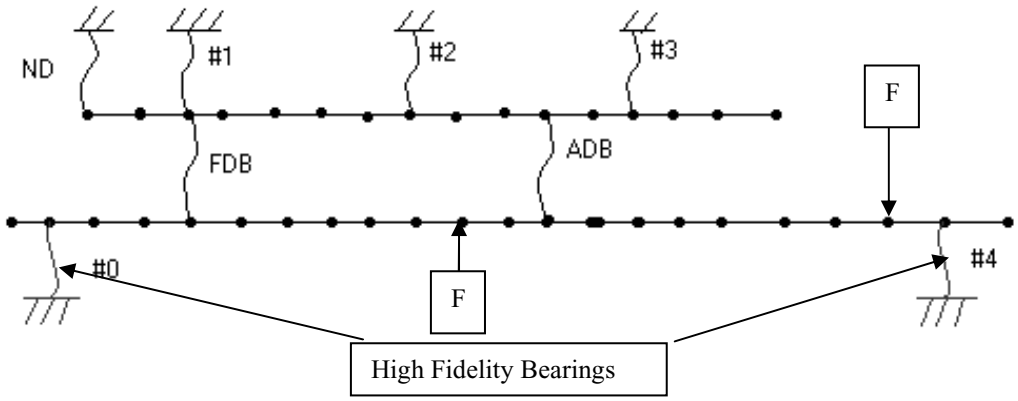


Fig. 2.4 Two spool aircraft turbine engine lumped parameter FE model

Table 2.1 Lumped Parameters and Cross-Sectional Properties of the Power Turbine Rotor

| Station No. | Weight (lb) | Length (in) | Shaft dia out | Shaft dia in | I (in^4) | Ip Lb-in^2 | It Lb-in^2 | E*10-6 (lb/in^2) |
|---|---|---|---|---|---|---|---|---|
| 1 | 0.740 | 1.3 | 2.00 | 1.53 | 0.52 | 0.0 | 0.129 | 30.0 |
| 2 | 1.539 | 1.3 | 2.10 | 1.53 | 0.69 | 0.0 | 0.297 | 30.0 |
| 3 | 1.989 | 3.0 | 2.10 | 1.53 | 0.69 | 0.0 | 0.977 | 30.0 |
| 4 | 1.679 | 4.3 | 2.10 | 1.53 | 0.69 | 0.0 | 2.749 | 30.0 |
| 5 | 2.082 | 4.8 | 2.30 | 1.80 | 0.86 | 0.0 | 4.623 | 30.0 |
| 6 | 2.187 | 4.8 | 2.30 | 1.80 | 0.86 | 0.0 | 5.365 | 30.0 |
| 7 | 1.851 | 4.4 | 1.80 | 1.30 | 0.38 | 0.0 | 4.139 | 30.0 |
| 8 | 1.516 | 4.4 | 1.80 | 1.30 | 0.38 | 0.0 | 2.913 | 30.0 |
| 9 | 1.120 | 2.1 | 1.80 | 1.30 | 0.38 | 0.0 | 1.701 | 30.0 |
| 10 | 0.896 | 3.1 | 1.80 | 1.30 | 0.38 | 0.0 | 0.837 | 30.0 |
| 11 | 0.896 | 2.1 | 1.80 | 1.30 | 0.38 | 0.0 | 0.837 | 30.0 |
| 12 | 0.723 | 2.1 | 1.80 | 1.30 | 0.38 | 0.0 | 0.489 | 30.0 |
| 13 | 1.429 | 2.0 | 2.60 | 1.40 | 2.05 | 0.0 | 1.181 | 30.0 |
| 14 | 2.187 | 2.1 | 2.60 | 1.40 | 2.05 | 0.0 | 1.959 | 30.0 |
| 15 | 2.027 | 1.7 | 2.60 | 1.40 | 2.05 | 0.0 | 1.735 | 30.0 |
| 16 | 1.387 | 0.9 | 2.60 | 1.40 | 2.05 | 0.0 | 1.007 | 30.0 |
| 17 | 1.173 | 2.4 | 2.25 | 1.57 | 0.96 | 0.0 | 0.953 | 30.0 |
| 18 | 1.386 | 2.4 | 2.25 | 1.57 | 0.96 | 0.0 | 1.317 | 30.0 |
| 19 | 26.501 | 2.8 | 2.25 | 1.57 | 0.96 | 625.0 | 314.067 | 30.0 |
| 20 | 31.028 | 2.0 | 1.80 | 1.50 | 0.27 | 704.5 | 353.257 | 30.0 |
| 21 | 2.660 | 1.5 | 3.30 | 1.50 | 5.57 | 0.0 | 1.602 | 30.0 |
| 22 | 1.440 | 0.0 | 0.00 | 0.00 | 0.00 | 0.0 | 1.453 | 0.0 |

Table 2.2 Lumped Parameters and Cross-Sectional Properties of the Gas Generator Rotor

| Station No. | Weight (lb) | Length (in) | Shaft dia outside | Shaft dia inside | I (in^4) | Ip (lb – in^2) | It (lb-in^2) | E*10-6 Lb/in^2 |
|---|---|---|---|---|---|---|---|---|
| 23 | 0.693 | 3.0 | 2.80 | 2.40 | 1.39 | 0.0 | 1.110 | 30.0 |
| 24 | 2.270 | 4.3 | 3.05 | 2.45 | 2.48 | 0.0 | 5.048 | 30.0 |
| 25 | 9.389 | 4.8 | 11.00 | 10.97 | 7.81 | 111.0 | 65.417 | 30.0 |
| 26 | 13.514 | 4.8 | 11.00 | 10.86 | 35.90 | 297.5 | 182.243 | 15.0 |
| 27 | 7.600 | 4.4 | 11.00 | 10.79 | 53.33 | 301.5 | 215.078 | 12.8 |
| 28 | 11.404 | 4.4 | 11.00 | 10.66 | 35.90 | 232.0 | 177.576 | 19.3 |
| 29 | 3.126 | 2.1 | 3.85 | 2.80 | 7.77 | 117.0 | 86.170 | 27.3 |
| 30 | 2.691 | 3.1 | 3.39 | 2.90 | 3.01 | 0.0 | 5.078 | 30.0 |
| 31 | 1.697 | 2.1 | 3.60 | 3.20 | 3.10 | 0.0 | 3.325 | 30.0 |
| 32 | 1.270 | 2.1 | 3.60 | 3.20 | 3.10 | 0.0 | 2.307 | 30.0 |
| 33 | 1.239 | 2.0 | 3.60 | 3.20 | 3.10 | 0.0 | 2.232 | 30.0 |
| 34 | 1.010 | 2.1 | 3.60 | 3.35 | 2.08 | 0.0 | 1.840 | 30.0 |
| 35 | 0.872 | 1.7 | 3.70 | 3.35 | 3.02 | 0.0 | 1.600 | 30.0 |
| 36 | 1.108 | 0.9 | 4.20 | 3.35 | 9.09 | 0.0 | 2.039 | 30.0 |
| 37 | 27.605 | 2.4 | 9.40 | 9.00 | 61.19 | 612.5 | 329.123 | 30.0 |
| 38 | 26.963 | 0.0 | 0.00 | 0.00 | 0.00 | 600.0 | 321.721 | 30.0 |

# CHAPTER III
# PRELIMINARY STRUCTURAL ANALYSES

The preliminary structural analyses are performed using the full system structural matrices. The various types of analyses performed and the respective equations used for them are given below.

## 3.1 Static Analysis

The equation of equilibrium for static analyses can be written as:

$$[K]\{Q\}=\{F\} \qquad 3.1$$

where,

[K] – System stiffness matrix

{F} – Static input force vector

{Q} – Static deflection vector

The following load case was run for the static analysis:

- Case 1: 100 lb force acting in the positive y direction at bearing #4

Table 3.1: Static Analysis Displacements in y Direction

| Location | Full Model without reduction (inches) |
|---|---|
| #0 Bearing | 9.5337 E-5 |
| Rotor Mid Span | 6.8703 E-5 |
| Second Stage Power Turbine | 0.0027 |
| #4 Bearing | 0.0030 |

- Case 2: 25 lb force acting downwards on the power turbine mid span

Table 3.2: Static Analysis Displacements in y Direction

| Location | Full Model without reduction (inches) |
|---|---|
| #0 Bearing | -6.9808 E-5 |
| Rotor Mid Span | 6.4124 E-4 |
| Second Stage Power Turbine | 6.5092 E-4 |
| #4 Bearing | 6.3262 E-4 |

## 3.2 Undamped Modal Analysis

Undamped normal mode frequencies and vectors are extracted by means of the following equations:

$$([K] - \omega^2 [M])[\Phi] = 0 \qquad 3.2$$

where,

[M] - System mass matrix

[Φ] - Eigen vector matrix

ω - Normal mode frequencies

The gyroscopic and damping matrices are ignored for this analysis. The modes of each of the rotors and the casing were obtained independently of each other by omitting the effects of disk gyroscopics and the intermediate bearings. The undamped normal mode shapes below 110,000 RPM are presented here. This covers the range up to about 6 times the top operating speeds of the rotors.

### 3.2.1 Gas Generator Rotor Undamped Modes

Figures 3.1 to 3.5 show the first five gas generator modes.

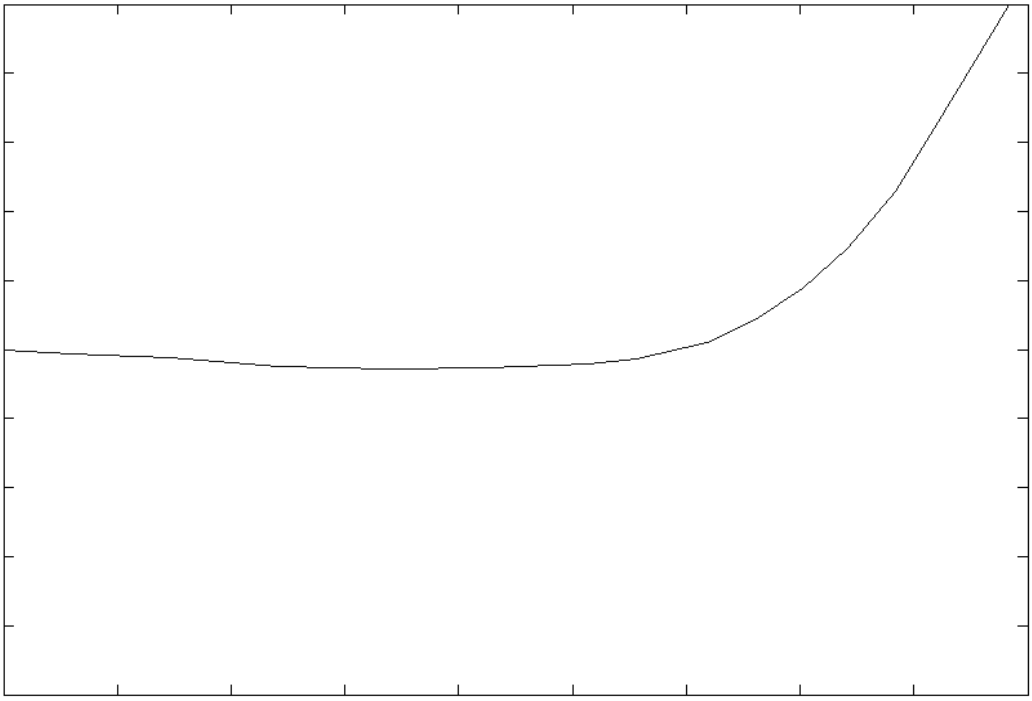

Fig 3.1 Gas generator undamped mode at N = 10,421 RPM

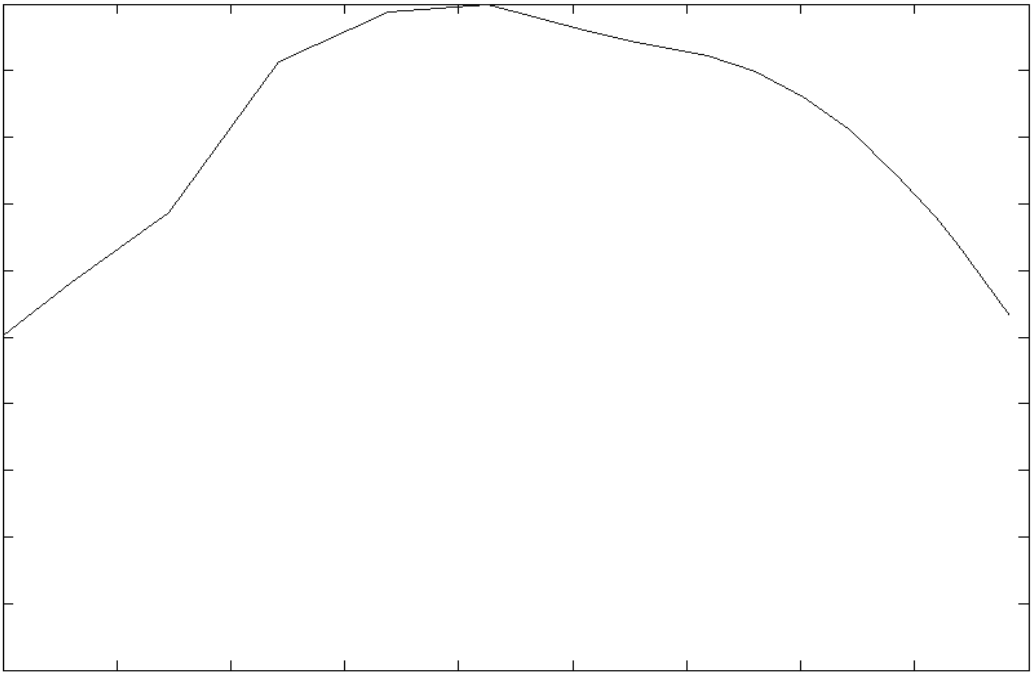

Fig 3.2 Gas generator undamped mode at N = 25,902 RPM

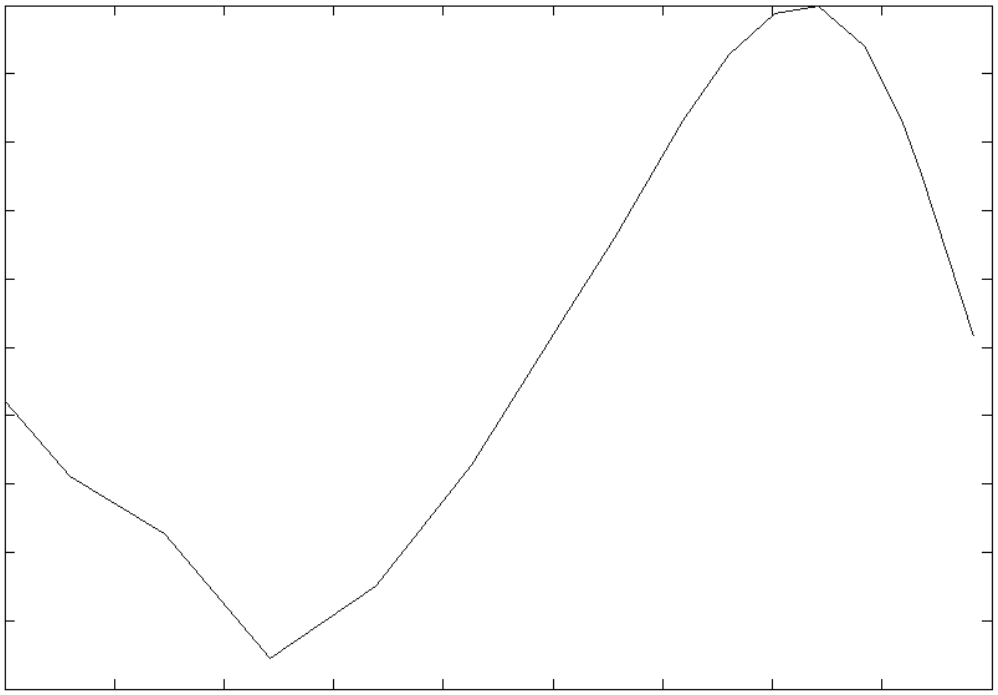

Fig 3.3 Gas generator undamped mode at N = 34,685 RPM

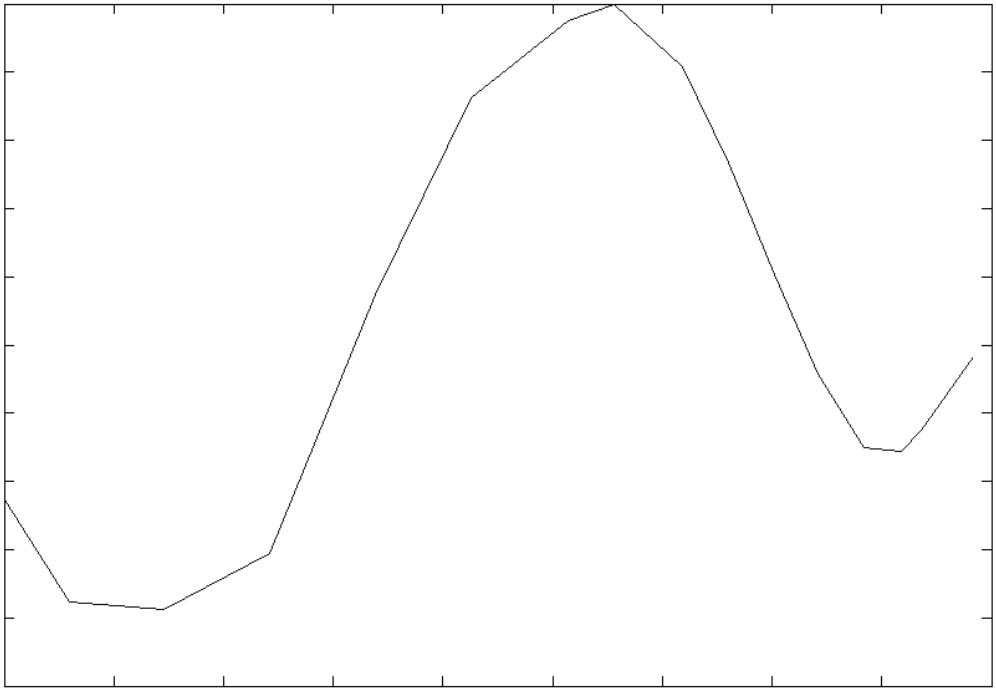

Fig 3.4 Gas generator undamped mode at N = 58570 RPM

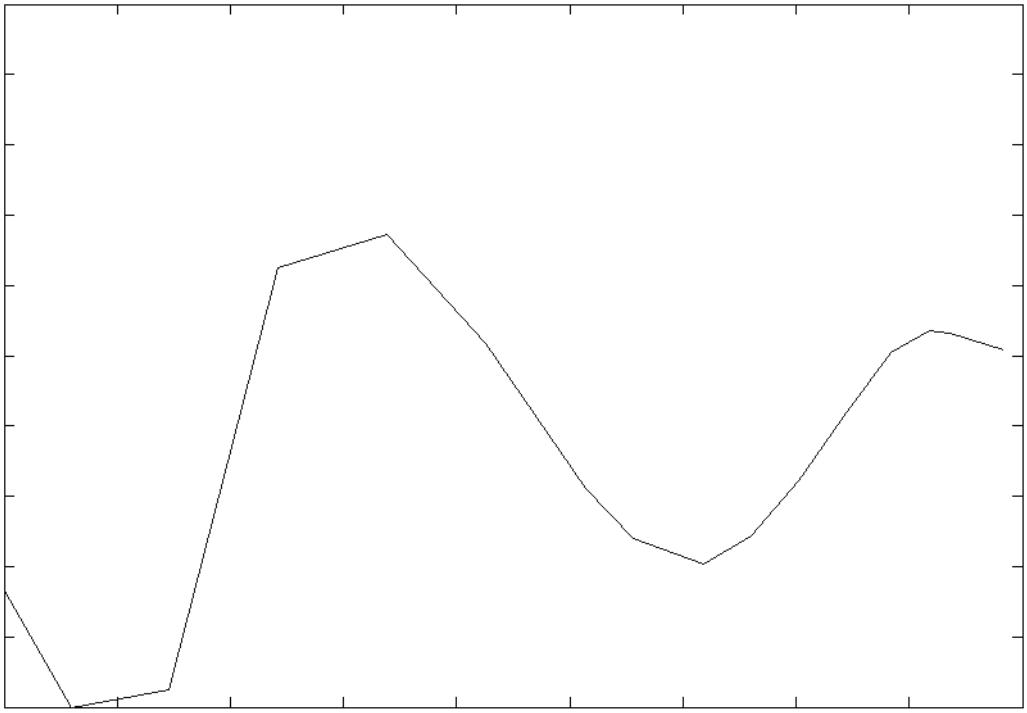

Fig 3.5 Gas generator undamped mode at N = 92,049 RPM

### 3.2.2 Power Turbine Rotor Undamped Modes

Figures 3.6 to 3.14 show the first nine power turbine modes. It is clear from the value of the frequency that the gas generator is stiffer than the power turbine.

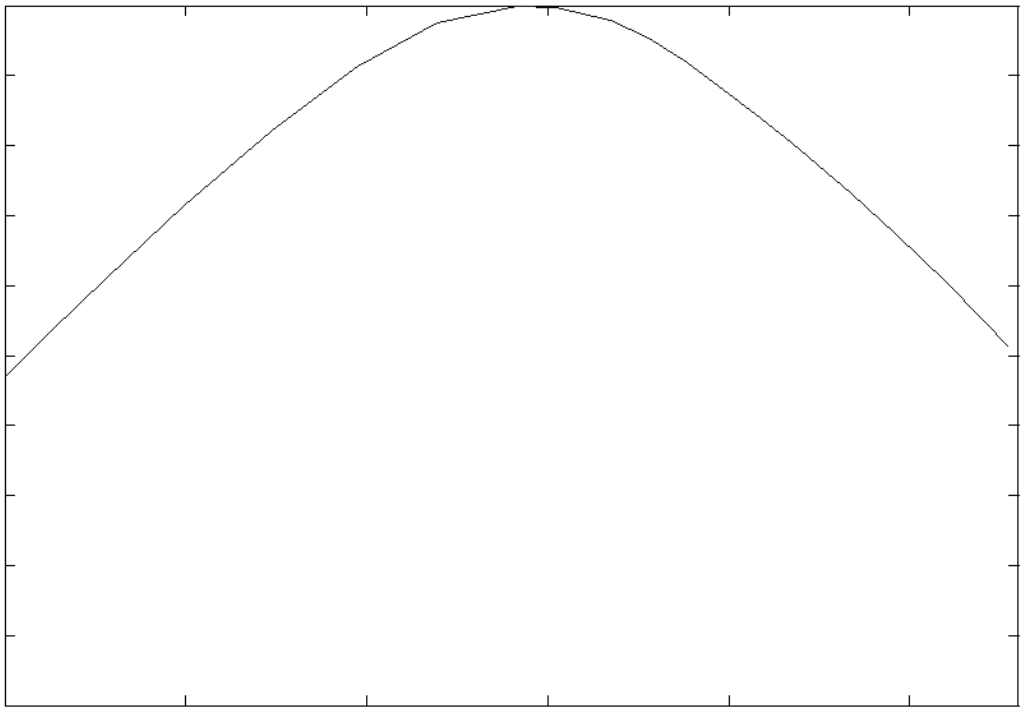

Fig 3.6 Power turbine undamped mode at N = 3080 RPM

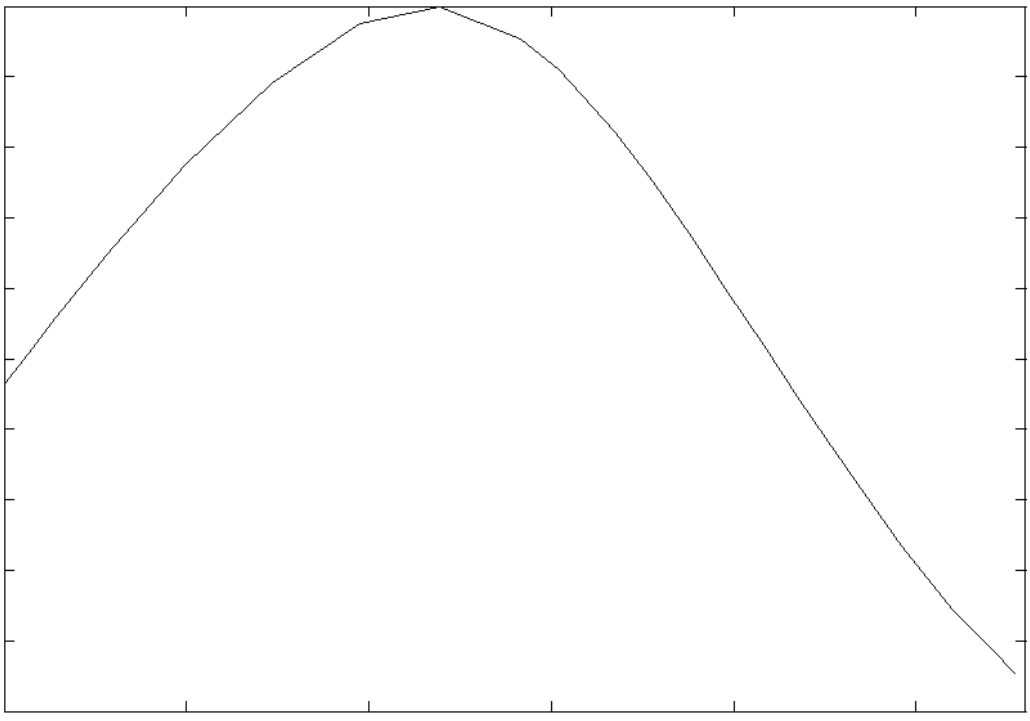

Fig 3.7 Power turbine undamped mode at N = 6943 RPM

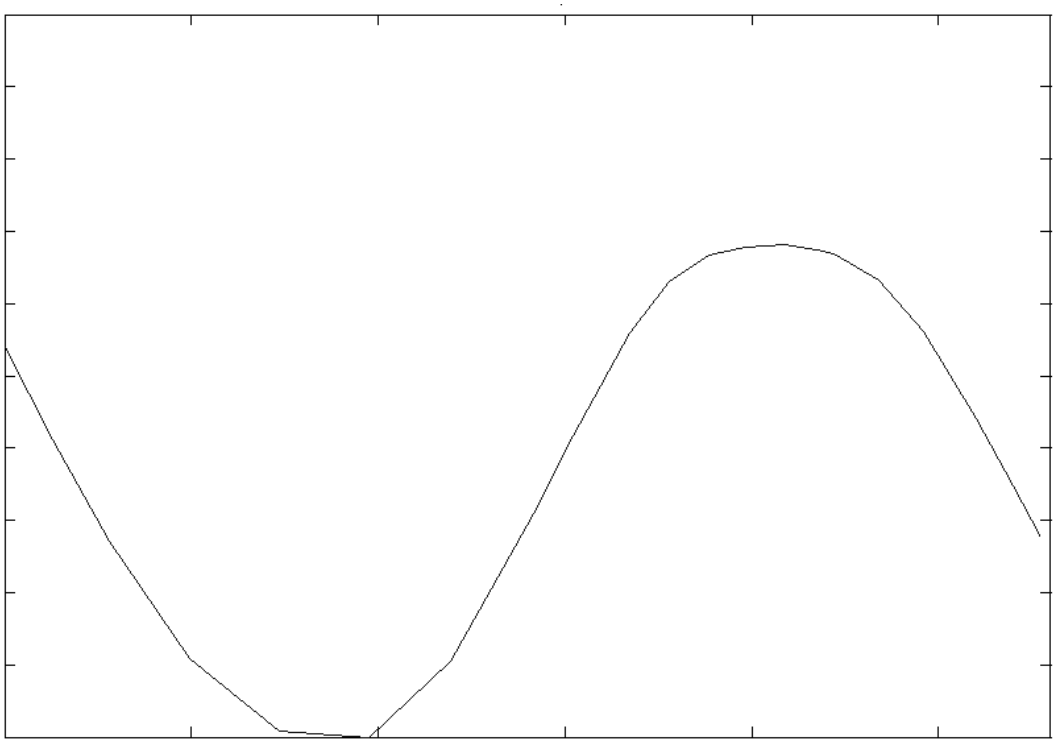

Fig 3.8 Power turbine undamped mode at N = 14,370 RPM

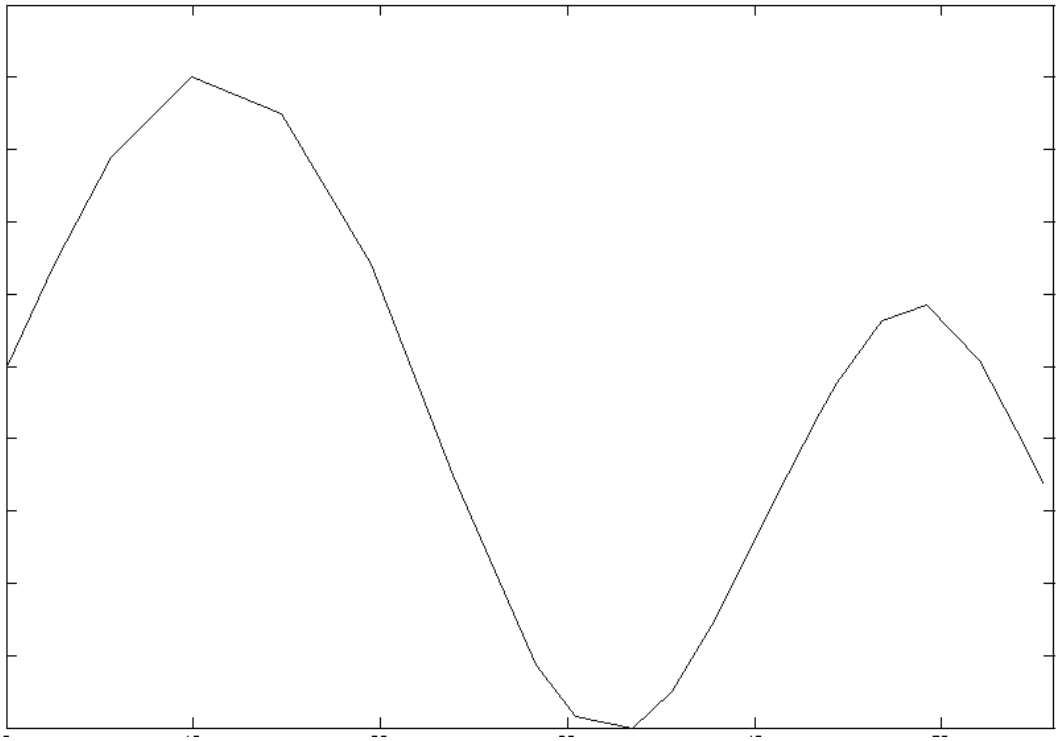

Fig 3.9 Power turbine undamped mode at N = 27,563 RPM

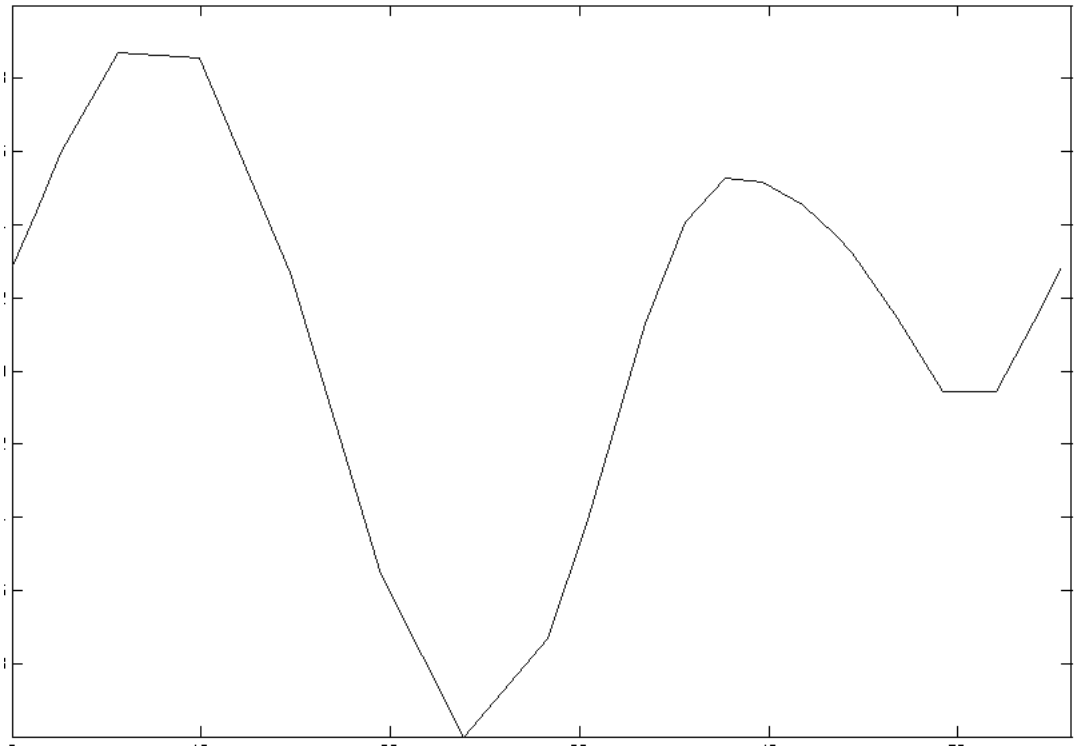

Fig 3.10 Power turbine undamped mode at N = 43,676 RPM

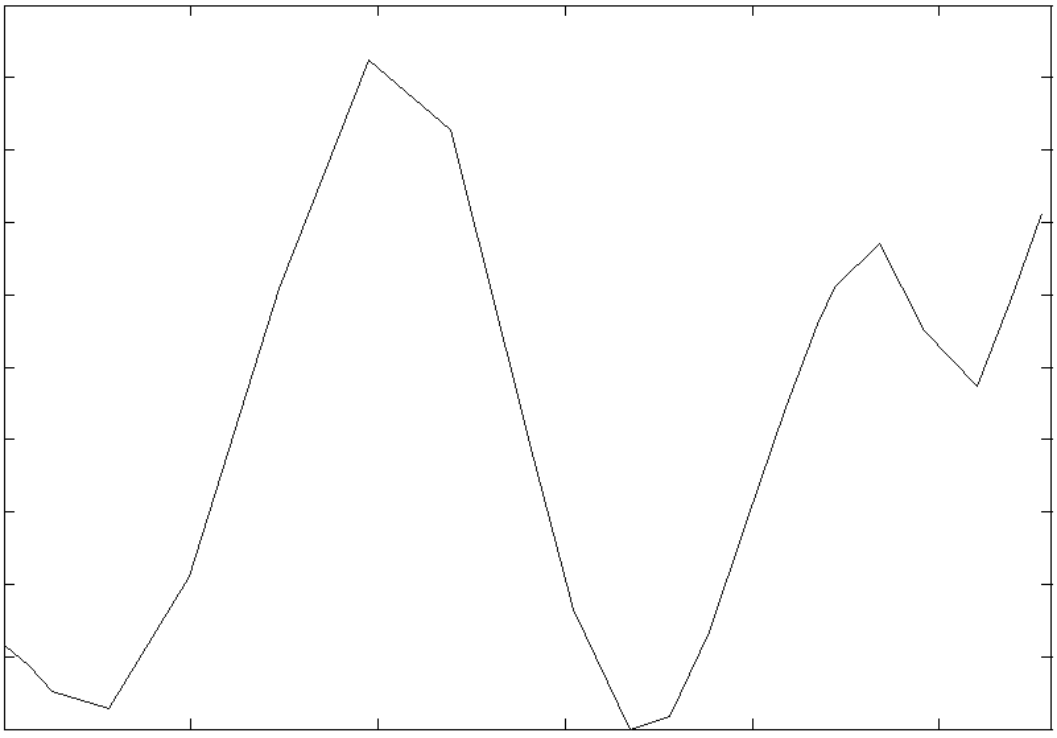

Fig 3.11 Power turbine undamped mode at N =54,341 RPM

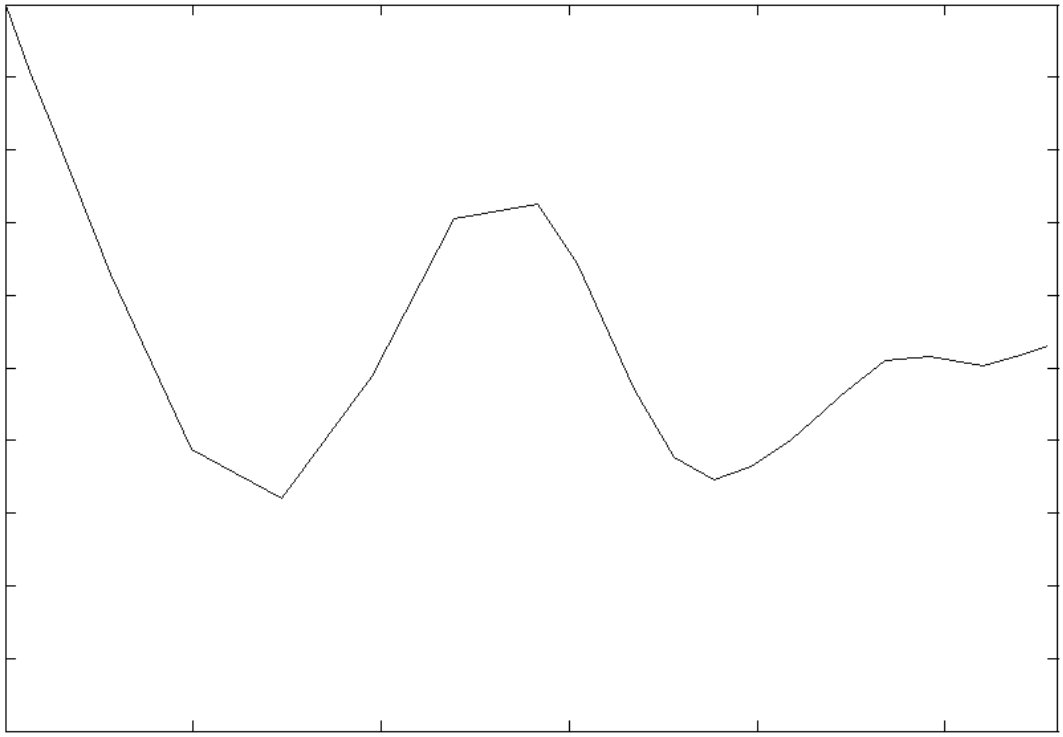

Fig 3.12 Power turbine undamped mode at N = 68,024 RPM

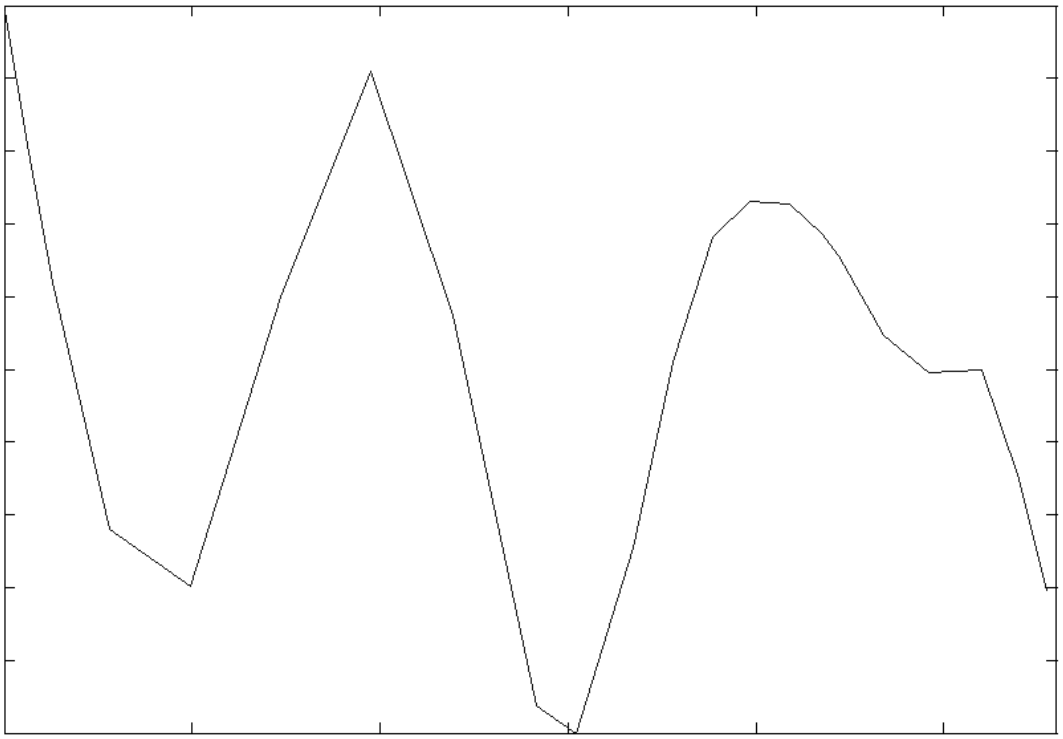

Fig 3.13 Power turbine undamped mode at N = 90,802 RPM

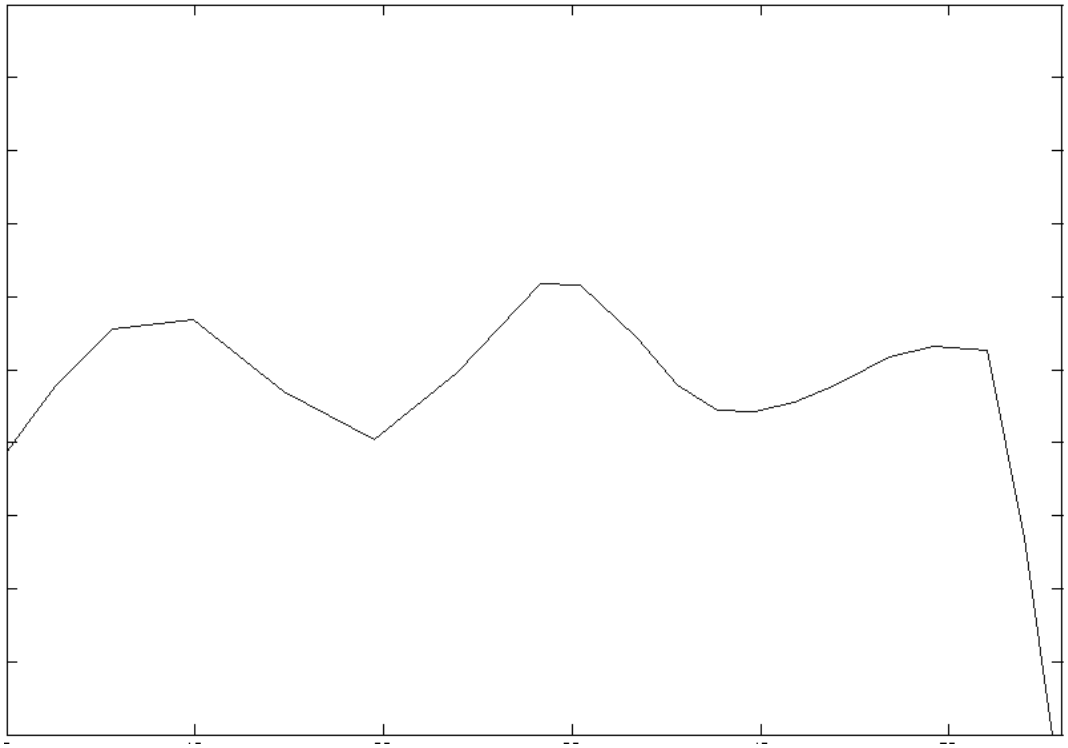

Fig 3.14 Power turbine undamped mode at N = 93,481 RPM

### 3.3 Gyroscopic Damped Mode Shapes

The gyroscopic damped mode shapes are generated considering the effect of the gyroscopic and damping matrices. This is done using the equation:

$$[\Lambda][\Phi] = [\Phi]\,[\lambda] \qquad 3.3$$

where

$$[\Lambda] = \begin{bmatrix} -M^{-1}C & -M^{-1}K \\ I & O \end{bmatrix}$$

[C] = System damping matrix including gyroscopic terms

[I] = Identity matrix

[O] = Zero Matrix

[λ] = Eigen values matrix (diagonal matrix)

Figures 3.15 to 3.17 show the 2D and 3D mode shapes as the displacement in the y direction against the shaft length.

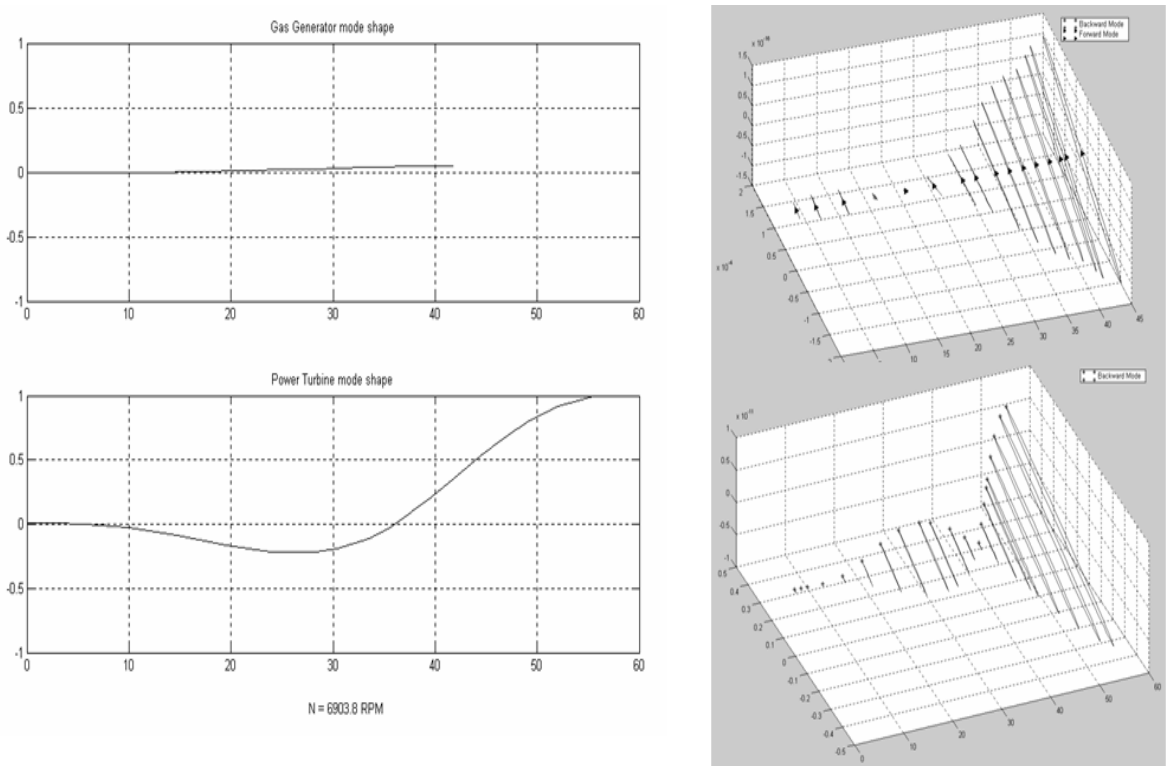


Fig 3.15 2D and 3D mode shapes (with whirl direction) at N = 6903.8 RPM

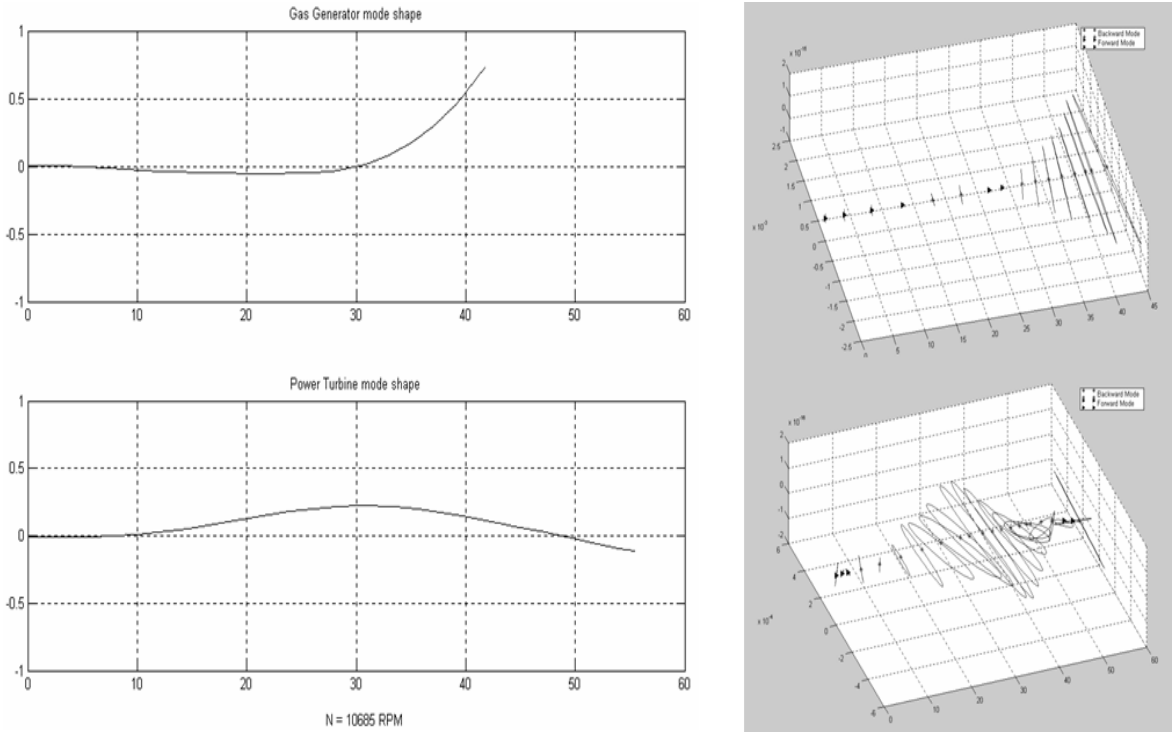


Fig 3.16 2D and 3D mode shapes (with whirl direction) at N = 10,397 RPM

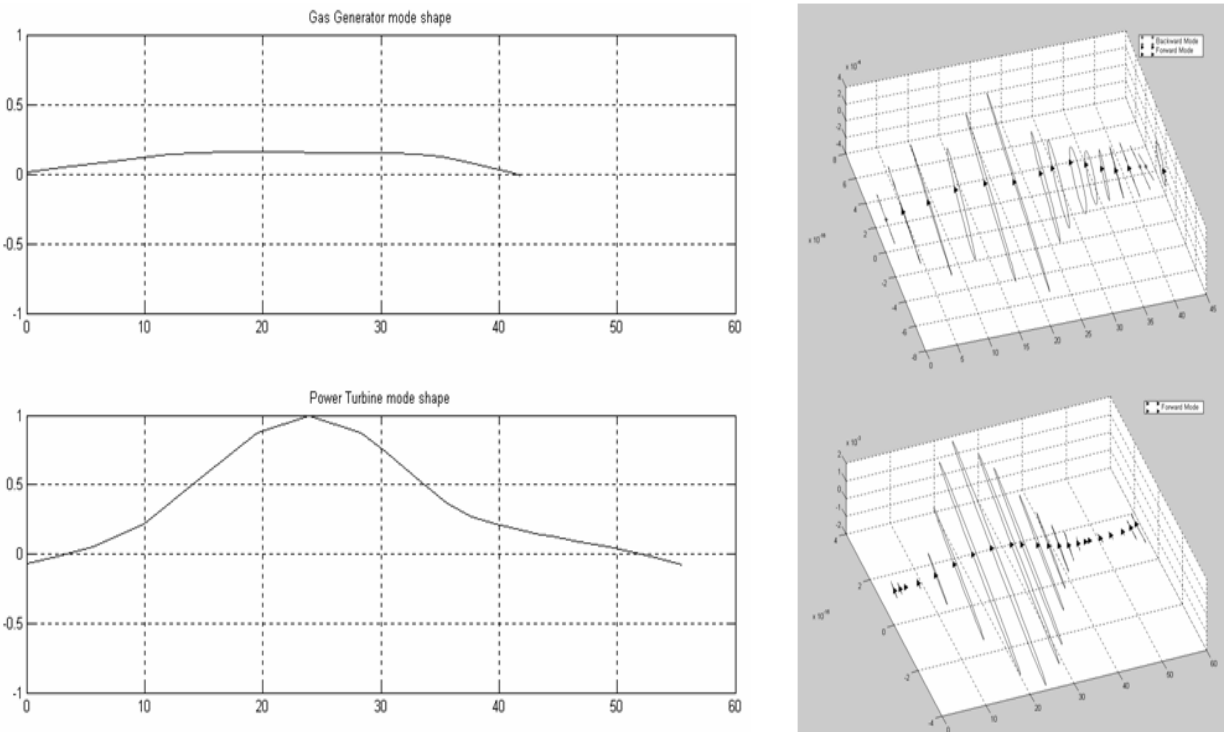


Fig 3.17 2D and 3D mode shapes (with whirl direction) at N = 20,504 RPM

## 3.4 Critical Speed Analysis

This is performed similar to the Mode Shape generation, where the reference spin speed is varying. It loops through the Power Turbine spin speeds from 0 to 30000 rpm in steps of 500 rpm, calculating the eigen values at each step. The critical speed analysis is useful to show the following system properties as a function of shaft speed:

- Sub/super-synchronous frequencies excitable at a particular operating speed.
- Confirms single analysis computation of critical speeds with $\lambda=i\omega$ ($\omega$ = Spin Speed)
- Increasing separation of forward and backward whirl modes with shaft speed.

Figure 3.18 show the natural frequencies vs speed plot for the given problem.

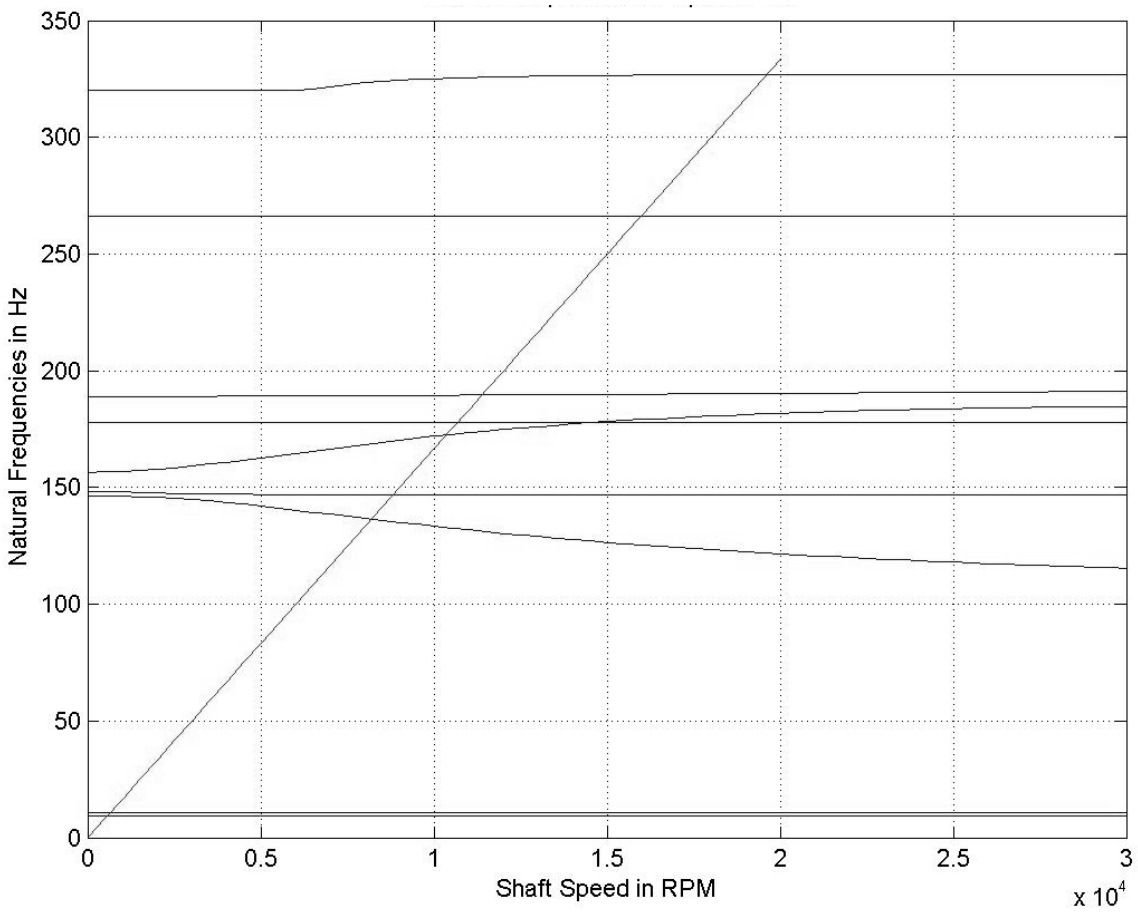


Fig. 3.18 Campbell diagram – natural frequencies vs speed plot

## 3.5 Steady State Harmonic Response Analysis

The general form of the equilibrium equation is written as:

$$(-\omega^2 [M] + i\,\omega [C] + [K]\,)\,\{Q(\omega)\} = \{F(\omega)\} \qquad 3.4$$

where

$[C] = [C_b] + [G(\omega)]$

$[C_b]$ = System Damping Matrix

$[G(\omega)]$ = Gyroscopic matrix

$Q(\omega)$ = Steady State Response vector

$F(\omega)$ = Input linear forcing function

An imbalanced load equivalent to 2850 N (640 lbs) force at 16000 RPM was applied to the power turbine mid-span and second stage turbine with a phase difference of Π rads. The result is shown in fig. 3.19.

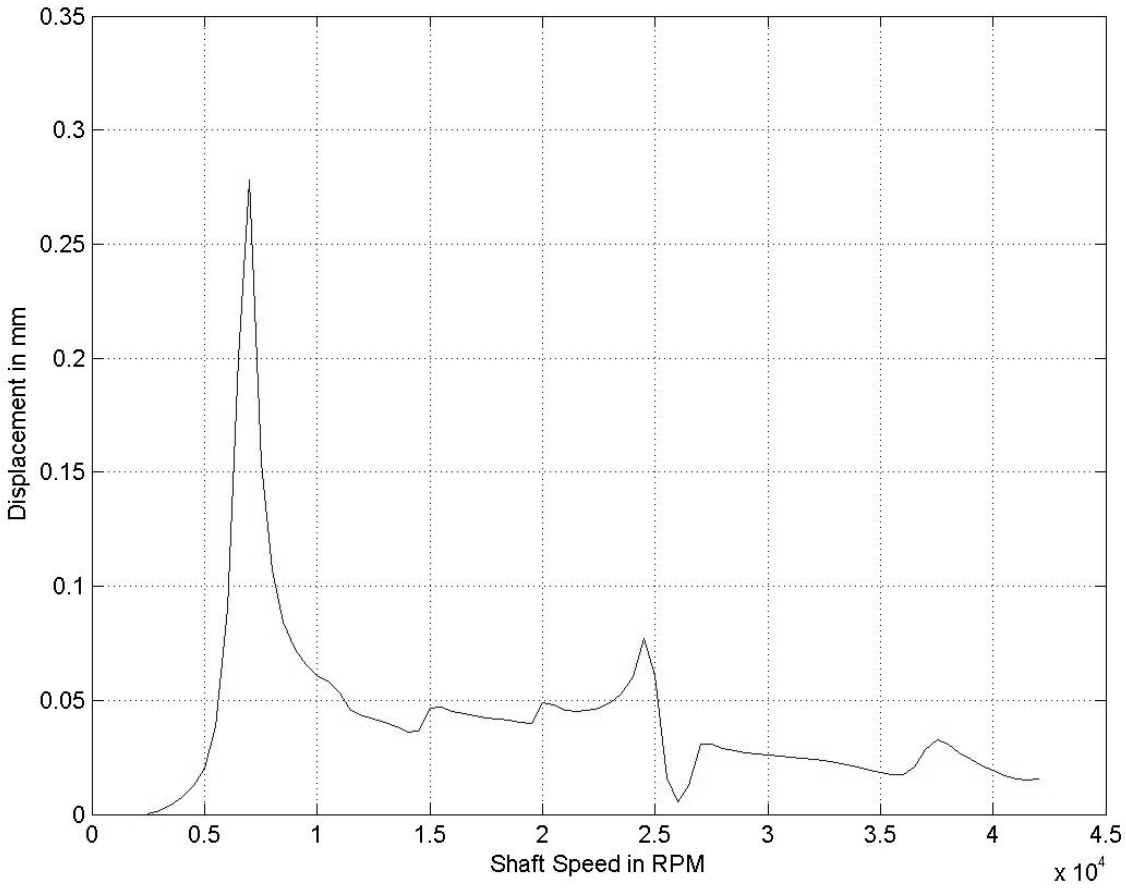


Fig 3.19 Steady state harmonic response of second stage power turbine

# CHAPTER IV
# BLADE-OUT RESPONSE ANALYSIS USING MODAL BASED SOLUTION ALGORITHMS

## 4.1 Modal Displacement Method

The equations of motion of a complete structural system are given by:

$$[M]\{\ddot{q}(t)\}+[C]\{\dot{q}(t)\}+[K]\{q(t)\}=\{F(t)\}+\{NF(q,\dot{q},t)\} \quad 4.1$$

where [M], [C] and [K] are the NxN mass, damping and stiffness matrices respectively; $\{q(t)\},\{\dot{q}(t)\},\{\ddot{q}(t)\}$ are the physical displacement, velocity and acceleration vectors respectively; {F(t)} is the applied linear force vector and $\{NF(q,\dot{q},t)\}$ is the applied non linear force vector.

The loading may be comprised of several spatial load vectors $\{F_o\}_i$ each with a corresponding time varying portion, $r_i(t)$. In this analysis, there is one spatial load vector for the sine part and one for the cosine part. The non-linear force vector is represented as a unit force at the selected DOF multiplied by the appropriate force component at each time step. Here we have 2 vectors (for the 2 radial directions) at each of the high fidelity bearings. Let

$$\{P(t)\}=\{F_o\}g(t)+\{NF(q,\dot{q},t)\}=\sum_{i=1}^{n}\{R_o\}_i r_i(t) \quad 4.2$$

where n is the total number of load vectors applied; $\{R_o\}_i$ is the invariant spatial portion and $r_i(t)$ is the time varying portion for each of the loads. For a modal displacement response analysis, the physical coordinates of eqn (4.1) are transformed to modal coordinates by a retained set of eigenvectors of the system.

$$\{q(t)\}=[\Phi]\{\chi(t)\} \quad 4.3$$

where $[\Phi]$ are determined from the general eigen value problem:

$$[K][\Phi]=[M][\Phi][\Omega^2] \quad 4.4$$

The number of retained eigenvectors, given by n, is typically much less than N. If eqn (4.2) is used to transform eqn (4.1) to modal coordinates:

$$[\hat{M}]\{\ddot{\chi}(t)\}+[\hat{C}]\{\dot{\chi}(t)\}+[\hat{K}]\{\chi(t)\}=\{\hat{F}(t)\} \tag{4.5}$$

where

$$\begin{aligned}
[\hat{M}] &= [\Phi]^T[M][\Phi] \\
[\hat{K}] &= [\Phi]^T[K][\Phi] \\
[\hat{C}] &= [\Phi]^T[C][\Phi] \\
\{\hat{F}(t)\} &= [\Phi]^T\{P(t)\}
\end{aligned} \tag{4.6}$$

## 4.2 Mode Acceleration Method

According to the Mode Acceleration (MA) method, the number of modes retained accurately spans the frequency range of interest; any loading represented by the non-retained modes will produce a quasi-static response. To develop the MA algorithm, eqn (4.1) is written as

$$[K]\{q(t)\}=\{P(t)\}-[M]\{\ddot{q}(t)\}-[C]\{\dot{q}(t)\} \tag{4.7}$$

Rewriting into modal coordinates, the approximate displacements using the MA algorithm are given by:

$$\{q_u(t)\}=[K]^{-1}\{P(t)\}-[K]^{-1}[M][\Phi]\{\ddot{\chi}(t)\}-[K]^{-1}[C][\Phi]\{\dot{\chi}(t)\} \tag{4.8}$$

The MA physical velocities and accelerations are determined using:

$$\begin{aligned}
\{\dot{q}_u(t)\} &= [\Phi]\{\dot{\chi}(t)\} \\
\{\ddot{q}_u(t)\} &= [\Phi]\{\ddot{\chi}(t)\}
\end{aligned} \tag{4.9}$$

## 4.3 Modal Truncation Augmentation Method

The pseudo static response is

$$[K]\{q\}=\{R_o\}_i \tag{4.10}$$

Now

$$[\Phi]^T[K][\Phi]\{\chi\} = [\Phi]^T\{R_o\}_i$$
$$\omega^2\{\chi\} = [\Phi]^T\{R_o\}_i \qquad 4.11$$
$$\{\chi\} = [\omega^2]^{-1}[\Phi]^T\{R_o\}_i$$

The pseudo static force represented by the modes can be written as:

$$\{R_s\}_i = [K][\Phi]\{\chi\} = [M][\Phi][\omega^2][\omega^2]^{-1}[\Phi]^T\{R_o\}_i \qquad 4.12$$

$$\{R_s\}_i = [M][\Phi][\Phi]^T\{R_o\}_i \qquad 4.13$$

The spatial load $\{R_o\}_i$ does not completely represent the retained modes in a modal reduction technique. Let the portion of the load vector $\{R_o\}_i$ that is not represented by the modes be the force truncation vector, $\{R_t\}_i$ which can be evaluated by subtracting the modally represented load vector $\{R_s\}_i$ from the applied spatial load vector $\{R_o\}_i$.

The force truncation (FT) vector is given by:

$$\{R_t\}_i = \{R_o\}_i - \{R_s\}_i \qquad 4.14$$

The modal truncation augmentation (MTA) method attempts to correct for the inadequate representation of the spatial loads in the modal domain by creating additional "pseudo eigen" or MT vectors to include in the modal set for the response analysis. This modal truncation (MT) vector is derived from the statically truncated displacement vector {X} obtained from the force truncation by solving

$$[K]\{X\}=\{R_t\}_i \qquad 4.15$$

Now form

$$\overline{[K]} = \{X\}^T[K]\{X\}$$
$$\overline{[M]} = \{X\}^T[M]\{X\} \qquad 4.16$$

and solve the reduced eigenvalue problem as:

$$\overline{[K]}[Q] = \overline{[M]}[Q][\varpi^2] \qquad 4.17$$

Form the MT vectors $\{\overline{P}\}$ which have the associated frequencies $[\varpi]$

$$\{\overline{P}\} = \{X\}[Q] \qquad 4.18$$

The MT vector is appended to the modal set $[\Phi]$ for the modal response analysis. The 'augmented eigenvector' set that is used for the modal analysis is:

$$[\tilde{\Phi}] = [\Phi \quad \bar{P}] \tag{4.19}$$

For several applied spatial load vectors, the vector {X} above is replaced by a matrix whose columns are equal to the number of independent spatial loads applied. This gives several MT vectors which are appended to the reduced eigen vector set.

The physical coordinates are now transformed into the modal coordinates as:

$$\begin{aligned} \{q(t)\} &= [\tilde{\Phi}]\{\chi(t)\} \\ \{\dot{q}(t)\} &= [\tilde{\Phi}]\{\dot{\chi}(t)\} \\ \{\ddot{q}(t)\} &= [\tilde{\Phi}]\{\ddot{\chi}(t)\} \end{aligned} \tag{4.20}$$

Using Eq. (4.20) to transform Eq. (4.1) yields

$$[\tilde{M}]\{\ddot{\chi}(t)\} + [\tilde{C}]\{\dot{\chi}(t)\} + [\tilde{K}]\{\chi(t)\} = \{\tilde{F}(t)\} \tag{4.21}$$

where

$$\begin{aligned} [\tilde{M}] &= [\tilde{\Phi}]^T [M][\tilde{\Phi}] \\ [\tilde{C}] &= [\tilde{\Phi}]^T [C][\tilde{\Phi}] \\ [\tilde{K}] &= [\tilde{\Phi}]^T [K][\tilde{\Phi}] \\ \{\tilde{F}(t)\} &= [\tilde{\Phi}]^T \{P(t)\} \end{aligned} \tag{4.22}$$

The physical acceleration, velocity and displacements are found using the pseudo modal set of vectors after completing the modal response analysis.

## 4.4 Theoretical Comparison of the Methods

To compare the MA and MT methods, the exact solution of eqn. 4.1 is written in two parts as:

$$\{q(t)\} = \{q_s(t)\} + (q_t(t)\} \tag{4.23}$$

The first part, $\{q_s(t)\}$ is the portion of the displacement solution obtained from the retained modes and the second part, $\{q_t(t)\}$ is the portion of the displacement solution lost due to the modal truncation. Substituting eqns. 4.14 and 4.23 into equation 4.1,

$$[M]\{\ddot{q}_s(t)\}+[C]\{\dot{q}_s(t)\}+[K]\{q_s(t)\}$$

$$+[M]\{\ddot{q}_t(t)\}+[C]\{\dot{q}_t(t)\}+[K]\{q_t(t)\}=\sum_{i=1}^{n}(R_s+R_t)_i\,r_i(t) \qquad 4.24$$

The modal response solved from equation (4.5) yields a solution in the physical domain that satisfies the equation:

$$[M]\{\ddot{q}_s(t)\}+[C]\{\dot{q}_s(t)\}+[K]\{q_s(t)\}=\sum_{i=1}^{n}(R_s)_i\,r_i(t) \qquad 4.25$$

Subtracting equation (4.25) from (4.24) we get

$$[M]\{\ddot{q}_t(t)\}+[C]\{\dot{q}_t(t)\}+[K]\{q_t(t)\}=\sum_{i=1}^{n}(R_t)_i\,r_i(t) \qquad 4.26$$

Equation 4.26 is the portion of the solution not represented by the modes retained in the analysis. Both the MA and the MT methods attempt to find a solution for eqn. 4.26 without calculating the non retained modes by approximating the non-modally represented solution. The difference between the two methods is in the approximation for $\{q_t(t)\}$. The MA method approximates $\{q_t(t)\}$ by standard modal truncation plus a correction for the static response of the portion of $P(t)$ that is omitted by the mode expansion. The MT method approximates it by a dynamic solution which averages all the non retained modes by a truncation augmentation vector. Thus, the MA method is an approximation to the MTA vector method. Also, the MA method corrects only the physical displacement whereas the physical velocity and acceleration are simply represented using only the retained modes. The MTA method attempts to correct the physical displacements, velocity and acceleration. Due to the added dynamics and the velocity and acceleration corrections, it is expected that the MTA method would give better results overall than the MA method.

## 4.5 Simulation Results

Blade loss simulations are conducted to illustrate implementation of the high fidelity ball bearing FE SFD model and efficiency of the MTA method [14]. Numerical integration (Refer Appendix A) of the equations of motion for aircraft turbine engine mounted on the support system is performed using the Newmark Beta method [15]. The

bearing dimension, material characteristics and SFD damper dimension for the locations #0 and #4 are listed in Table 4.1. A simple support model with linear stiffness and damper is utilized for all the locations except #0 and #4 since they are the most crucial in the event of a blade loss. The stiffness and damping coefficients are listed in Table 4.2.

Table 4.1 Specifications of Support Bearings

| **Dimension** | **Brg #0 (210J)** | **Brg #4 (217H)** |
|---|---|---|
| **Geometry:** | | |
| Bore diameter, BD [cm] | 5.08 | 8.38 |
| Outside diameter, OD [cm] | 9 | 11 |
| Width [cm] | 2 | 1.6 |
| Number of balls | 21 | 27 |
| Diameter of a ball [mm] | 8.73 | 9.53 |
| Initial contact angle [deg] | 15 | 15 |
| Axial preload [N] | 800 | 1,100 |
| Number of rows | 1 | 1 |
| **Material:** | | |
| Density of ball: steel [g/cm$^3$] | 7.8 | 7.8 |
| Density of races: steel [g/cm$^3$] | 7.8 | 7.8 |
| Elastic modulus of ball [GPa] | 208 | 208 |
| Poisson's ratio of ball | 0.3 | 0.3 |
| Elastic modulus of races [GPa] | 208 | 208 |
| Poisson's ratio of races | 0.3 | 0.3 |
| **Support system:** | | |
| Stiffness of centering spring [N/mm] | 5254 | 5254 |
| Radius of SFD journal [cm] | 10 [cm] | 8 |
| Length of SFD journal [cm] | 4 | 3.2 |
| Viscosity of fluid lubricant [cP] | 70 | 70 |
| Radial clearance [mm] | 0.635 | 0.635 |

Table 4.2 Stiffness and Damping of Support System

| Bearing No. | Stiffness (N/m) | Damping (N-sec/m) |
|---|---|---|
| ND | 1.751E08 | 1.751E03 |
| #1 | 1.751E08 | 1.751E03 |
| #2 | 8.756E07 | 1.751E03 |
| #3 | 7.005E07 | 1.751E03 |
| FDB | 8.756E07 | 3.502E03 |
| ADB | 8.756E07 | 3.502E03 |

The pseudo modal set for the given set of loads (linear & non linear) is determined as follows. There is one spatial load vector for the sine part and one for the cosine part of the applied imbalanced load. The non linear force vector is represented as a unit force at selected DOF multiplied by the appropriate force component at each time step. Here we have 2 vectors (for the 2 radial directions) at each of the high fidelity bearings.

The power turbine is spinning at 16,000 rpm. Before the blade loss occurs, several revolutions of time transient solutions under low imbalanced load are performed to show proper status of the motion of the rotor-support system. Sudden increase of imbalanced load is then applied at the second stage (node #20) of the power turbine and at the geometric center of the power turbine (node #11). Numerical solution is obtained using Newmark Beta method [15]. The total integration time is 35 rev. for each case and the time step $2 \cdot 10^{-7}$ sec is used.

Figure 4.1(a) shows the transient responses of the second stage power turbine rotor under an unbalanced force of 2,847 N. After several overshoots, steady-state peak-to-peak amplitude of 0.9 mm is observed. The orbit plot in Fig. 4.1(b) shows the initial several overshoots and steady-state whirls of an elliptical shape. The transient response of the SFD journal at bearing #0 and steady-state peak-to-peak amplitude of 0.12 mm are shown in Fig. 4.2(a), while the transient response of the SFD journal at bearing #4 is shown in Fig. 4.3. It can be noticed that the steady-state amplitude in *x*-axis at bearing #4

is about 4 times greater than that at bearing #0 and the amplitude in *y*-axis at bearing #4 is damped out.

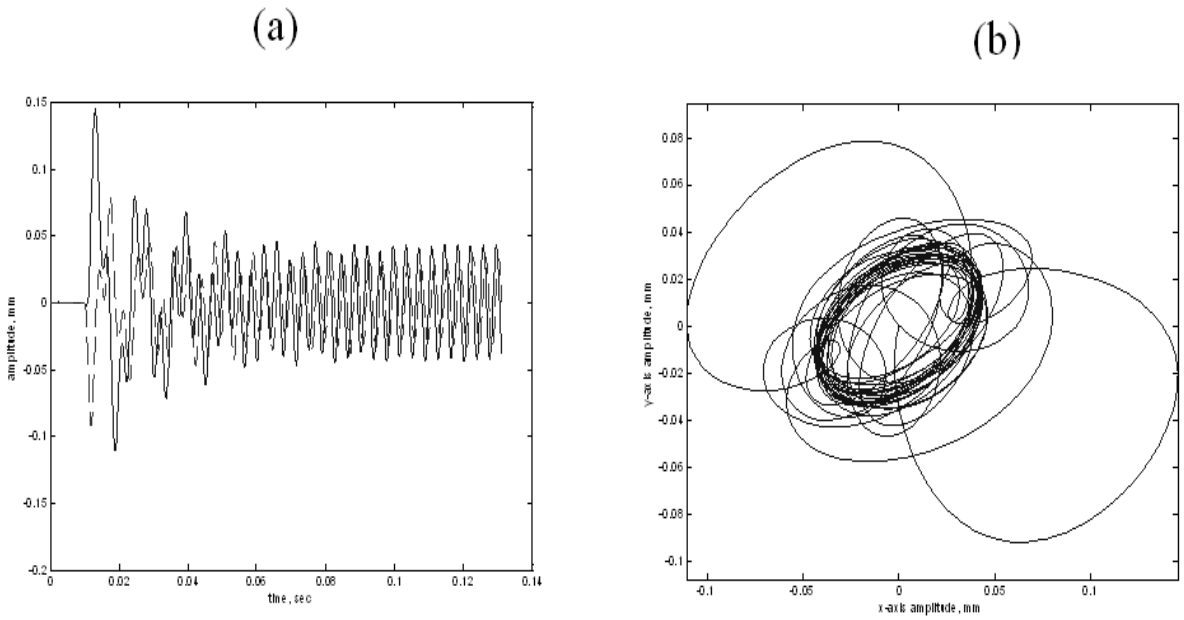


Fig. 4.1 (a) Transient response and (b) orbit plot of the second stage of the power turbine for 35 rev.:—, *y*-axis; - -, *z*-axis

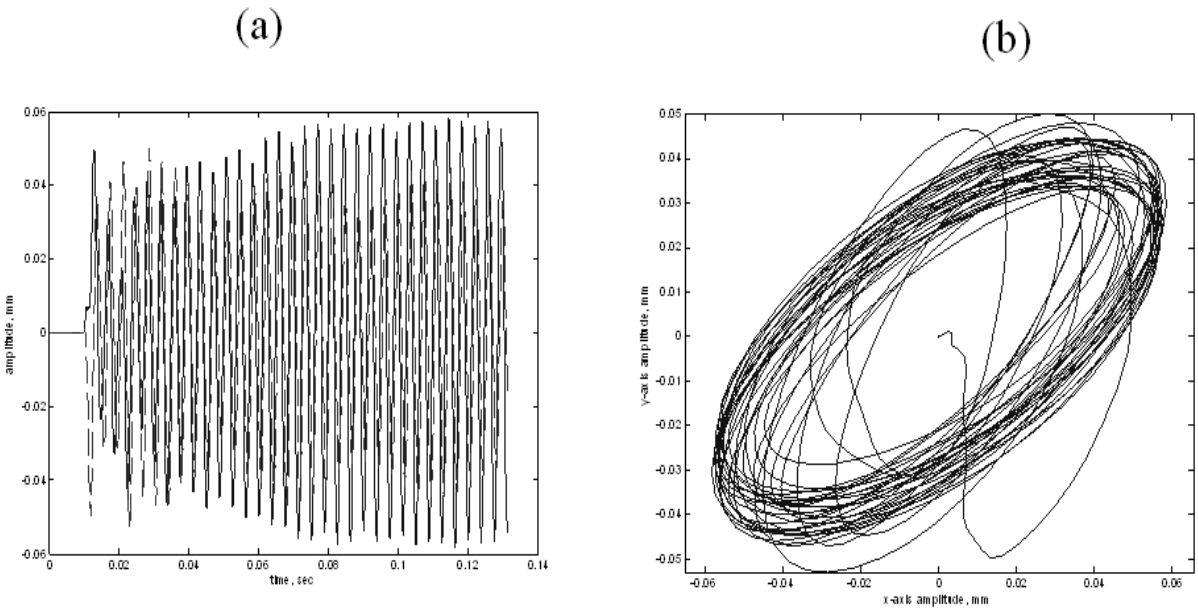


Fig. 4.2 (a) Transient response and (b) orbit plot of the SFD journal at brg #0 for 35 rev.:—, *y*-axis; - -, *z*-axis

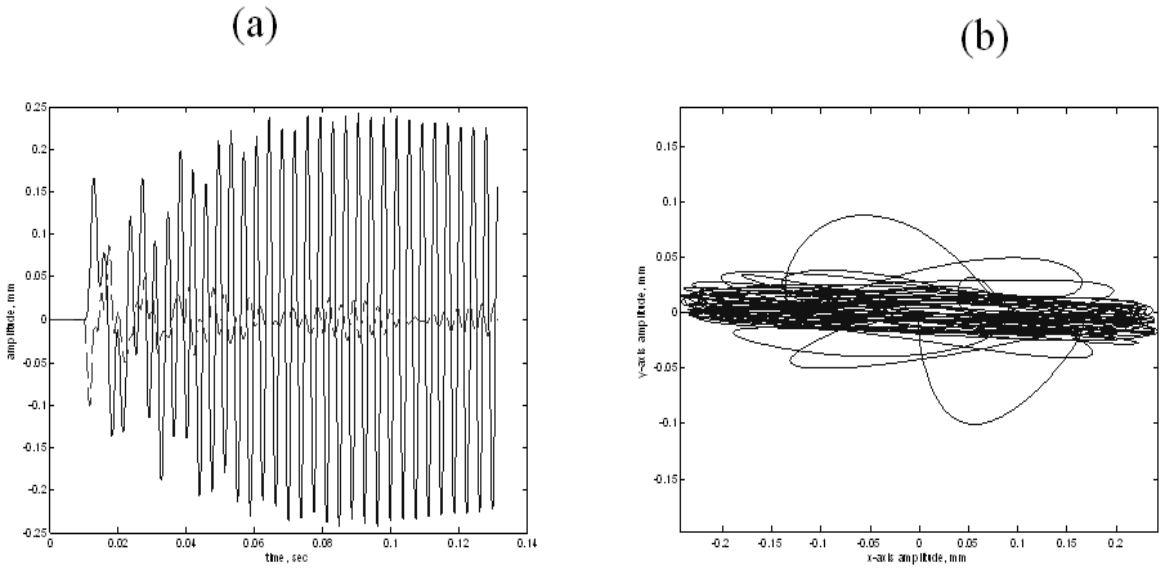


Fig. 4.3 (a) Transient response and (b) orbit plot of the SFD journal at brg #4 for 35 rev.:—, *y*-axis; - -, *z*-axis

Transmissibility is defined as the ratio of the force transmitted to the support system to the unbalanced force and is described as:

$$T = \frac{\left|F_X + F_s\right|}{\left|F_u\right|} \tag{4.27}$$

where $F_X$ is the damping force from the SFD, $F_s$ is the centering spring force and $F_u$ is the unbalanced force. The transmissibility at bearing #0 shown in Fig.4.4 does not have much difference between the initial and final values, while that at bearing #4 has an initial value of 0.3 and oscillates about 0.05 after 35 rev. Figure 4.5 shows the maximum contact loads between the races and balls at each time step. The initial load due to preload is applied before the blade loss occurs which causes the initial offset. It is observed that the contact loads at bearing #0 are higher than those at bearing #4 even though imbalanced load location at the power turbine blade is closer to bearing #4. This is due to the fact that the number of balls of bearing #0 (21) are lesser than those of bearing #4 (27) and hence the contact load applied on each ball in bearing #0 is greater. The maximum stress due to compressive contact load is shown in Fig.4.6. It has the same

trend as the contact load because the contact stress is a function of the contact load. Contact stress $\sigma_{i,e}$ is determined from

$$\sigma_{i,e} = -\frac{3Q_{i,e}}{2\pi \cdot a_{i,e} b_{i,e}} \tag{4.28}$$

where $a$, $b$ are the semi-major & semi-minor axes of an elliptical contact area and $Q_{i,e}$ is internal bearing load due to thermal expansions.

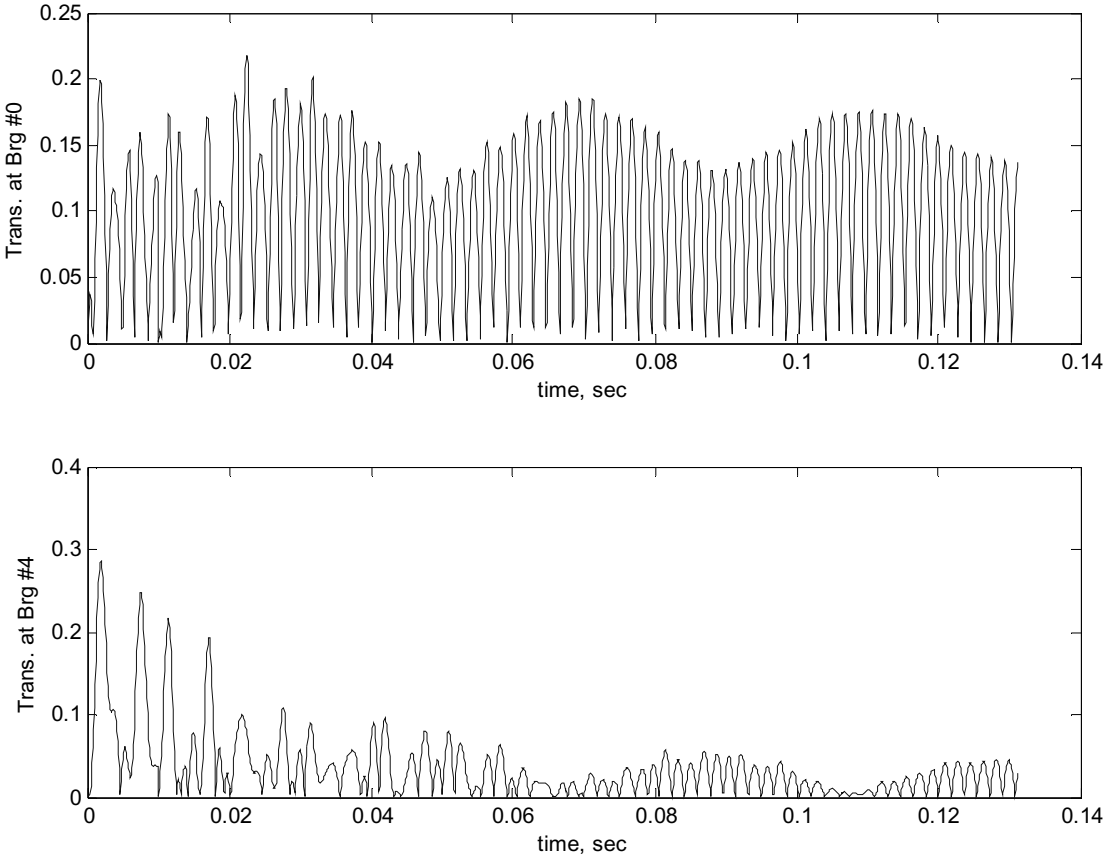


Fig. 4.4 Transmissibility (a) at brg #0 and (b) at brg #4

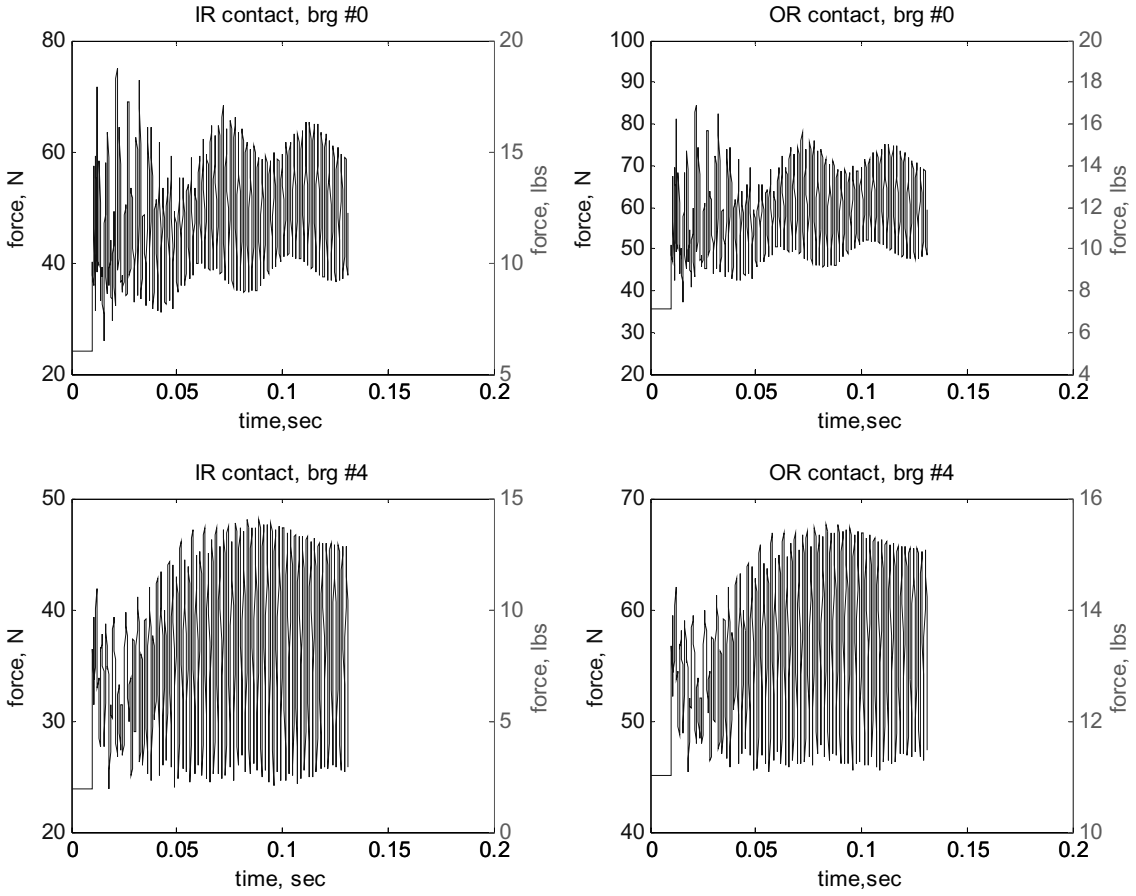


Fig. 4.5 Maximum contact loads (a) at brg #0 IR, (b) at brg #0 OR, (c) at brg #4 IR, and (d) at brg #4 OR

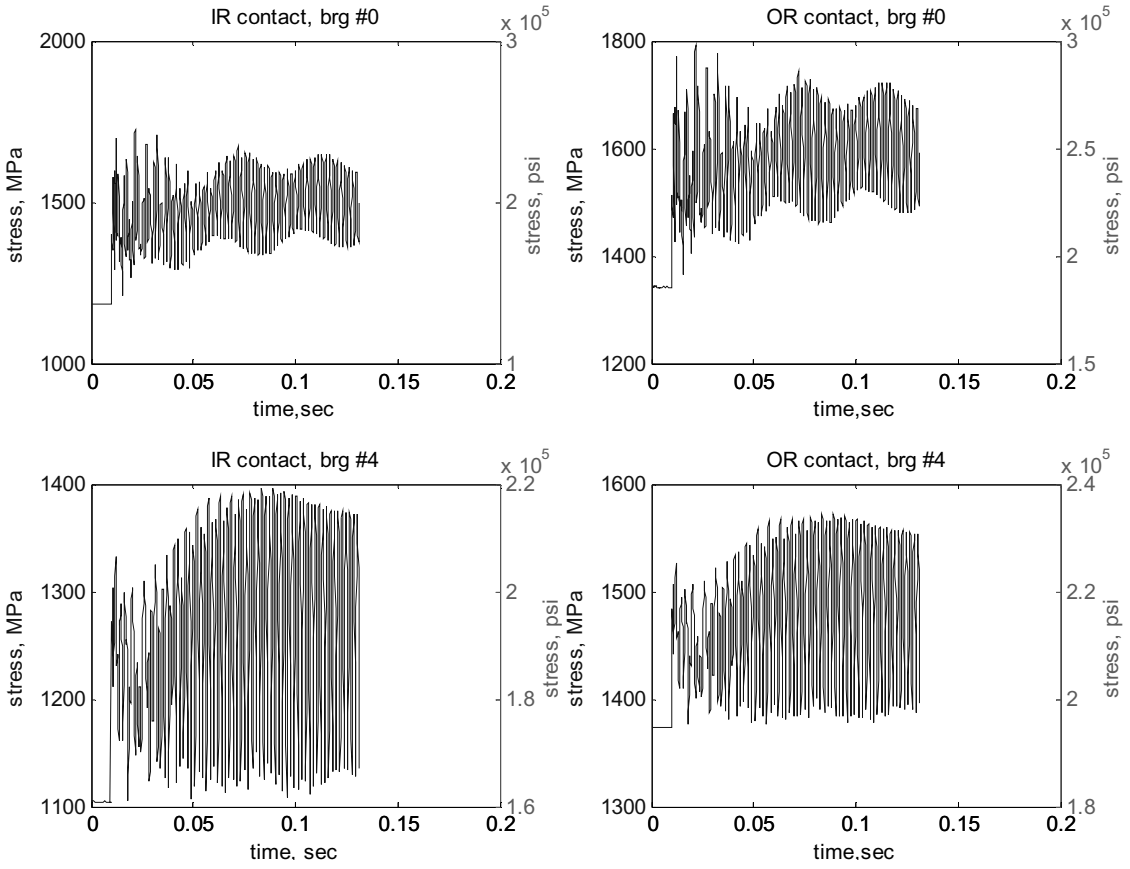


Fig. 4.6 Maximum contact stress (a) at brg #0 IR, (b) at brg #0 OR, (c) at brg #4 IR, and (d) at brg #4 OR

Figures 4.7, 4.8 show the maximum and minimum pressure in the FE SFD. A supply pressure of 0.21 MPa is used. Due to the high eccentricity, the maximum pressure at bearing #4 is much higher than that at bearing #0, while the minimum pressure at bearing #4 is lower than that at bearing #0. Zero pressure indicates oil cavitation.

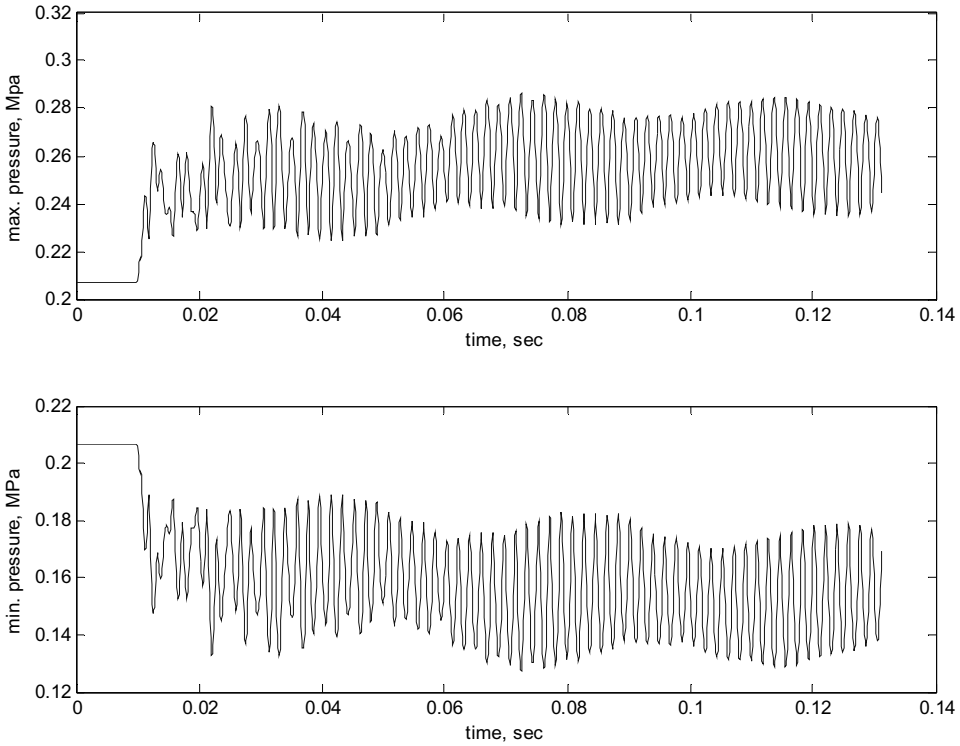


Fig. 4.7 Maximum and minimum pressures in brg #0 SFD

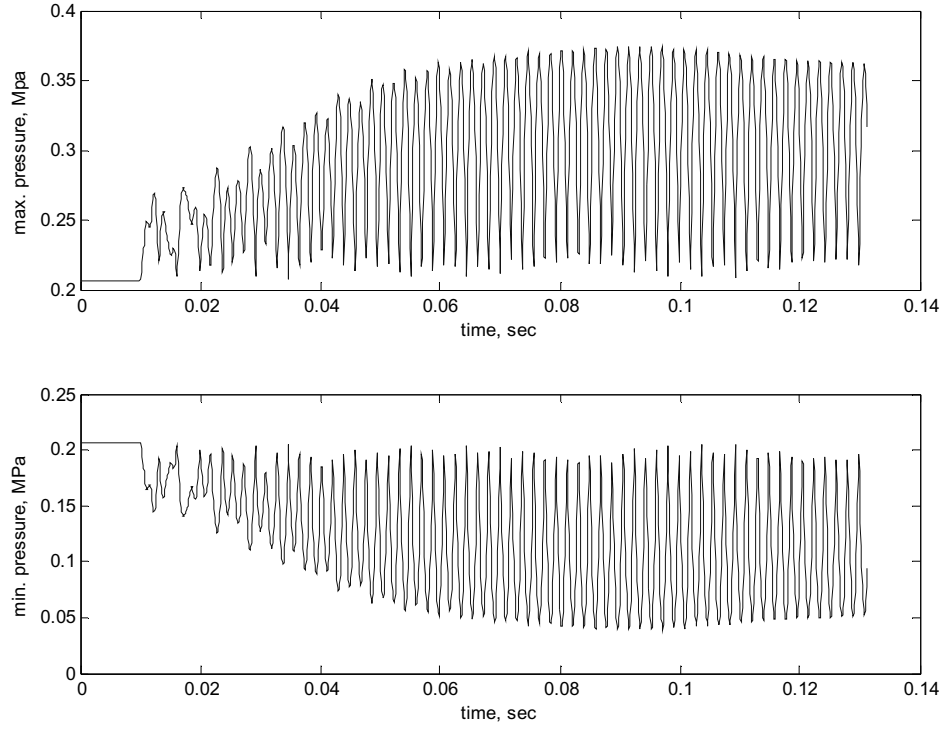


Fig. 4.8 Maximum and minimum pressures in brg #4 SFD

Table 4.3 shows a comparison of the computational time taken for the different methods under identical loading conditions on an Intel P3 933 MHz processor with 512 MB RAM and 20 GB hard disk.

Table 4.3 Computational Time Comparison

| **Method** | **No. of Rotor modes used** | **Maximum Error (%)** | **Time taken (in hrs)** | **Time Savings (%)** |
|---|---|---|---|---|
| Numerical Integration of Physical Co-ordinates | - | 0 % | 23.5 hrs | 0 % |
| All Modes | All (228) | 0.0001 % | 22.9 hrs | 2.5 % |
| Mode Displacement | 22 | 15.3 % | 14.9 hrs | 36.6 % |
| Mode Acceleration | 22 | 14.2 % | 16.4 hrs | 30.2 % |
| Modal Truncation Augmentation | 22 | 8.9 % | 14.3 hrs | 38.8 % |

## 4.6 Parametric Study:

A study of the important parameters is performed with the amount of unbalanced force varying from 712 N to 11,387 N. The whirl amplitude change of the power turbine versus the unbalanced force is shown in Fig. 4.9. The very first overshoot after blade loss occurs is called transient amplitude here.

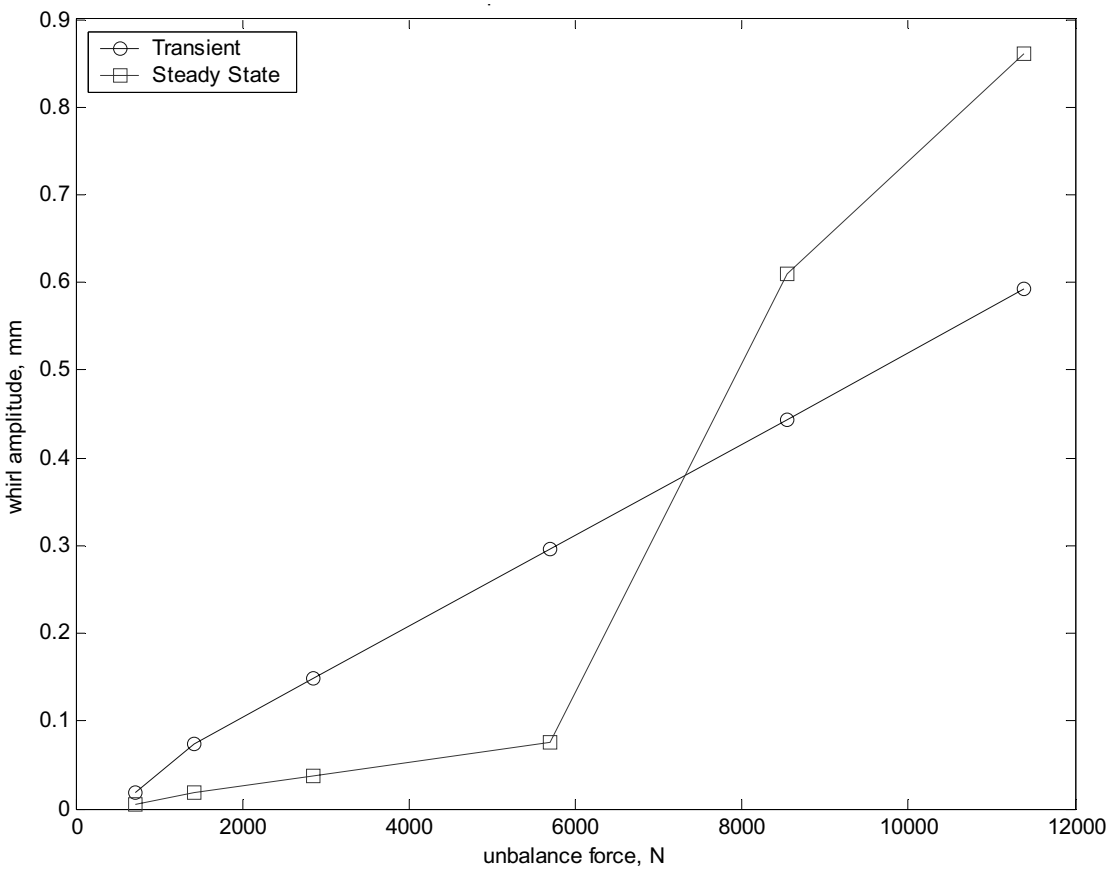


Fig.4.9 Whirl amplitude of the power turbine

The transient motion is greater than the steady-state motion up to 5694 N, which means that the SFD damps out the transient vibration but after 5694 N, the steady-state whirl motion is greater than the transient motion. The maximum whirl motion of the SFD journal at bearing #0 versus the unbalanced force in Fig. 4.10 shows the linear relationship between the amplitude and the force. A contact stiffness of 1.75E+5 N/mm between the SFD journal and outer bearing is used. In the last two cases in Fig. 4.10, the SFD journal at bearing #4 bottoms out and rubs against the outer race. This results in no damping in the system which results in the non linear relationship.

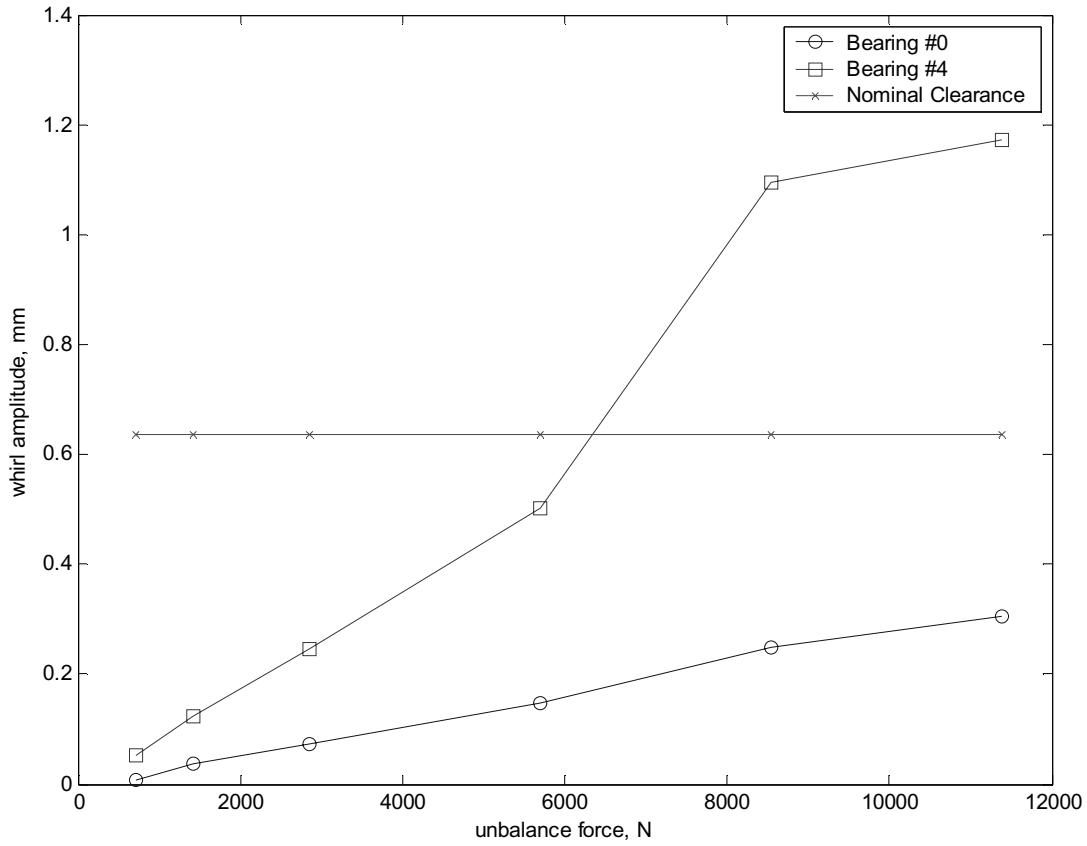


Fig.4.10 Maximum whirl amplitude of the SFD journal

Figure 4.11 shows the maximum contact loads at bearing #0 and at bearing #4 respectively. As observed in Fig. 4.11, the contact load at the outer race is slightly higher than that at the inner race because of centrifugal force on balls. However, the contact loads at both races are almost same in the last two high imbalanced cases. The contact loads at bearing #4 increases enormously in the two cases. Figure 4.12 illustrates that the contact stress at bearing #0 increases linearly and the contact stress at bearing #4 is lower than that at bearing #0 up to 5694 N due to the higher number of balls but it increases enormously in the last two cases. The maximum and minimum SFD pressures at both bearings are compared in Fig. 4.13. The maximum pressure at bearing #4 increases to 1.2 MPa and that at bearing #0 increases to 0.6 MPa. The excessive nonlinear film force produced by high eccentricity can make the SFD lock up and cause an increase in the transmissibility as shown in Fig. 4.14.

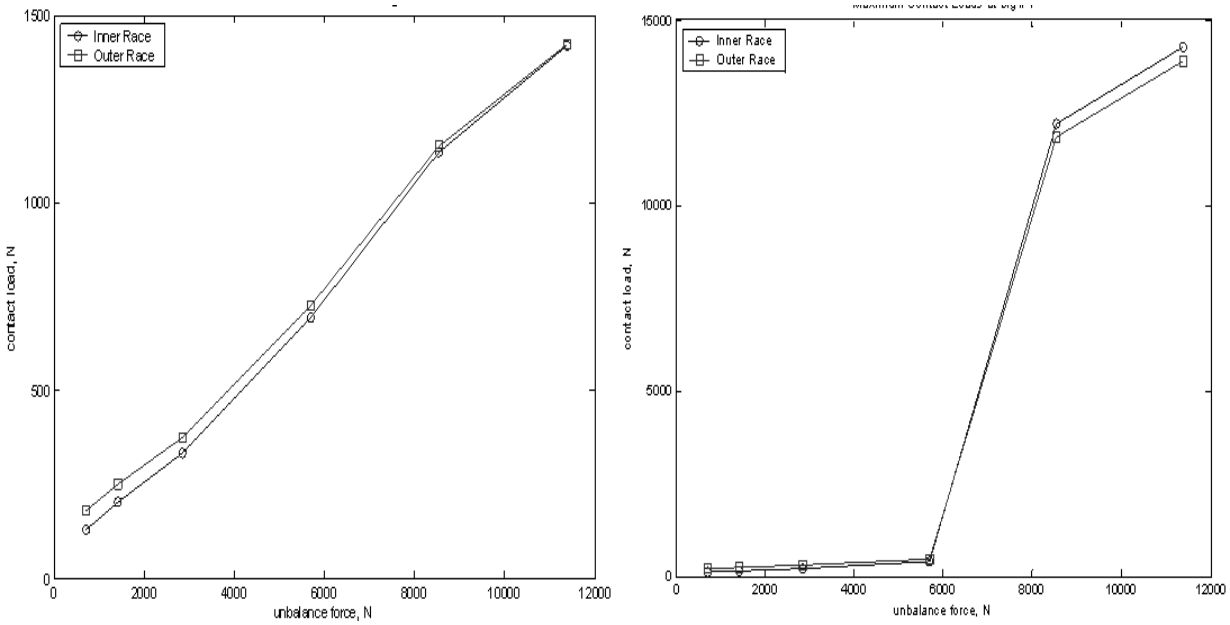


Fig. 4.11 Maximum ball contact loads at (a) brg #0 and (b) brg #4

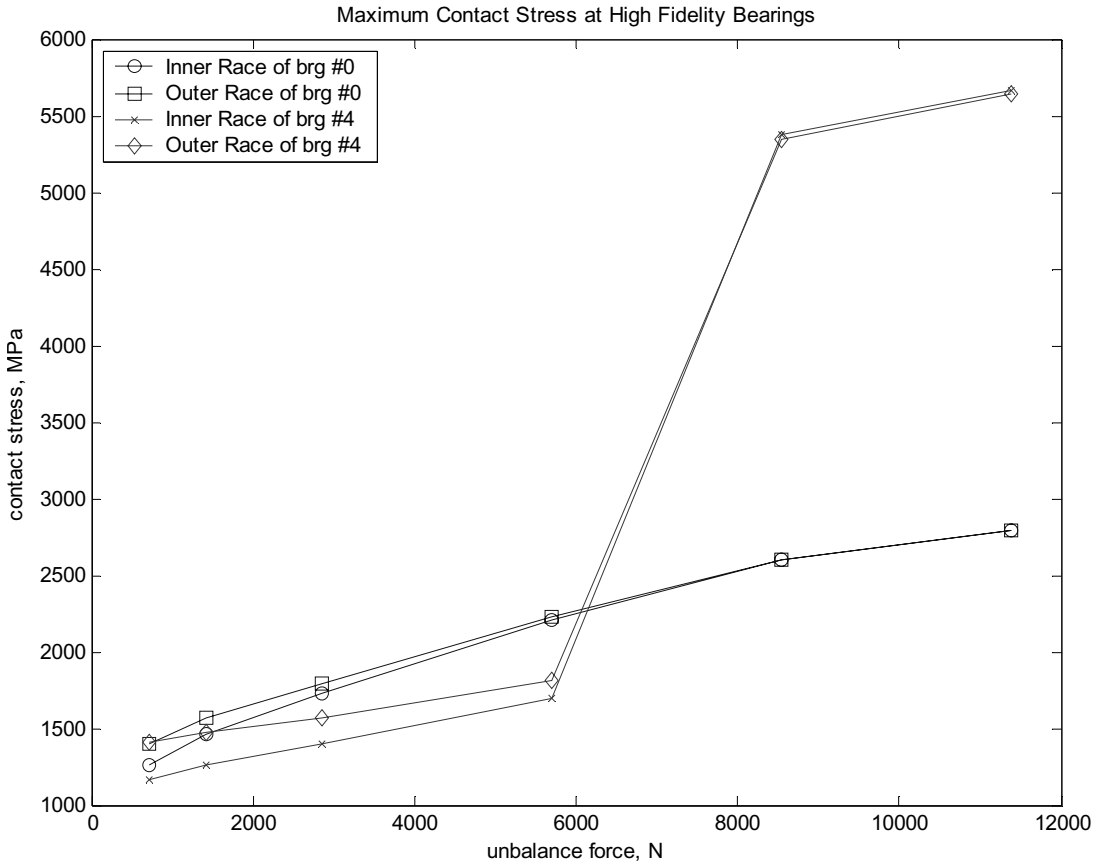


Fig. 4.12 Maximum contact stress vs unbalanced load

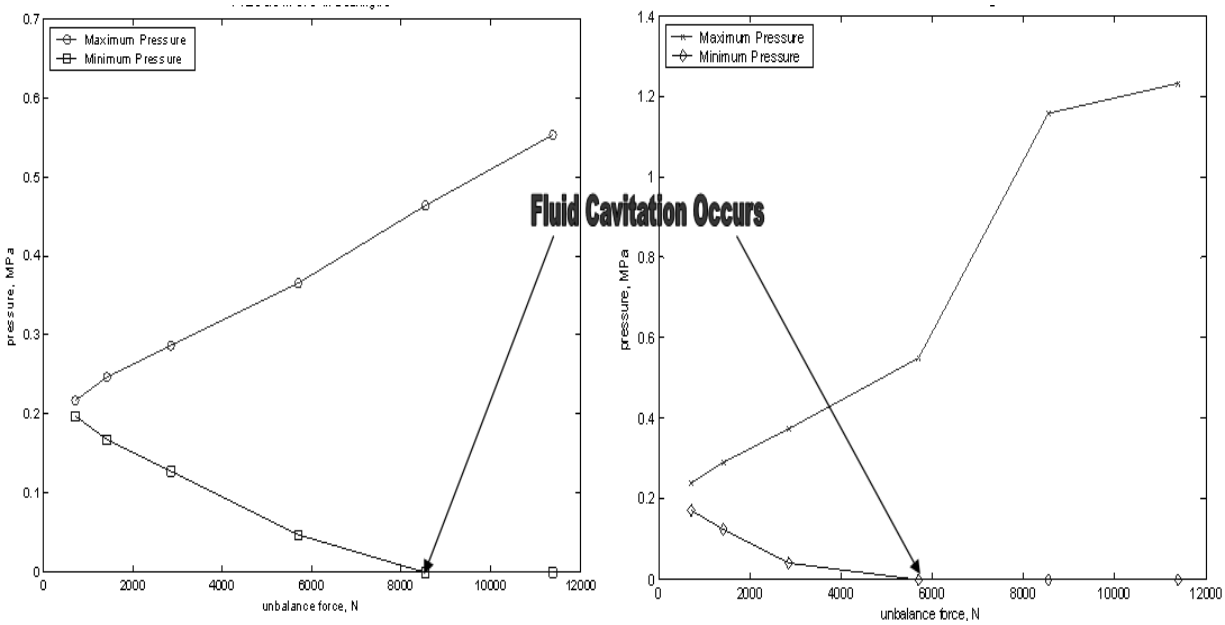


Fig. 4.13 Pressure in SFD in (a) brg #0 and (b) brg #4

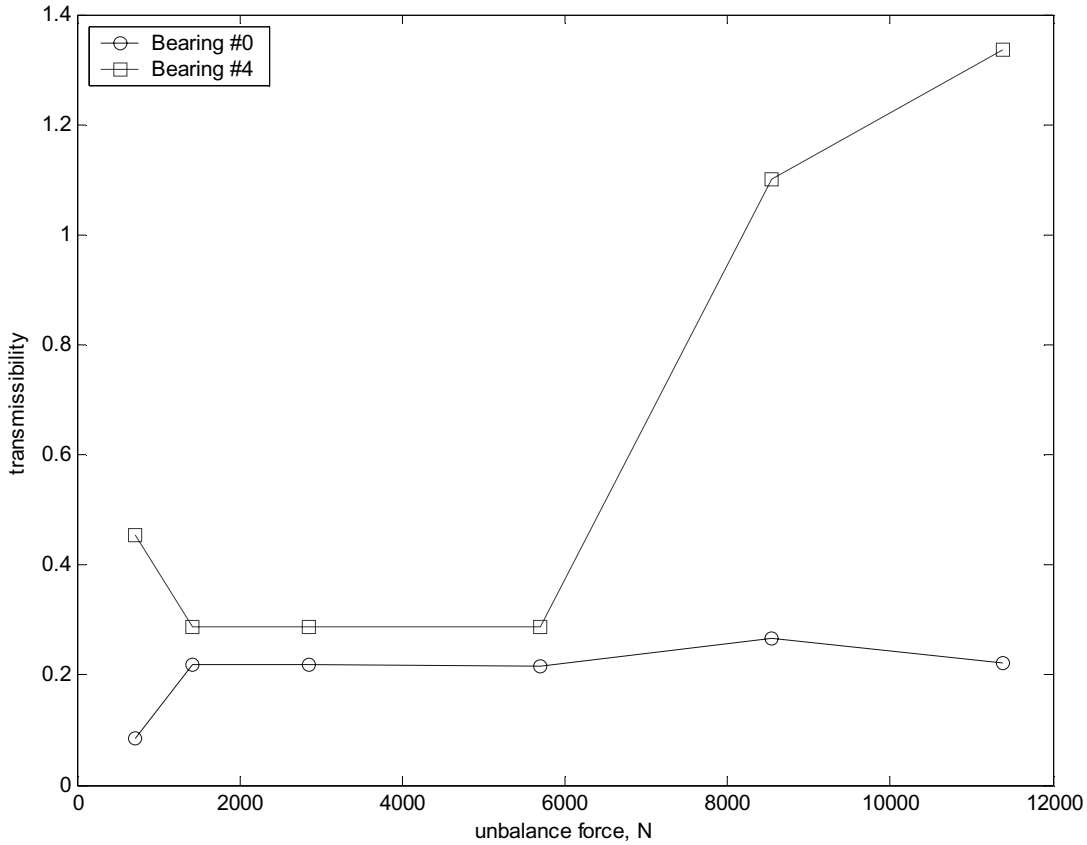


Fig. 4.14 Transmissibility plots

The simulation results show that the SFD damps out the transient whirl amplitude of the power turbine rotor up to an unbalanced force of 5694 N followed by an enormous increase in the steady state whirl amplitudes because the SFD with high eccentricity locks up the rotor support system. This phenomenon is also observed in the maximum contact loads, which increase over 25 times higher than the contact loads at 5694 N, and in the transmissibility, which increases from 0.26 to 1.1. The maximum contact stress also increases proportionally with the 1/3 power of the contact load as the unbalanced force increases. The oil film cavitation at bearing #4 close to the imbalanced load location occurs at an unbalanced force of 5694 N, while the cavitation at bearing #0 occurs at 8541 N. It is also observed in the transmissibility plot in Fig. 4.14 that the transmissibility at bearing #4 remains at 0.3 up to an unbalanced force of 5694 N and then increases to 1.3.

# CHAPTER V
# STAGGERED ANALYSIS SCHEME

The computation time that is required to solve for the response of large order systems becomes prohibitive when an extended blade loss simulation result is desired. This gains even more importance when the analysis must be performed for many repetitions in an optimal parameter search. With this motivation, a new scheme was developed wherein the computational efficiency is greatly increased with a negligible loss in the accuracy of the solution.

## 5.1 Description of Staggered Analysis Scheme

In this scheme, the blade loss analysis is carried out using the Modal Truncation Augmentation method intermittently with thermal only regions between the thermo-mechanical regions. A thermal only region is defined as one where a constant power source is assumed and only the bearing thermal equations are integrated with a relatively large time step. A thermo-mechanical region is defined as on where the complete system equations and the bearing thermal equations are integrated simultaneously at each time step.

The assumption in formulating this scheme is that once the mechanical steady state is reached, there is no significant change in the response. Thus, a constant power loss (rms value for the last 5 cycles) is calculated and applied to the thermal only region. After the completion of the thermal only region, the final temperatures are applied back to the system which then calculates the thermal growth, change in viscosity, etc and performs time integration with the new values in thermo-mechanical region. This process can be used alternately several times to obtain an extended blade loss simulation for several minutes. The length of each of the thermal only and the thermo-mechanical regions is decided on a trial and error basis. Figure 5.1 shows the computational flow diagram used to implement this method.

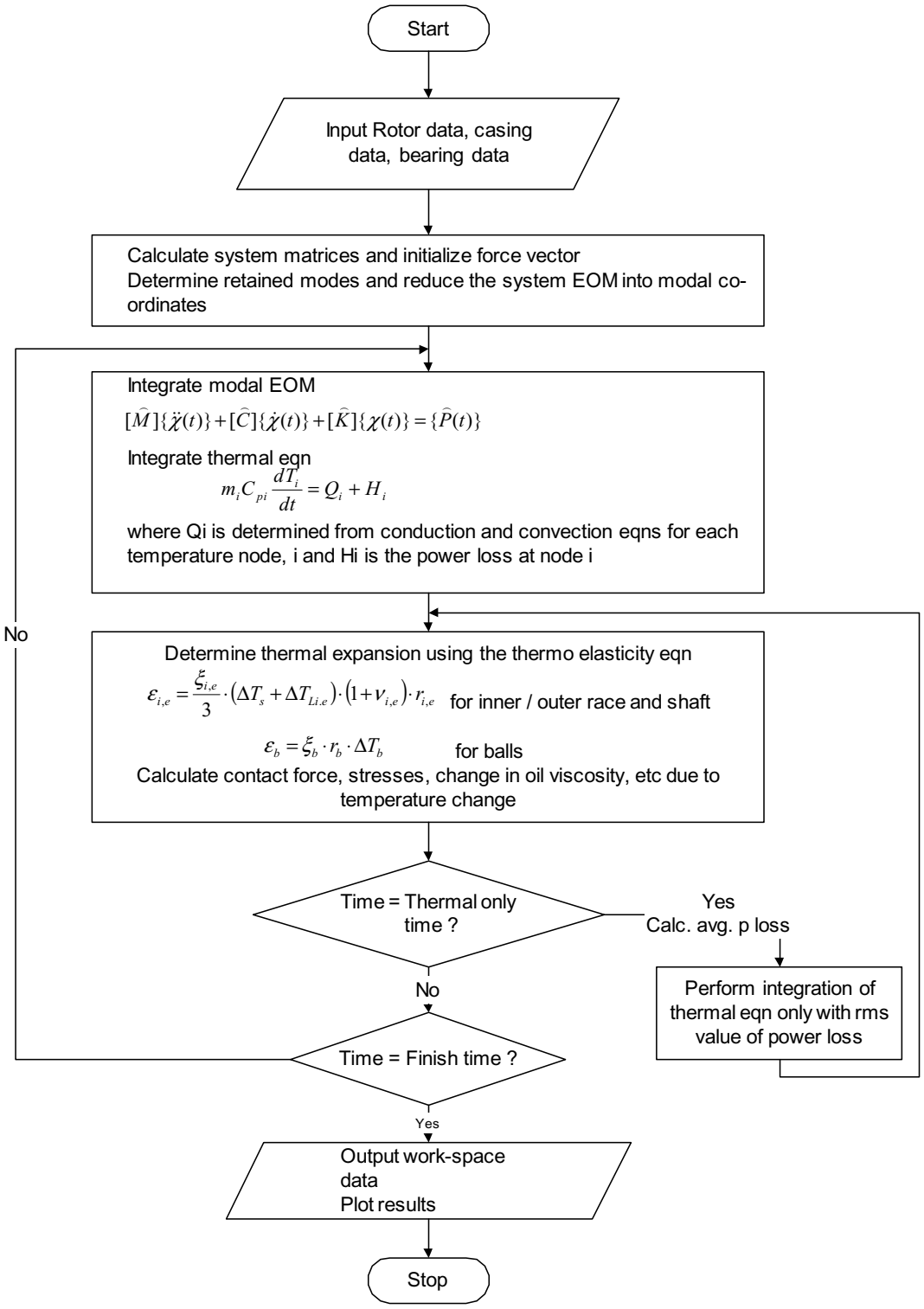


Figure 5.1. Computational flow diagram

## 5.2 Verification of Staggered Analysis Scheme

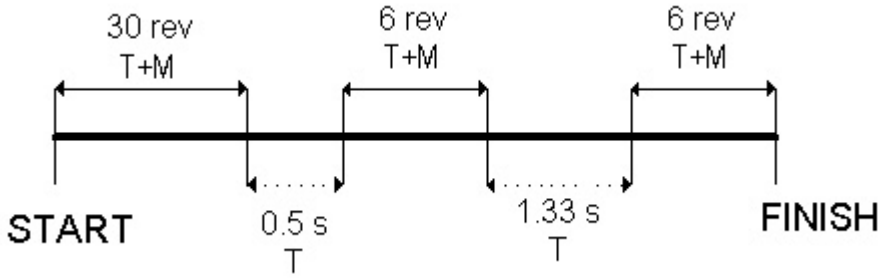


Fig.5.2 Staggered analysis scheme time line: --, Thermal only region; —, Thermo-mechanical region.

Figure 5.2 shows the time line used for the verification of the staggered analysis scheme. Since the results from this scheme had to be compared with the results from full integration, a short integration was performed for a total of 2 sec. Both the methods use a time step of 1E-6 sec in the thermo-mechanical region while it is 0.1 s in the thermal only region for the staggered analysis scheme. The power turbine is spinning at 18,000 rpm, while the gas turbine at 15,000 rpm with an imbalanced load of 500 lbs each applied at the second stage and mid of the power turbine. An initial temperature of 30 °C is used at all the temperature nodes.

### 5.2.1 Simulation Results with Thermo-Mechanical Integration

The following plots show some of the important results obtained from the Thermo-Mechanical only integration scheme.

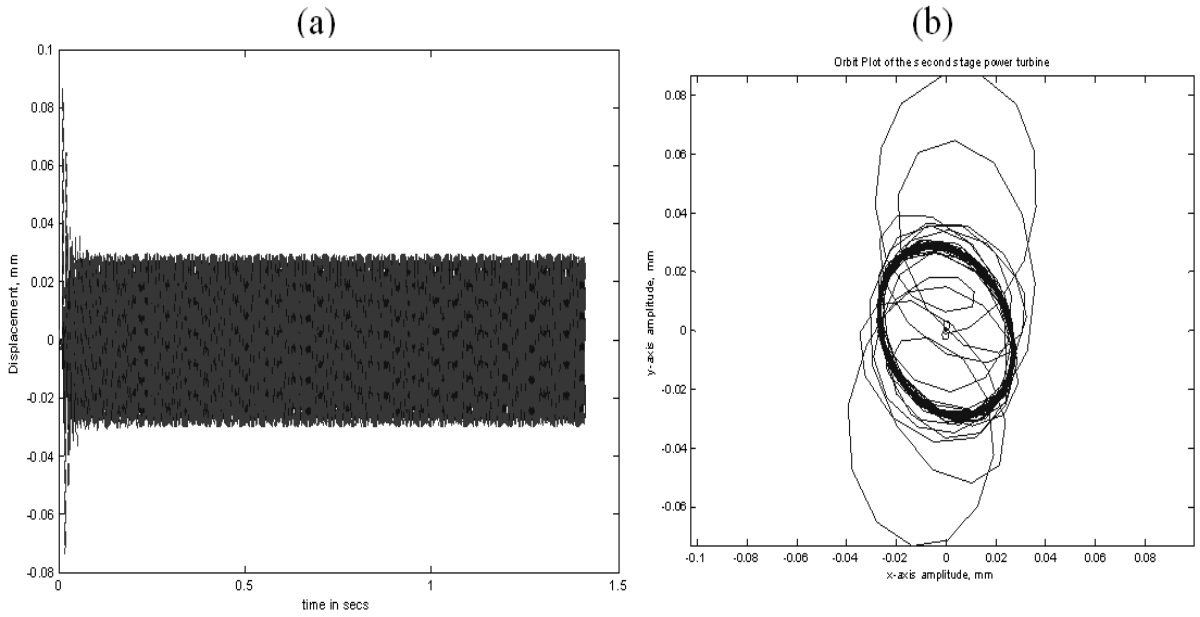


Fig. 5.3 (a) Transient response and (b) orbit plot of the second stage of the power turbine —, *y*-axis; - -, *z*-axis

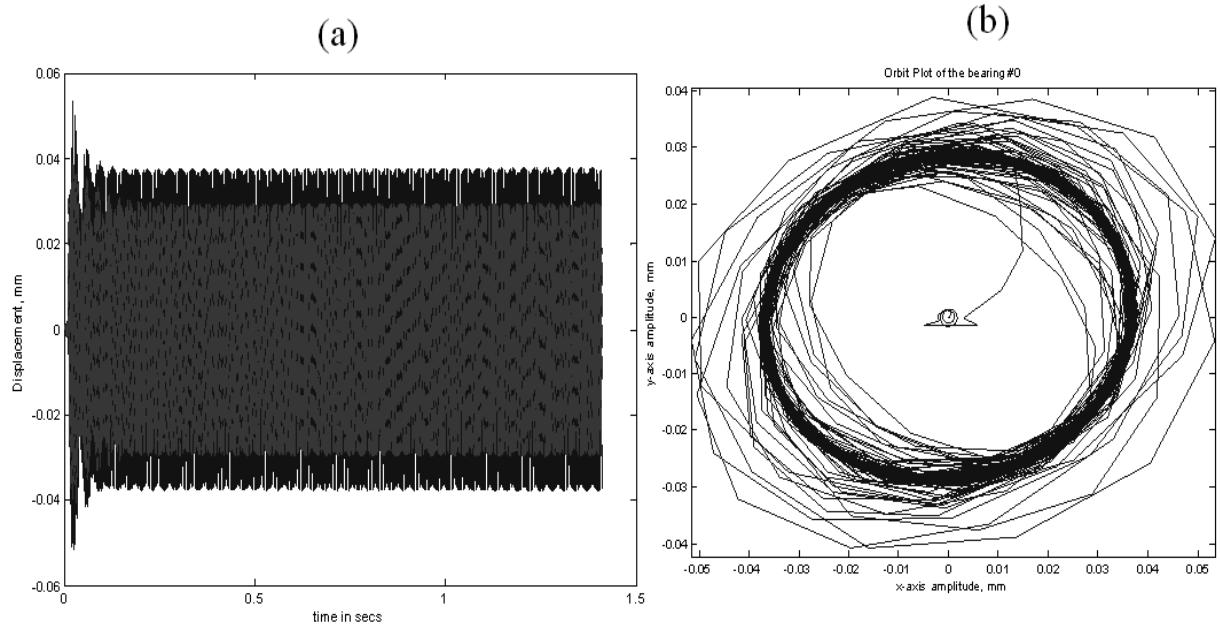


Fig. 5.4 (a) Transient response and (b) orbit plot at brg #0 :—, *y*-axis; - -, *z*-axis

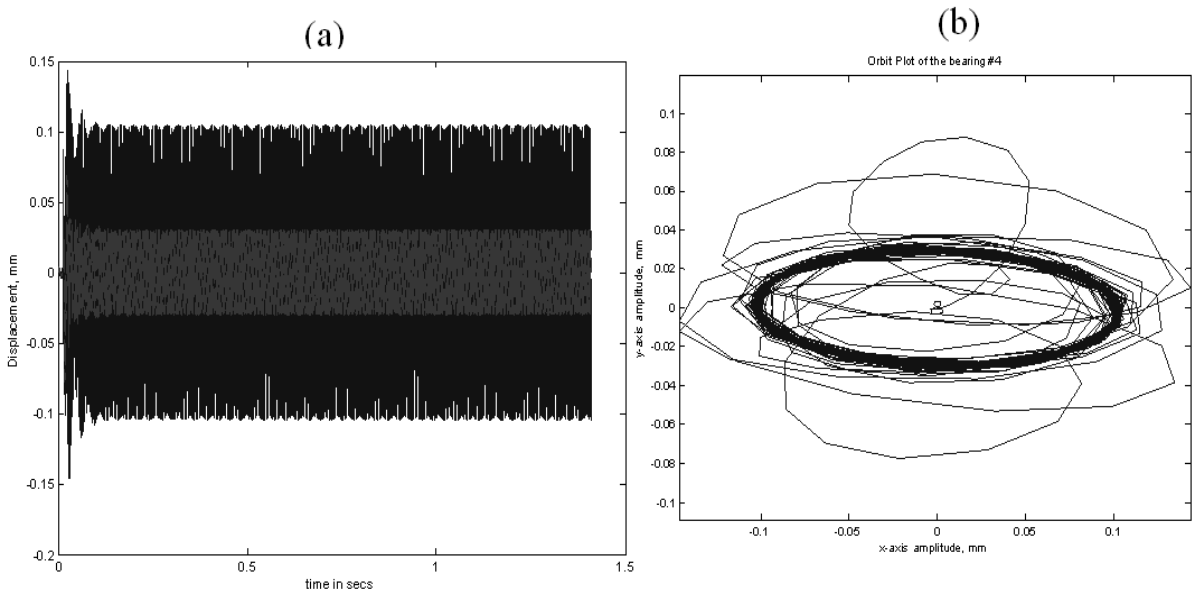


Fig. 5.5 (a) Transient response and (b) orbit plot at brg #4:—, *y*-axis; - -, *z*-axis

Figures 5.3, 5.4 and 5.5 show the transient response and the orbit plots of the second stage power turbine, bearing #0 and bearing #4 respectively. Since the imbalanced load is small, there is an initial transient and then it reaches the steady state very quickly. The power loss at bearing #4 is higher than that at bearing #0 as noticed in fig. 5.6. Figures 5.7 and 5.8 show the temperature plot of the bearing inner race, outer race, ball and oil. Since the imbalanced loads applied are closer to bearing #4 the temperatures are higher than that of bearing #0. This is also noticed in the transmissibility plot in fig 5.9.

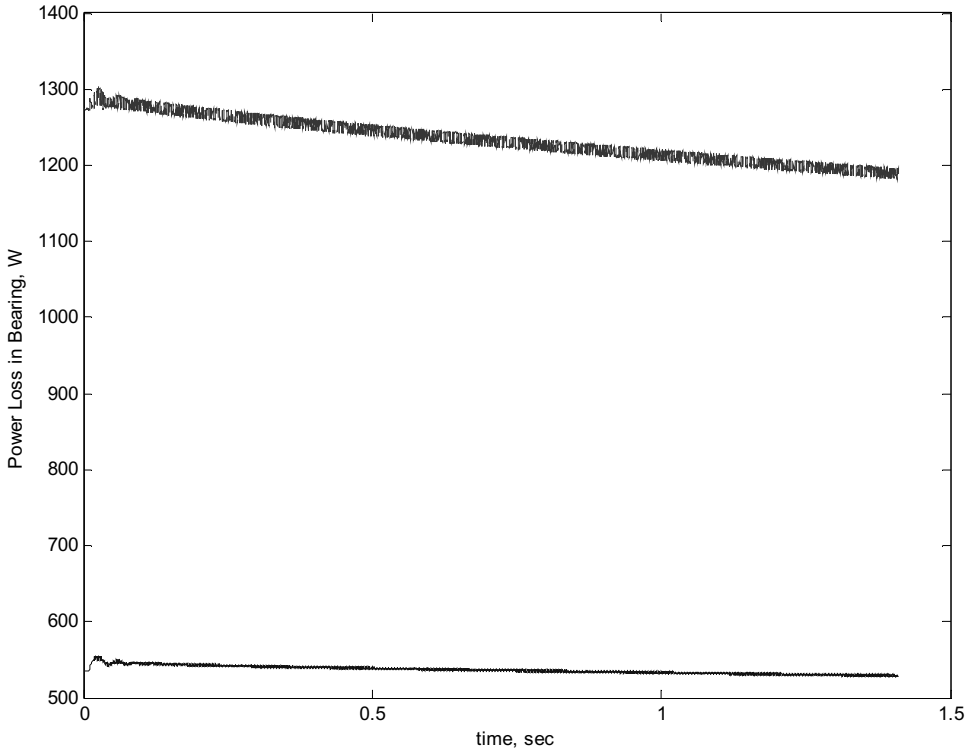


Fig 5.6 Power loss in: —, brg #0; - -, brg #4

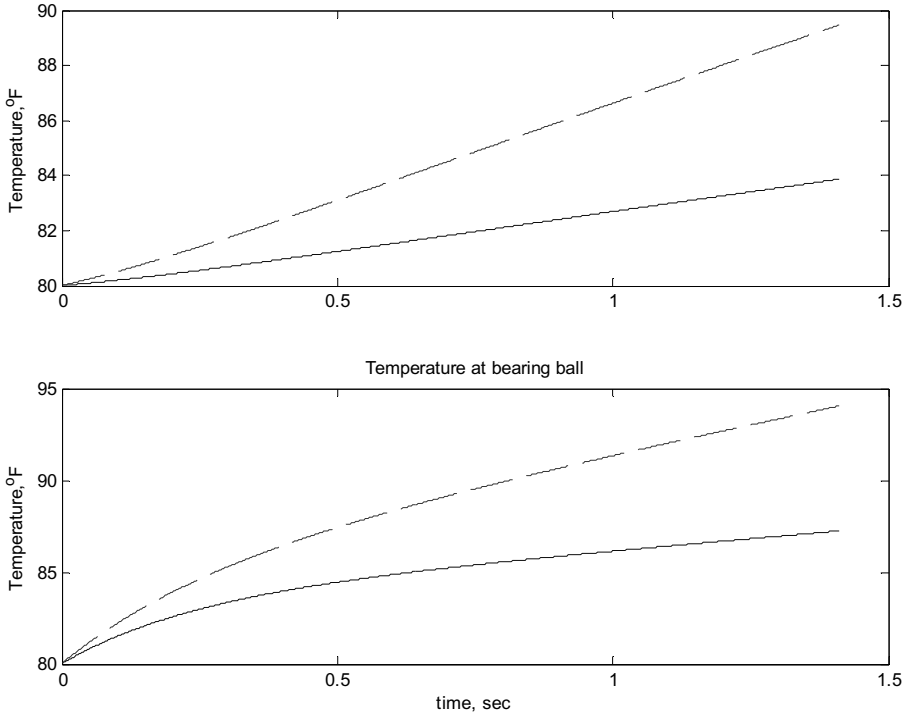


Fig 5.7 Temperature of bearing inner race and ball at: —, brg #0; - -, brg #4

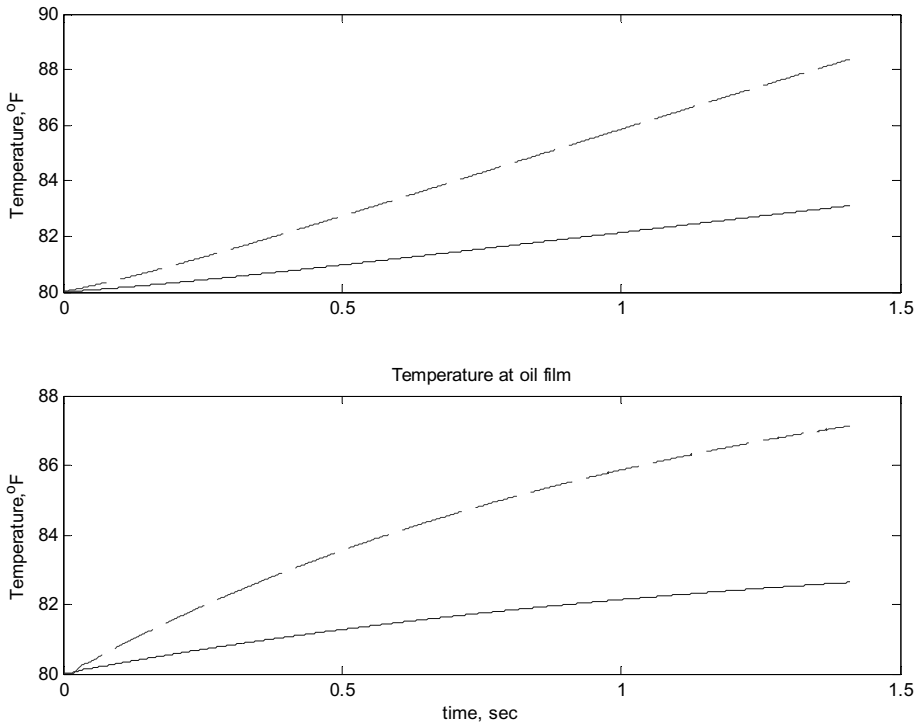


Fig 5.8 Temperature of bearing outer race and oil film at: —, brg #0; - -, brg #4

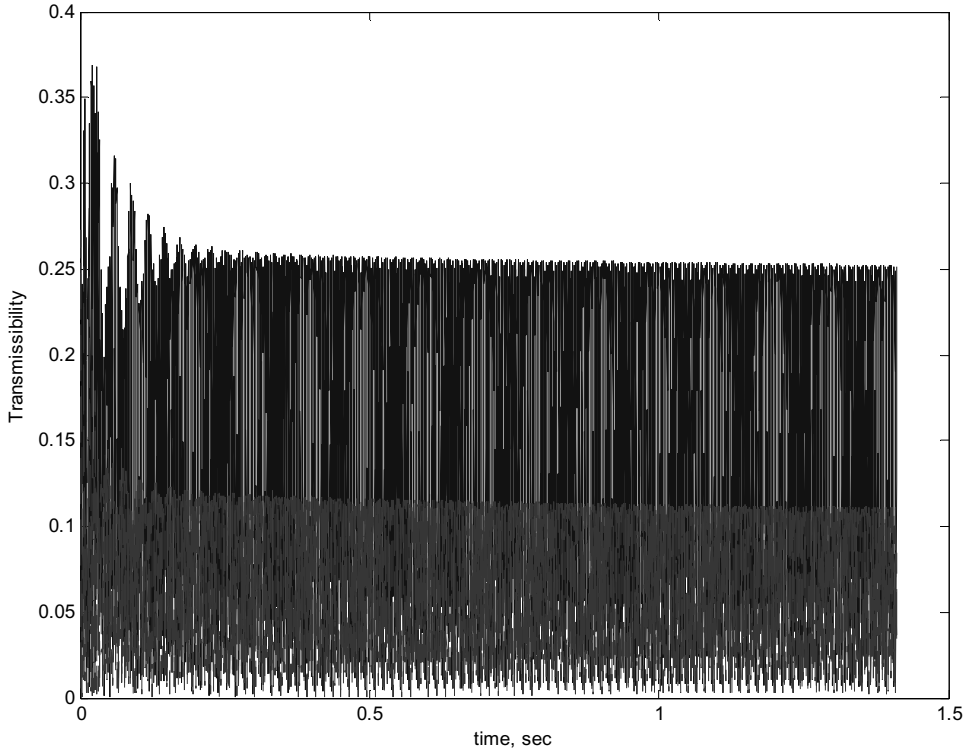


Fig 5.9 Transmissibility at: —, brg #0; - -, brg #4

### 5.2.2 Simulation Results Using Staggered Analysis Scheme

The following plots show some of the important results obtained from the Staggered Analysis scheme.

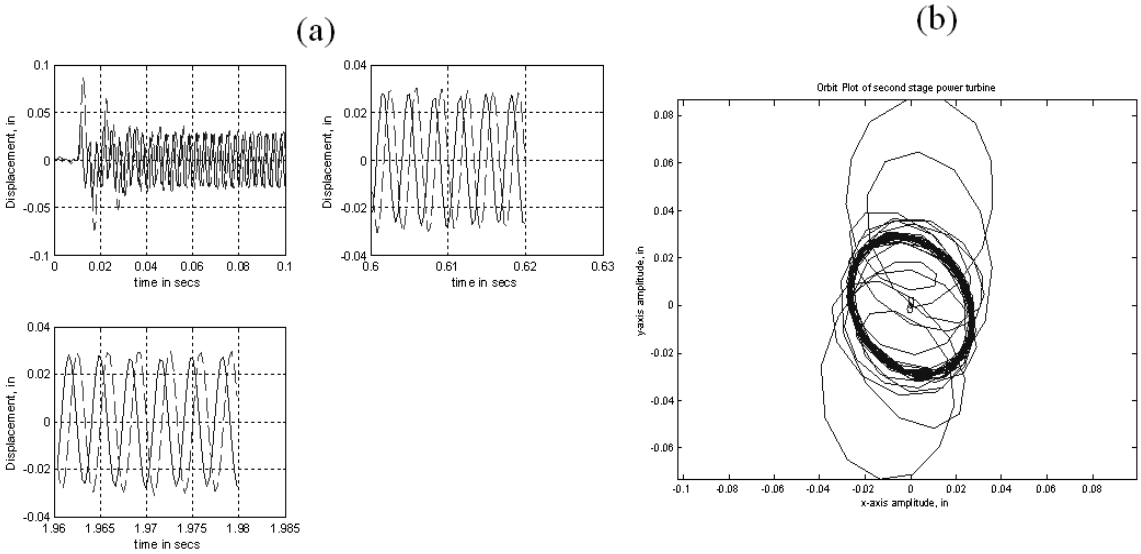


Fig. 5.10 (a) Transient response and (b) orbit plot of the second stage of the power turbine —, *y*-axis; - -, *z*-axis

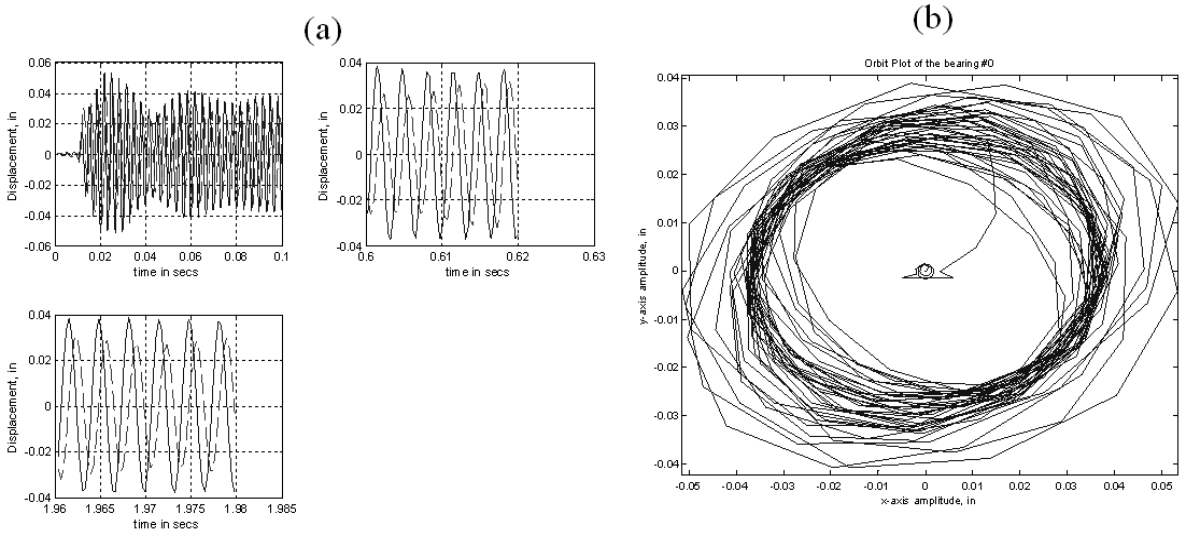


Fig. 5.11 (a) Transient response and (b) orbit plot of at brg #0 :—, *y*-axis; - -, *z*-axis

From fig. 5.10, 5.11 and 5.12 we see that the transient response plots and the orbit plots at all the main locations show very close concordance with the plots obtained in fig. 5.3, 5.4 and 5.5. Figure 5.13 shows the power loss in the bearing using the staggering effect. This also follows the non staggering plot in fig. 5.6 with an initial value of 1300 W and 550 W and dropping down to 1200 W and 500 W for bearing #4 and bearing #0 respectively.

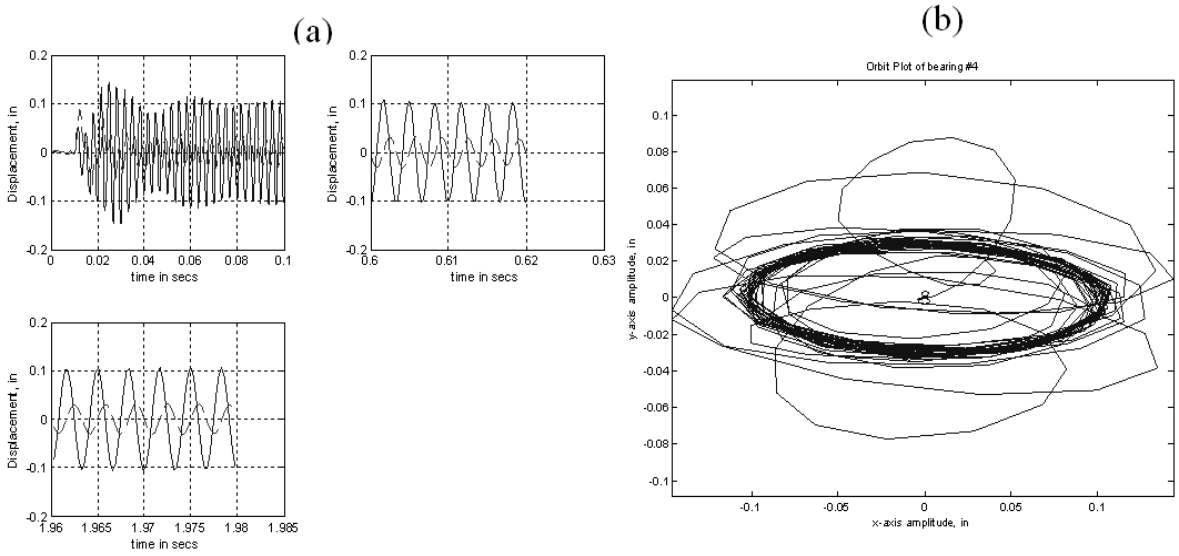


Fig. 5.12 (a) Transient response and (b) orbit plot at brg #4:—, *y*-axis; - -, *z*-axis

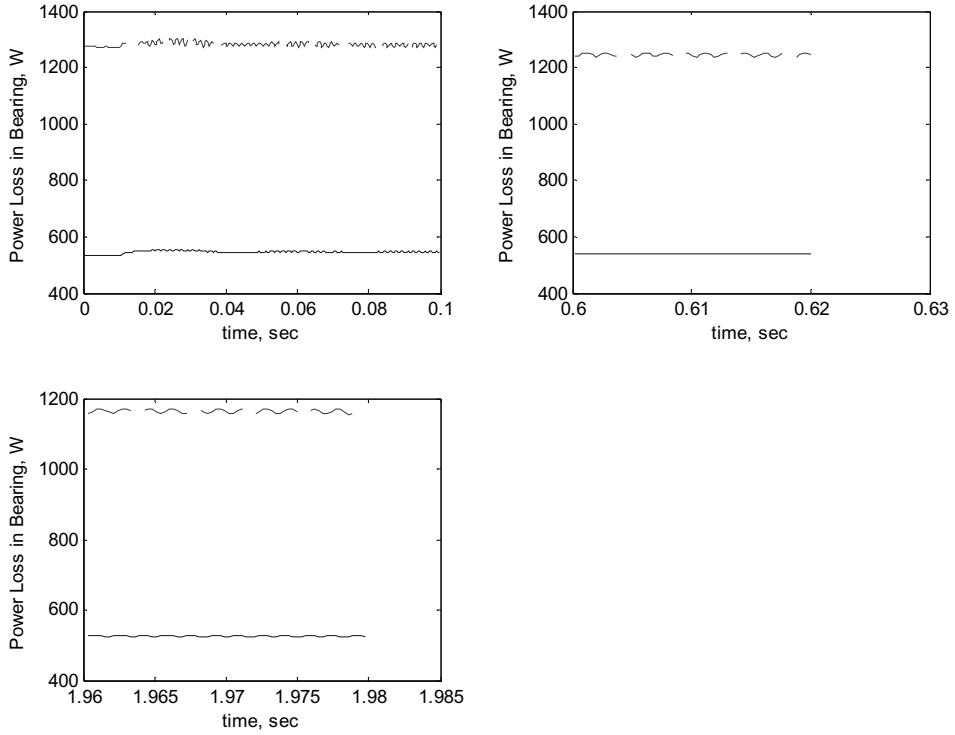


Fig 5.13 Power loss in: —, brg #0; - -, brg #4

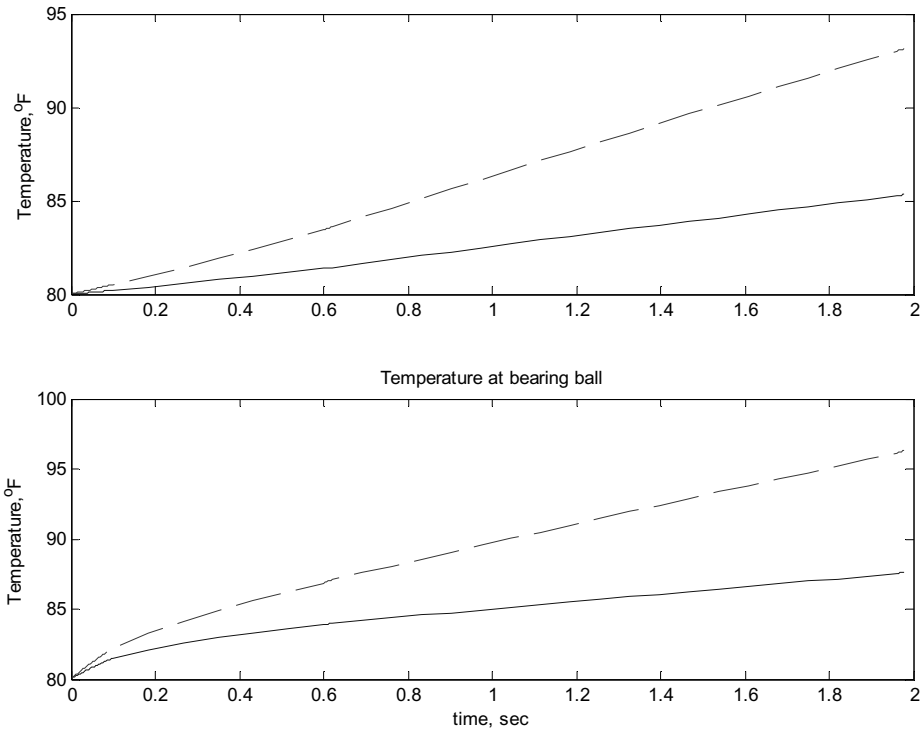


Fig 5.14 Temperature of bearing inner race and ball at: —, brg #0; - -, brg #4

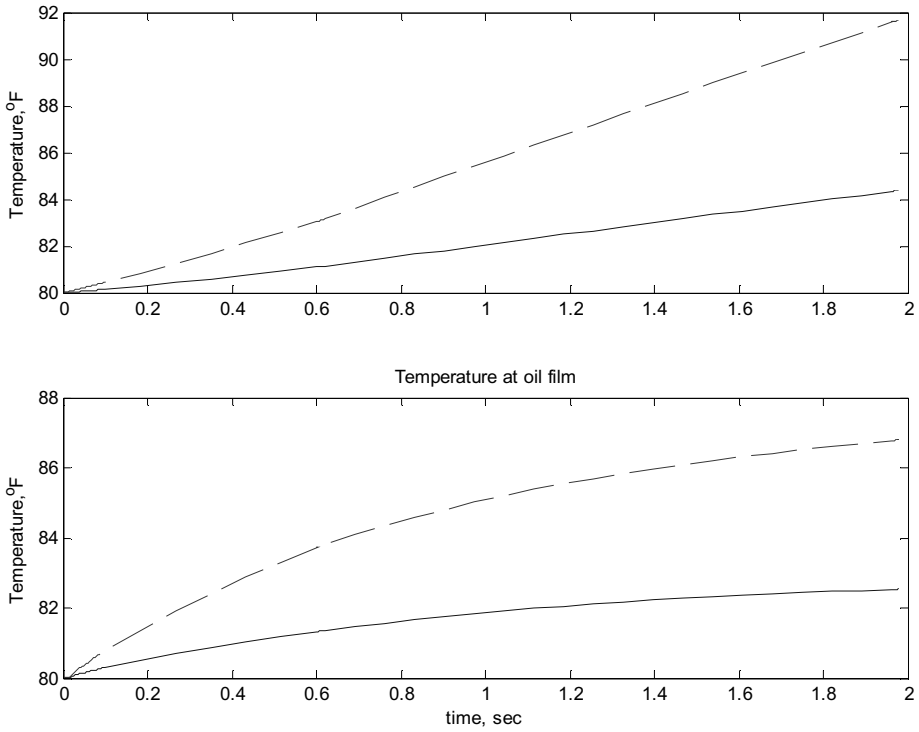


Fig 5.15 Temperature of bearing outer race and oil film at: —, brg #0; - -, brg #4

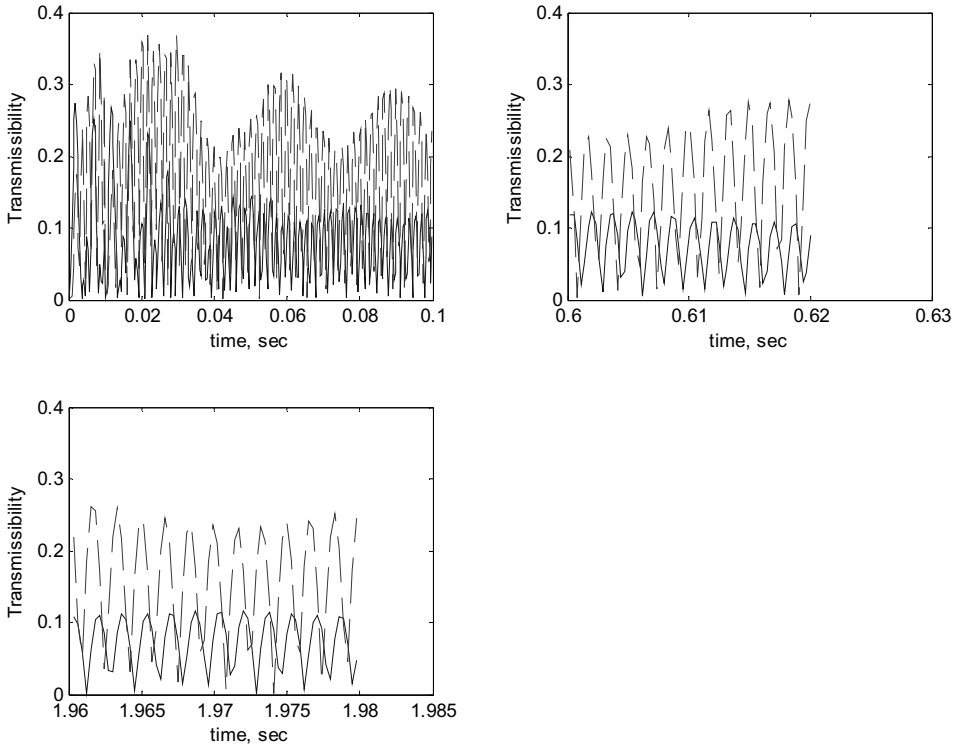


Fig 5.16 Transmissibility at: —, brg #0; - -, brg #4

Figures 5.14 and 5.15 show the temperature plot obtained by using the rms value of power loss in the thermal only region. Comparing the final values of the temperature with that obtained from the non staggering plot, we can say that the approximation of the power loss is not far from the true value. This is further proved by comparing the transmissibility plots of fig. 5.16 and 5.9.

### 5.2.3 Summary

The following table summarizes the results obtained from both the staggering and non staggering analysis at the power turbine bearing locations. From this, we can conclude that the staggering scheme can be applied to the present blade loss problem without any major loss in accuracy (less than 5 %) while improving the computational speed by almost 5 times.

Table 5.1 Comparison of Results between Staggered and Non Staggered Analysis

| **Simulation Results** | **Method Used** | | | |
|---|---|---|---|---|
| | **Full Integration** | | **Staggered Analysis** | |
| | **Bearing #0** | **Bearing #4** | **Bearing #0** | **Bearing #4** |
| Peak displacement of power turbine, mm | 0.0535 | 0.1435 | 0.0535 | 0.1435 |
| Steady-state displacement of power turbine, mm | 0.0377 | 0.1048 | 0.038 | 0.1055 |
| Maximum power loss in oil film, watt | 128.0 | 305.6 | 127.5 | 305.5 |
| Maximum power loss in bearing, watt | 555.45 | 1302.8 | 556.0 | 1302 |
| Peak Transmissibility | 0.28 | 0.37 | 0.273 | 0.37 |
| Steady State Transmissibility | 0.12 | 0.23 | 0.114 | 0.233 |
| Final temperatures, °F (Initial temperature is 80 °F) | | | | |
| Inner race | 85.4 | 93.2 | 85.3 | 93.12 |
| Ball | 88.6 | 97.5 | 87.6 | 96.3 |
| Outer race | 84.4 | 91.75 | 84.3 | 91.66 |
| Oil film | 83.1 | 88.3 | 82.5 | 86.8 |
| Time Taken*, hrs | 24.8 hrs | | 4.65 hrs | |

* - On a P3 Intel 933 MHz processor with 512 MB RAM.

# CHAPTER VI
# HOUSING, CONTACT AND THERMAL MODEL

In the previous chapters, all the bearings except the inter shaft bearings were connected to the ground. But in reality, this is not true since the rotors and bearings are enclosed in a flexible housing which in turn is connected to the aircraft wing. Also, seals are built into the model which rubs against the rotor during high imbalanced load to protect the bearings. Hence, in this chapter both the flexible housing and seal rub is included into the model.

## 6.1 Description of Flexible Housing

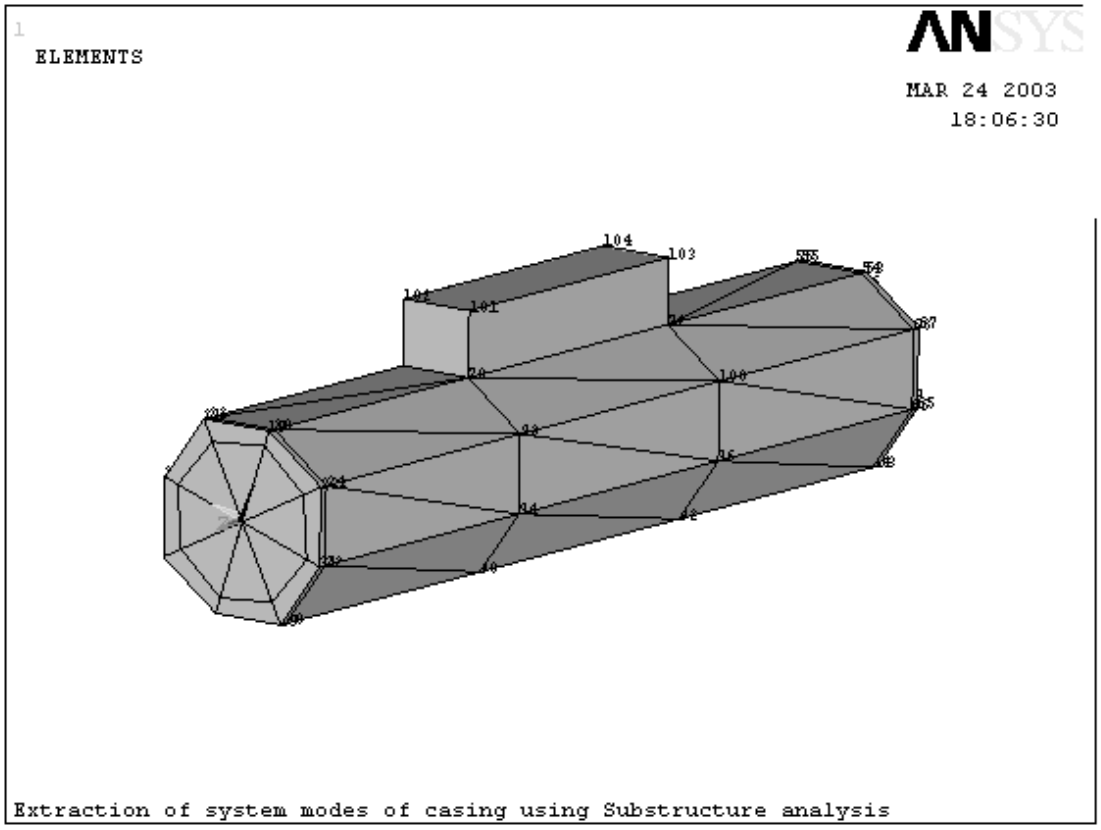


Fig 6.1. Flexible housing from ANSYS

The housing is built using 104 SOLID45 (8 node solid element with 3 DOF at each node), 8 BEAM4 (2 node 3D elastic beam with 6 DOF at each node) and 6 COMBIN14 (longitudinal spring – damper element) elements (Refer Appendix B for ANSYS element description). It consists of a total of 118 nodes with a total of 342 degrees of freedom. The housing has a diameter of 10 in, length of 57 in with a wall thickness of 0.25 in. The top face of the housing is rigidly fixed i.e. all DOF at all nodes on top face is zero. The material constants used for the housing are:

Young's Modulus, $E = 3E7\,psi = 2.06E11N/m^2$

Density, $\rho = 7832kg/m^3 = 0.283lb/in^3$

Poisson's Ratio, $\upsilon = 0.3$

### 6.1.1 Casing Undamped Modes from ANSYS

Figures 6.2 to 6.6 show the first few undamped modes less than 110,000 rpm that are imported from ANSYS since they are the contributing modes. They are shown below.

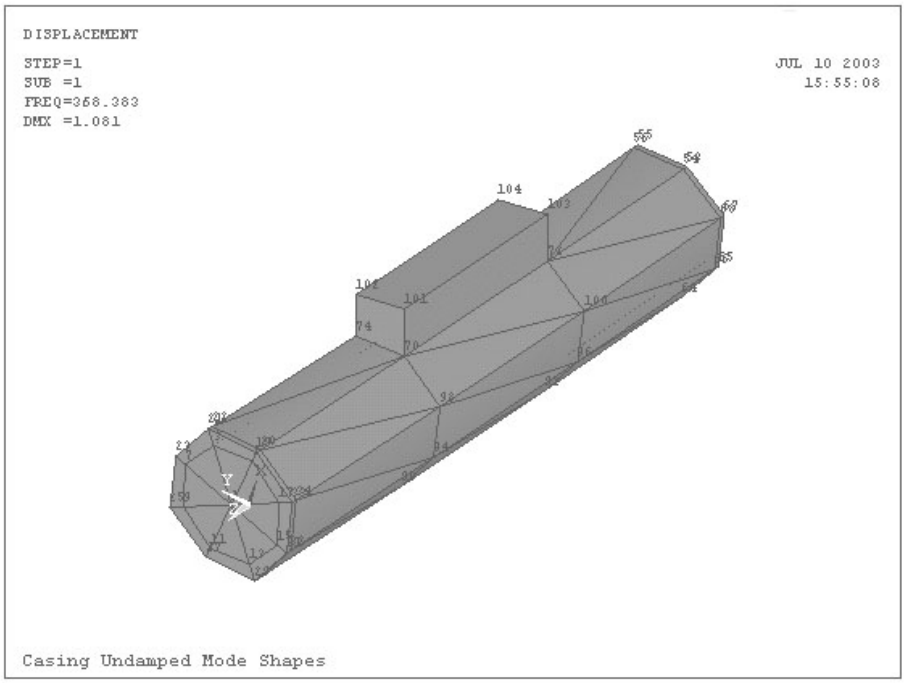


Fig 6.2 Casing undamped mode at N = 22,103 RPM

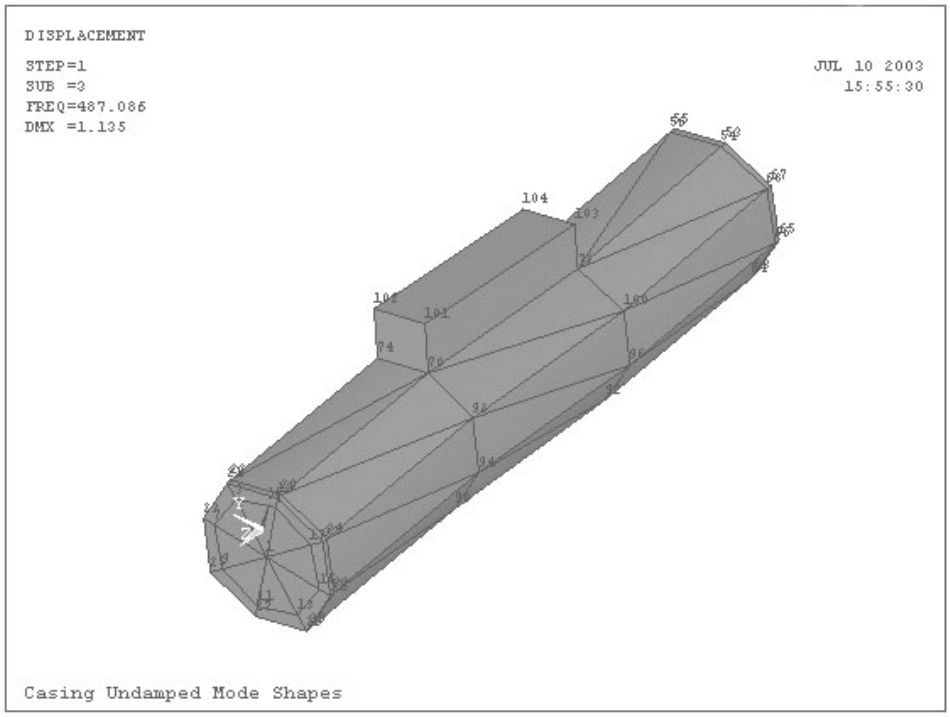


Fig 6.3 Casing undamped mode at N = 29,225 RPM

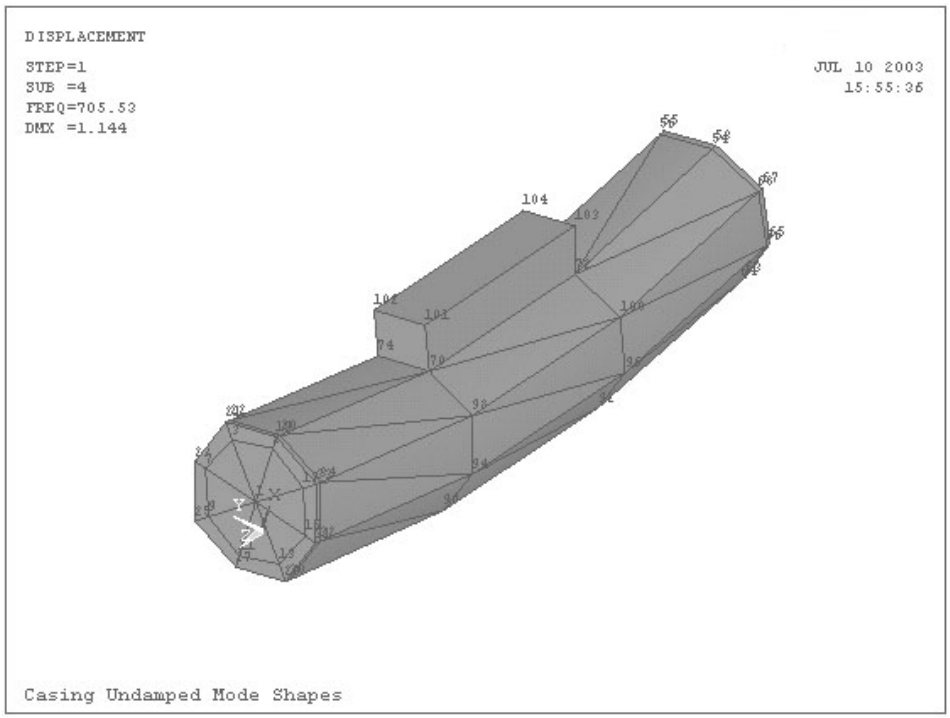


Fig 6.4 Casing undamped mode at N = 42,332 RPM

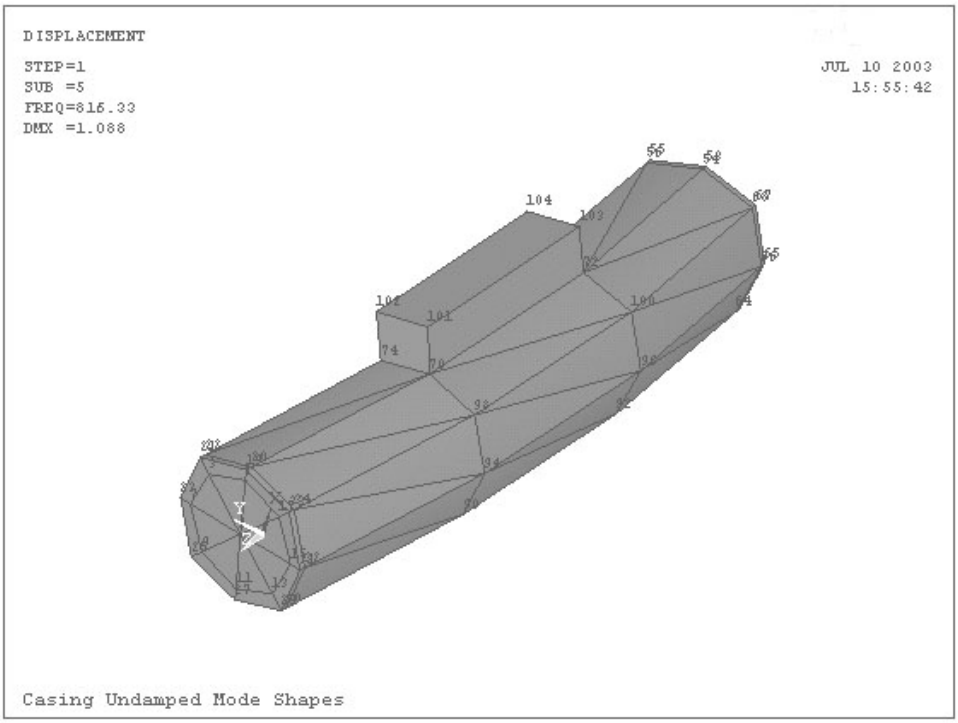


Fig 6.5 Casing undamped mode at N = 48,980 RPM

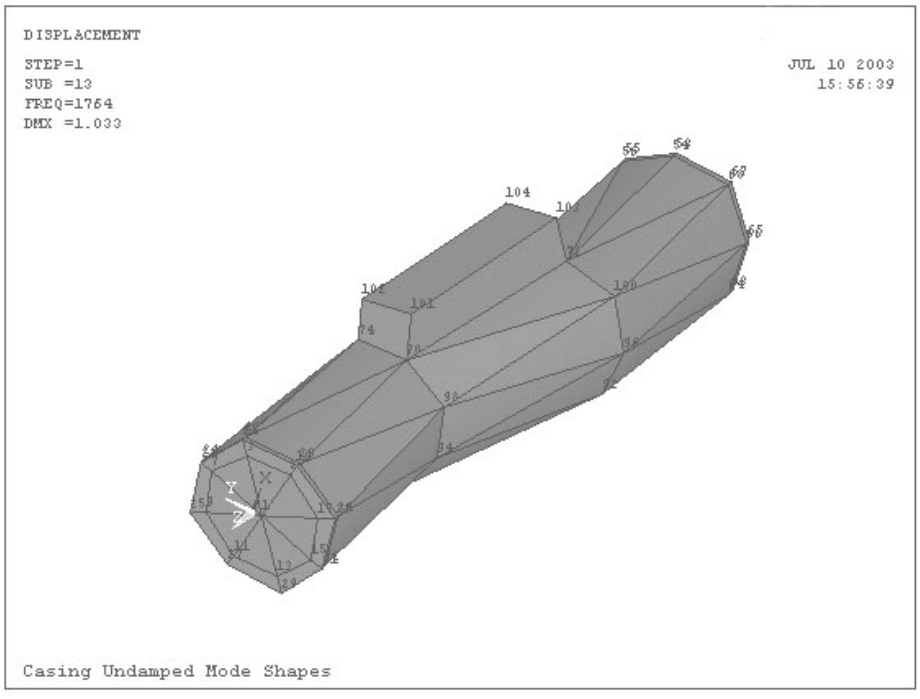


Fig 6.6 Casing undamped mode at N = 105,840 RPM

## 6.2 Seal Rub Contact Model

Rotor rub against a non rotating part generates a very complex rotor vibration, which may lead to total destruction of the machine in merely a few rotations. The most common type of rub in rotating machinery is blade tip and seal rub both of which can be caused by thermal expansion.

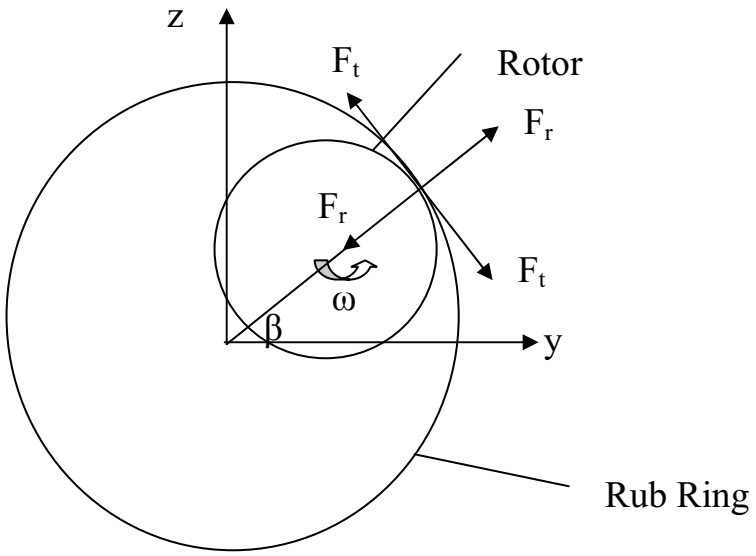


Fig 6.7 Rub ring contact model

The figure shows the rub ring contact model based on a modified Hertzian contact force and equivalent damping used in this problem [16]. The radial displacement from the rotor center and its derivative is given by:

$$\delta = \sqrt{Y_r^2 + Z_r^2} - C \qquad 6.1$$

where

$Z_r, Y_r,$- Radial rotor displacement

C – Rub ring clearance

$$\dot{\delta} = \frac{Y_r \dot{Y}_r + Z_r \dot{Z}_r}{\delta + C} \qquad 6.2$$

The radial contact force and the tangential force is given by:

$$F_r = k_l \delta^{\frac{10}{9}} (1.5\alpha\dot{\delta} + 1) \qquad 6.3$$

where

$k_l = 1.14 \times 10^7 (l_c)^{0.8}$ ; $l_c$ – Contact length

α = 0.002 ~ 0.008 for steel on steel rub

$$F_t = \mu F_c \qquad 6.4$$

where

μ – Co efficient of friction = 0.1

The forces are resolved into the y and z directions as:

$$\beta = \tan^{-1}\left(\frac{Z_r}{Y_r}\right)$$

$$F_y = -F_c \cos\beta + F_t \sin\beta \qquad 6.5$$

$$F_z = -F_c \sin\beta - F_t \cos\beta$$

These forces are added to the right hand side of the equations of motion at the appropriate degrees of freedom. The Power Loss due to the rub is defined as:

$$H_r = F_t r \omega \qquad 6.6$$

where $r$ – radius at the rub location

$\omega$ – Speed of the rotor, rad/s

## 6.3 Thermal Model

Actual heat transfer in a bearing needs 3 dimensional analysis but assuming that the heat flux is uniform in the radial direction and symmetric to the axial direction one dimensional radial heat transfer equations are developed using bulk heat masses. The heat transfer in the equations is described by thermal resistances as the connectors between interested temperature nodes. Crucial temperature nodes in the cross-section of an angular contact ball bearing supported on SFD are shown in Fig.6.8. The length $L_s$ is the distance from the axial center of inner race to the end of rotor and the lengths $L_j$, $L_h$

denote the axial length of the SFD journal and housing, respectively. The widths $w_i$, $w_e$ of inner and outer rings are assumed to be same.

Figure 6.9 shows the heat transfer network of the ball bearing with grease packed, which consists of the thermal resistances and heat sources. The heat sources $H_{i,e}$ and the heat source $H_{sf}$ due to viscous dissipation energy in fluid film is obtained from [10]. $H_r$ is the power loss due to rub which is obtained from Eqn. 6.6.

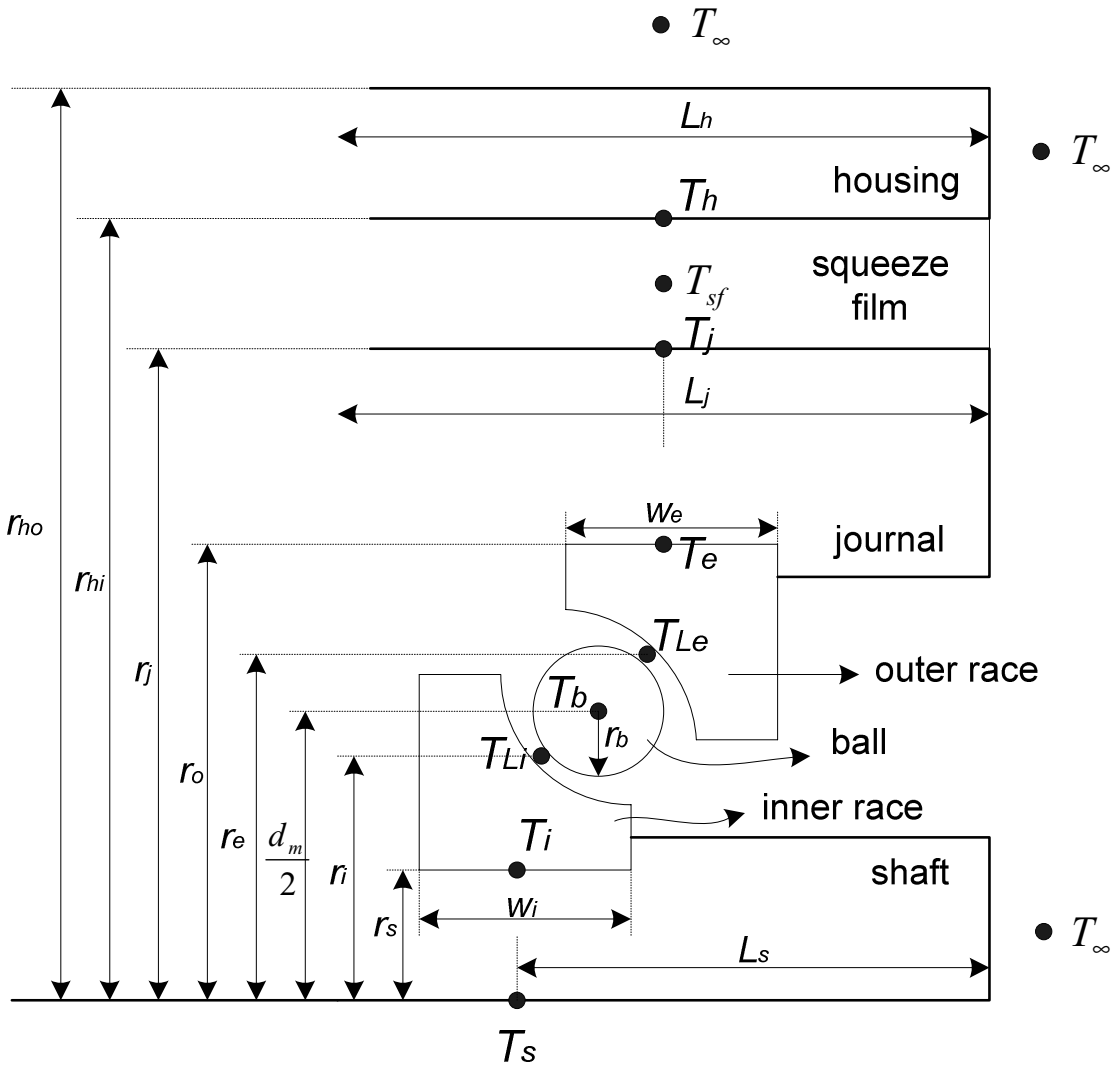


Fig. 6.8 Cross-sectioned bearing with thermal nodes

In addition, the following assumptions are utilized in modeling:

(a) Heat generation from the contacts acts on shaft, balls, inner race and outer race.

(b) Ball bearing is modeled with lumped heat mass elements.

(c) Each heat mass has uniform temperature distribution.

(d) Conduction heat transfer through fluid film.

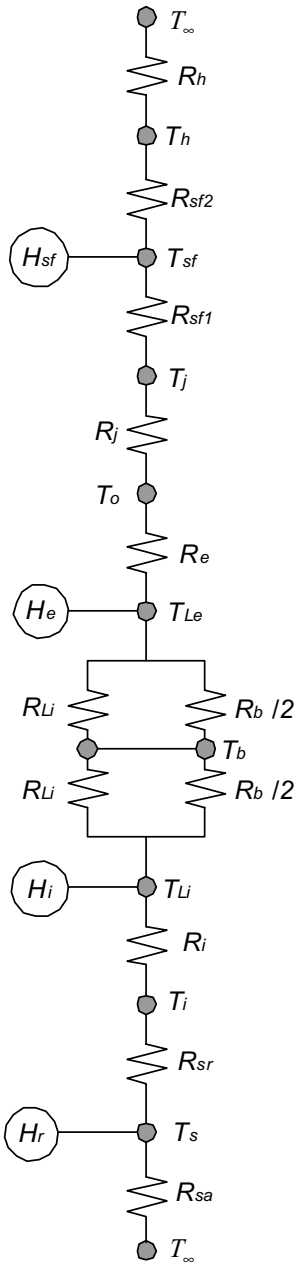


Fig. 6.9 Heat transfer network

The thermal resistances are a function of material properties, geometry and heat transfer mode. For instance, the thermal resistance $R_i$ between the inner race contact with balls and inner race bore radius is obtained as follows. The radial heat flow of a cylinder of inside radius $r_s$, outside radius $r_i$ and length $w_i$ can be described as

$$q = kA\frac{dT}{dr} \tag{6.7}$$

or $$q = k2\pi r w_i \frac{dT}{dr} \tag{6.8}$$

where $k$ is the thermal conductivity of the cylinder and $A$ is the area normal to temperature gradient. Eqn. 6.8 has the boundary conditions as

$$T = T_i \qquad \text{at } r = r_s \tag{6.9}$$

$$T = T_{Li} \qquad \text{at } r = r_i \tag{6.10}$$

Since the heat flow at any radial location is same, integrating Eqn. 6.9 becomes

$$\int_{r=r_s}^{r=r_i} q\frac{1}{r}dr = 2\pi w_i k \int_{T=T_i}^{T=T_{Li}} dT$$

or

$$q \cdot \ln(r_i/r_s) = 2\pi k w_i (T_{Li} - T_i) \tag{6.11}$$

Rearranging Eqn. 6.11

$$q = \frac{T_{Li} - T_i}{\frac{\ln(r_i/r_s)}{2\pi k w_i}} = \frac{T_{Li} - T_i}{R_i} \tag{6.12}$$

The electrical analogy can be used to express the relationship between the temperature node and thermal resistance as shown in Fig. 6.10. Table 6.1 shows the thermal resistances in the thermal heat network.

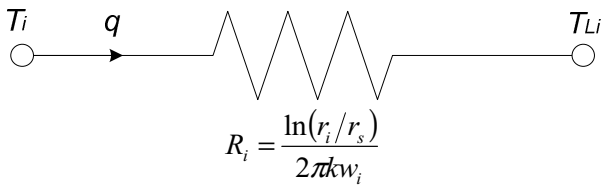


Fig. 6.10 1D radial heat flow through cylinder and electrical analogy

Table 6.1 Thermal Resistances of Heat Transfer Network

| **Ball/lubricant** | **Inner race/ shaft** | **Outer race/journal** |
|---|---|---|
| $R_{Li} \approx \frac{r_b}{k_l(2\pi r_i W_i - \pi n r_b^2)}$ | $R_i = \frac{\ln\left(r_i / r_s\right)}{2\pi k_i W_i}$ | $R_e = \frac{\ln\left(r_o / r_e\right)}{2\pi k_e W_e}$ |
| $R_{Le} \approx \frac{r_b}{k_l(2\pi r_e W_e - \pi n r_b^2)}$ | $R_{sr} = \frac{1}{\pi k_s W_i}$ | $R_j = \frac{\ln\left(r_j / r_o\right)}{2\pi k_j W_e}$ |
| $R_b \approx \frac{1}{n k_b \pi r_b}$ | $R_{sa} = \frac{L_s}{k_s \pi r_s^2} + \frac{1}{h_s \pi r_s^2}$ | $R_h = \frac{R_{hr} R_{ha}}{R_{hr} + R_{ha}}$ |
| **SFD** | **Housing** | |
| $R_{sf1} = \frac{\ln\left((r_j + c_{sf}/2) / r_j\right)}{2\pi k_{sf} L_j}$ | $R_{hr} = \frac{\ln\left(r_h / r_o\right)}{2\pi k_h L_h} + \frac{1}{h_h 2\pi r_h L_h}$ | |
| $R_{sf2} = \frac{\ln\left(r_{hi} / (r_j + c_{sf}/2)\right)}{2\pi k_{sf} L_j}$ | $R_{ha} = \frac{L_h}{2\pi k_h (r_h^2 - r_o^2)} + \frac{1}{\pi h_h (r_h^2 - r_o^2)}$ | |

Free convection coefficient $h$ [21] is approximated as a function of the relative temperatures, which is

$$h = 23 \cdot \left(T - T_\infty\right)^{0.25} \text{ [W/m}^2\text{-°C]} \qquad 6.13$$

From the heat transfer network and heat sources a thermal equation of motion is developed. For the inner and outer races, half the mass is used to represent temperature node. To consider convection heat transfer at the axial end of rotor and the ends of housing, small heat mass is assigned to these locations and the convection coefficient $h$ is changed according to the temperature difference.

The equation for the axial end of rotor is

$$m_{s1}C_{ps}\frac{dT_{s1}}{dt}=-\frac{T_{s1}-T_s}{R_{sac}}-\frac{T_{s1}-T_\infty}{R_{sacv}} \tag{6.14}$$

where $m_{s1}$ is the heat mass, $C_p$ the specific heat and $T_\infty$ the ambient temperature. $R_{sac}$, $R_{sacv}$ are the conduction and convection thermal resistances of $R_{sa}$, respectively.

The thermal equations for the nodes $T_s$ to $T_{sf}$ are

$$m_sC_{ps}\frac{dT_s}{dt}=-\frac{T_s-T_i}{R_{sr}}-\frac{T_s-T_{s1}}{R_{sac}} \tag{6.15}$$

$$\frac{m_i}{2}C_{pi}\frac{dT_i}{dt}=-\frac{T_i-T_s}{R_{sr}}-\frac{T_i-T_{Li}}{R_i} \tag{6.16}$$

$$\frac{m_i}{2}C_{pi}\frac{dT_{Li}}{dt}=-\frac{T_{Li}-T_i}{R_i}-\frac{T_{Li}-T_b}{R_1}+\frac{H_i}{2} \tag{6.17}$$

$$m_bC_{pb}\frac{dT_b}{dt}=-\frac{T_b-T_{Li}}{R_1}-\frac{T_b-T_{Le}}{R_2}+\frac{H_i}{2}+\frac{H_e}{2} \tag{6.18}$$

$$\frac{m_e}{2}C_{pe}\frac{dT_{Le}}{dt}=-\frac{T_{Le}-T_b}{R_2}-\frac{T_{Le}-T_e}{R_e}+\frac{H_e}{2} \tag{6.19}$$

where the thermal resistances $R_1=\dfrac{R_{Li}R_b/2}{R_{Li}+R_b/2}$ and $R_2=\dfrac{R_{Le}R_b/2}{R_{Le}+R_b/2}$.

$$\frac{m_e}{2}C_{pe}\frac{dT_e}{dt}=-\frac{T_e-T_{Le}}{R_e}-\frac{T_e-T_j}{R_j} \tag{6.20}$$

Assuming the heat generation due to viscous dissipation in the squeeze film is provided only to oil film,

$$m_jC_{pj}\frac{dT_j}{dt}=-\frac{T_j-T_e}{R_j}-\frac{T_j-T_{sf}}{R_{sf1}} \tag{6.21}$$

$$m_{sf}C_{psf}\frac{dT_{sf}}{dt}=-\frac{T_{sf}-T_j}{R_{sf1}}-\frac{T_{sf}-T_h}{R_{sf2}}+H_{sf} \tag{6.22}$$

The thermal equation for the housing is

$$m_hC_{ph}\frac{dT_h}{dt}=-\frac{T_h-T_{sf}}{R_{sf2}}-\frac{T_h-T_{ha}}{R_{hac}}-\frac{T_h-T_{hr}}{R_{hrc}} \tag{6.23}$$

where $T_{ha}$, $T_{hr}$ are the temperatures at the axial and radial ends of the housing, respectively, and $R_{hac}$, $R_{hrc}$ are the conduction thermal resistances in the axial and radial directions, respectively.

The thermal equations for the ends of the housing are

$$m_{ha}C_{ph}\frac{dT_{ha}}{dt} = -\frac{T_{ha}-T_h}{R_{hac}} - \frac{T_{ha}-T_\infty}{R_{hacv}} \tag{6.24}$$

$$m_{hr}C_{ph}\frac{dT_{hr}}{dt} = -\frac{T_{hr}-T_h}{R_{hrc}} - \frac{T_{hr}-T_\infty}{R_{hrcv}} \tag{6.25}$$

where $R_{hacv}$, $R_{hrcv}$ are the convection thermal resistances of $R_{ha}$, $R_{hr}$, each.

Since the temperature node $T_s$ at one rotor end is connected to the temperature node $T_{s'}$ at the other end in the heat transfer network, Eqn. 6.15 should be updated to

$$m_sC_{ps}\frac{dT_s}{dt} = -\frac{T_s-T_i}{R_{sr}} - \frac{T_s-T_{s1}}{R_{sac}} - \frac{T_s-T_{s'}}{R_{sc}} \tag{6.26}$$

where the thermal resistance $R_{sc}$ is described using the average rotor radius $\bar{r}$ and distance $L$ between two nodes as

$$R_{sc} = \frac{L}{k_s\pi\bar{r}^2} \tag{6.27}$$

Figure 6.11 shows the full thermal model used for the power turbine rotor.

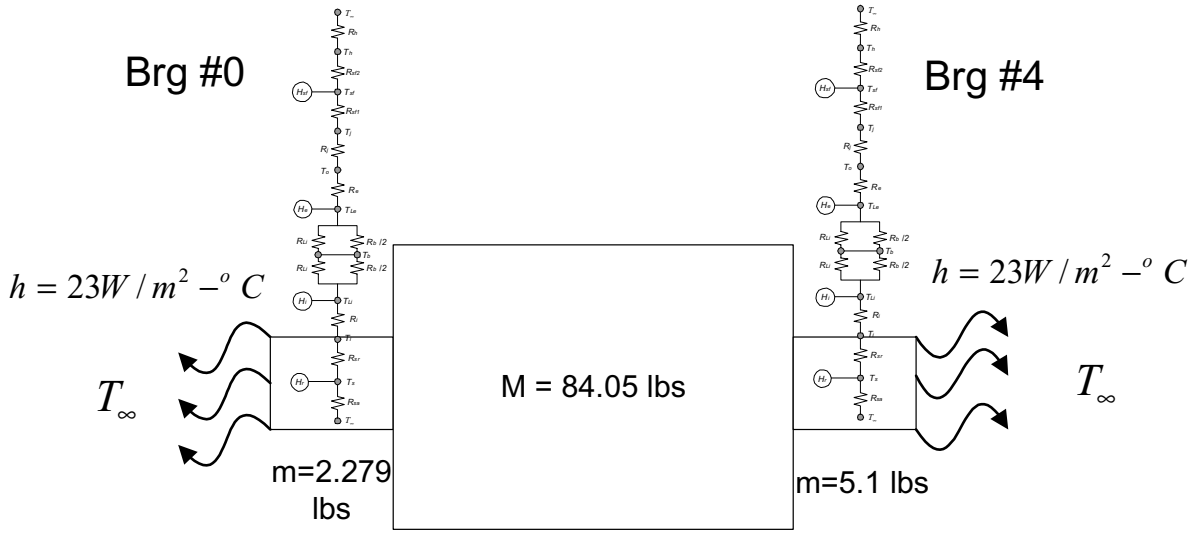


Fig 6.11 Full thermal model for power turbine rotor

The thermal expansion of a hollow cylinder with temperature distribution $T(r)$ in the radial direction is estimated using [21]. Assuming the temperature distribution is linear the thermal expansion $\varepsilon_e$ of the outer race and SFD journal is given by

$$\varepsilon_{i,e} = \frac{\xi_{i,e}}{3} \cdot \left(\Delta T_s + \Delta T_{Li.e}\right) \cdot \left(1 + \nu_{i,e}\right) \cdot r_{i,e} \tag{6.28}$$

where $\xi_e$ [m/m-°C] is the thermal expansion coefficient of the outer race, $\nu_e$ is the Poisson's ratio and $\Delta T$ indicates the temperature increase from an initial value.

The thermal expansion of a ball with uniform temperature is

$$\varepsilon_b = \xi_b \cdot r_b \cdot \Delta T_b \tag{6.29}$$

where $r_b$ is the ball radius.

The thermal expansions of the bearing components are substituted into the calculation of contact forces. From the geometric relationship between the ball, inner race and outer race,

$$\tan\alpha_i = \frac{l_{oi}\sin\alpha_o + u_z - v_z}{l_{oi}\cos\alpha_o + u_r + \varepsilon_i - v_r} \tag{6.30}$$

$$\tan\alpha_e = \frac{l_{oe}\sin\alpha_o + v_z - w_z}{l_{oe}\cos\alpha_o + v_r - w_r - \varepsilon_e} \tag{6.31}$$

$$l_i = \varepsilon_b + \sqrt{\left(l_{oi}\cos\alpha_o + u_r + \varepsilon_i - v_r\right)^2 + \left(l_{oi}\sin\alpha_o + u_z - v_z\right)^2} \tag{6.32}$$

$$l_e = \varepsilon_b + \sqrt{\left(l_{oe}\cos\alpha_o + v_r - w_r - \varepsilon_e\right)^2 + \left(l_{oe}\sin\alpha_o + v_z - w_z\right)^2} \tag{6.33}$$

$$\delta_i = l_i - l_{oi} - \Delta_i \tag{6.34}$$

$$\delta_e = l_e - l_{oe} - \Delta_e \tag{6.35}$$

Figure 6.12 describes the geometric parameters used in the above equations.

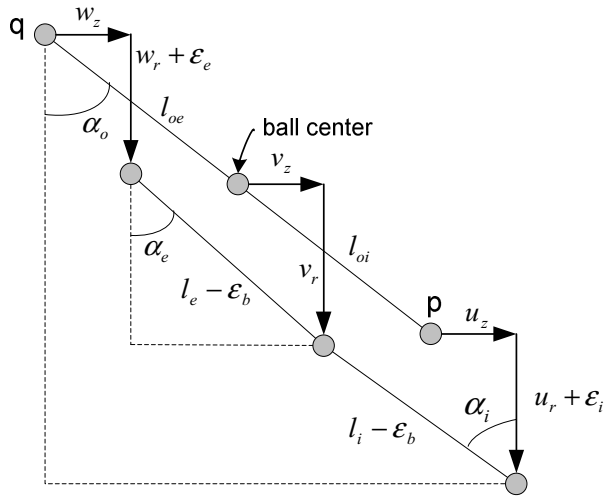


Fig.6.12. Displacements of ball center, inner and outer races including thermal expansion

From the modified Hertzian contact force [16],

$$Q_i = k_i \delta_i^{3/2} \cdot \left( \frac{3}{2} \alpha \dot{\delta}_i + 1 \right) \tag{6.36}$$

$$Q_e = k_e \delta_e^{3/2} \cdot \left( \frac{3}{2} \alpha \dot{\delta}_e + 1 \right) \tag{6.37}$$

For an elliptical contact area, the ball contact stress [17] at the geometric center is

$$\sigma_{i,e} = -\frac{3Q_{i,e}}{2\pi \cdot a_{i,e} b_{i,e}} \tag{6.38}$$

*a*, *b* are the semi-major and semi-minor axes of the projected elliptical area, which are calculated as described in [17].

The increased contact force causes more friction heat generation, the heat source is transferred to the bearing components, and the temperature increase brings more thermal expansion. This feedback loop becomes unstable when the heat generation increases so rapidly that the heat transfer mechanism can not redistribute heat quickly enough and the thermally induced load increases until failure occurs. It is called thermally induced bearing seizure or lockup.

# CHAPTER VII
# OVERALL SYSTEM SIMULATION

This chapter presents the system simulation after a blade loss event of the aircraft gas turbine engine mounted on six rolling element bearings & squeeze film dampers (SFD) with seal rub and enclosed in a flexible housing. The approach being used is to first develop and include a detailed high-fidelity model to capture the structural loads resulting from blade loss, and then use these loads in an overall system model that includes complete structural models of both the engines and aircraft structure. A high fidelity nonlinear ball bearing model and finite element (FE) SFD model is employed in the simulation. The contact stress on the ball is calculated using the ball bearing model and permanent deformation is predicted. The FE SFD determines pressure profile of oil film around SFD journal and calculates damper forces depending on the journal motion and velocity. A bearing thermal model predicts temperature growths in support bearings and oil in SFD. Simulation results including whirl amplitudes of power turbine, bearing contact load and stress, oil pressure in SFD, power loss in bearing and transmissibility.

## 7.1 FE Model of Complete System

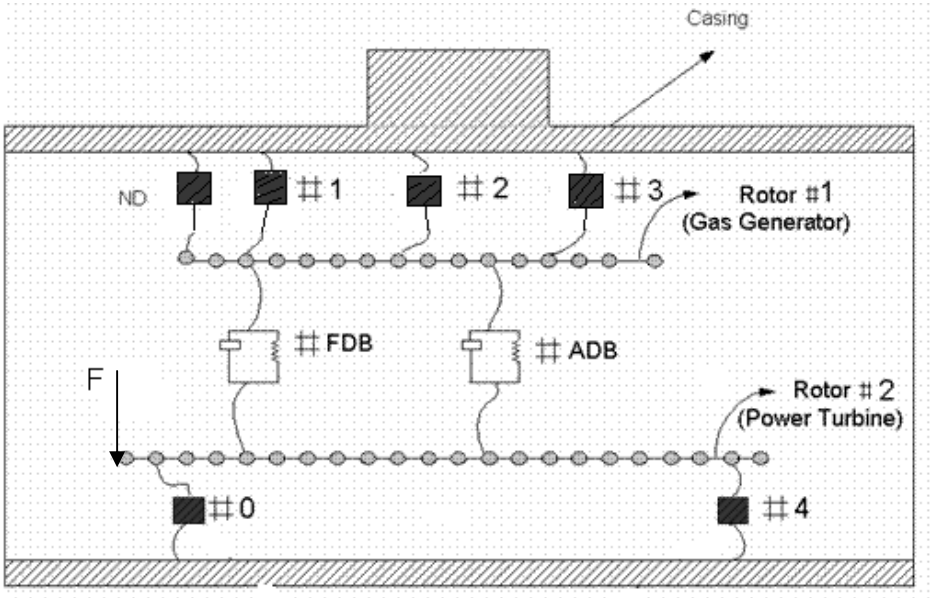


Fig 7.1 Schematic diagram of the full system

Figure 7.1 shows the schematic drawing of the complete system with dual rotors and high fidelity bearings enclosed in a flexible casing. All the bearings to the ground are replaced with high fidelity bearings. Since rolling element bearings have little inherent damping, SFD is employed to reduce the amplitudes of vibration and dynamic force transmitted from the engine. The arrows in the figure indicate a high imbalanced load applied at the blade loss location. The bearing dimension, material characteristics and SFD damper dimension for all the hi-fidelity bearing locations are listed in Table 7.1. A linear stiffness and damper is utilized for the intermediate differential bearings as listed in Table 7.2.

Table 7.1 Specifications of Support Bearings

| **Dimension** | **Brg #0 210J** | **Brg #4 217H** | **Brg ND 114H** | **Brg #1 215H** | **Brg #2 217H** | **Brg #3 219H** |
|---|---|---|---|---|---|---|
| **Geometry:** | | | | | | |
| Bore diameter, [cm] | 5.00 | 8.50 | 7.00 | 7.50 | 8.50 | 9.50 |
| Outside diameter, [cm] | 9.00 | 15.0 | 11.00 | 13.00 | 15.0 | 17.00 |
| Width [cm] | 2.00 | 2.80 | 2.00 | 2.50 | 2.80 | 3.20 |
| Number of balls | 21 | 16 | 18 | 17 | 16 | 15 |
| Diameter of ball [mm] | 8.73 | 20.64 | 12.70 | 17.46 | 20.64 | 24.61 |
| Initial contact angle | 15 | 15 | 15 | 15 | | 15 |
| Axial preload [N] | 800.67 | 1645.8 | 711.71 | 1156.5 | 1645.8 | 2090.7 |
| Number of rows | 1 | 1 | 1 | 1 | 1 | 1 |
| **Material:** | | | | | | |
| Density of ball: [g/cm$^3$] | 7.8 | 7.8 | 7.8 | 7.8 | 7.8 | 7.8 |
| Density of races: [g/cm$^3$] | 7.8 | 7.8 | 7.8 | 7.8 | 7.8 | 7.8 |
| Elastic modulus of ball [GPa] | 208 | 208 | 208 | 208 | 208 | 208 |
| Poisson's ratio of ball | 0.3 | 0.3 | 0.3 | 0.3 | 0.3 | 0.3 |
| Elastic modulus of races [GPa] | 208 | 208 | 208 | 208 | 208 | 208 |
| Poisson's ratio of races | 0.3 | 0.3 | 0.3 | 0.3 | 0.3 | 0.3 |
| **Support system:** | | | | | | |
| Stiffness of centering spring [N/mm] | 5254 | 5254 | 5524 | 5524 | 5524 | 5524 |
| Radius of SFD journal [cm] | 10.0 | 8.0 | 10.0 | 12.5 | 8.0 | 16.0 |
| Length of SFD journal [cm] | 4.0 | 3.2 | 4.0 | 5.0 | 3.2 | 6.4 |

| | | | | | | |
|---|---|---|---|---|---|---|
| Viscosity lubricant [cP] | 70 | 70 | 70 | 70 | 70 | 70 |
| Radial clearance [mm] | 0.635 | 0.635 | 0.635 | 0.635 | 0.635 | 0.635 |

Table 7.2 Stiffness and Damping of Support System

| Bearing No. | Stiffness (N/m) | Damping (N-sec/m) |
|---|---|---|
| FDB | 8.756E07 | 3.502E03 |
| ADB | 8.756E07 | 3.502E03 |

## 7.2 Simulation Results

The system simulation includes the lost blade loadings and the interactions between the rotating turbo machinery and the remainder of the aircraft's structural components. Seal rub is included at the bearing locations #0 and #4 to protect the bearings from permanent damage. The clearance between the rotor and the seal is 0.508 mm (20e-3 in) and that for the SFD is 0.635 mm (25e-3 in). Thus, under high imbalanced load the rotor first rubs against the seal and loses power thereby preventing bearing failure.

The power turbine is spinning at 18,000 rpm while the gas generator at 15,000 rpm. Before the blade loss event occurs, several revolutions of time transient solution under low imbalanced load is performed to show proper status of the motion of the overall system. Sudden unbalanced load of 10,008 N (2250 lb) is then applied at the blade loss location (node #1). Numerical solution is obtained using Newmark Beta method with a fixed time step of 4e-7 sec. The total integration time is 120.1667 sec. Figure 7.2 shows the staggering analysis timeline used for the simulation.

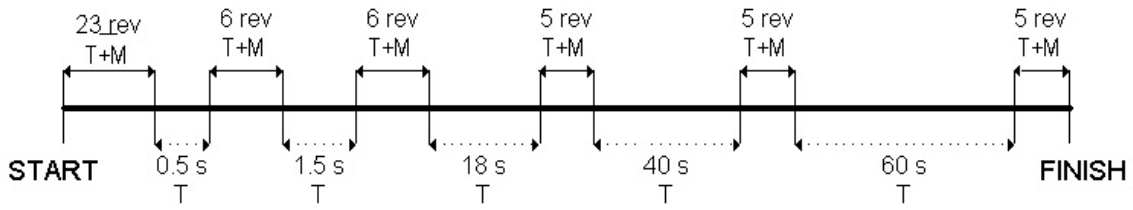


Fig 7.2. Timeline for overall system simulation

Figure 7.3 (a) and (b) shows the transient response in the *y, z* axes and the orbit plot of the power turbine rotor at bearing #1 respectively. When the blade is lost, there is an initial overshoot causing the rotor to rub against the seal. After a couple of revolutions, the amplitude decreases and continues to decrease till it reaches the steady state amplitude of 0.3 mm (o-p). This can be seen clearly in the orbit plot where the first ring shows the rub which is damped out as time progresses.

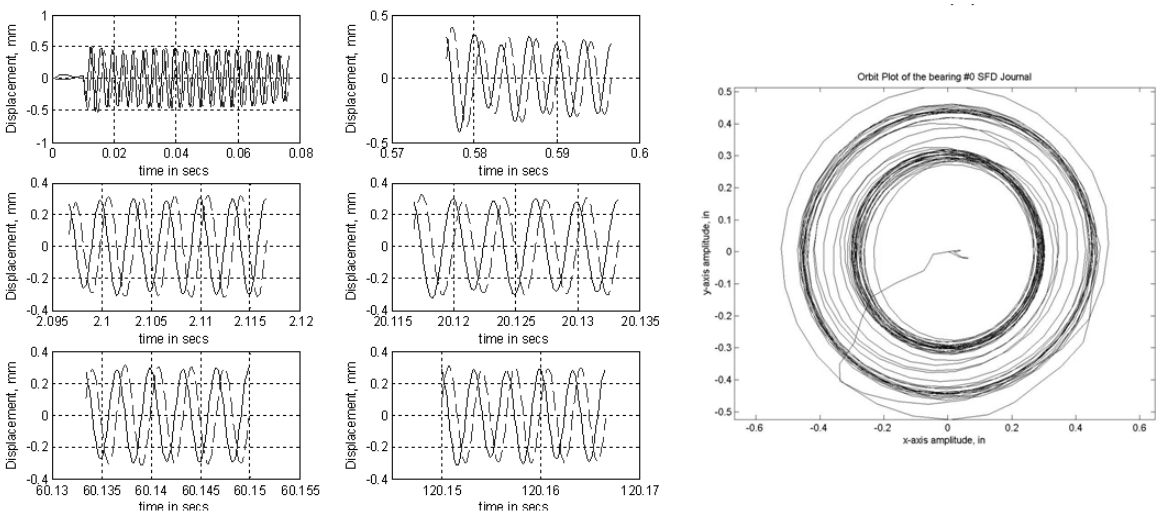


Fig. 7.3 (a) Transient response and (b) orbit plot of brg #0:—, *y*-axis; --, *z*-axis

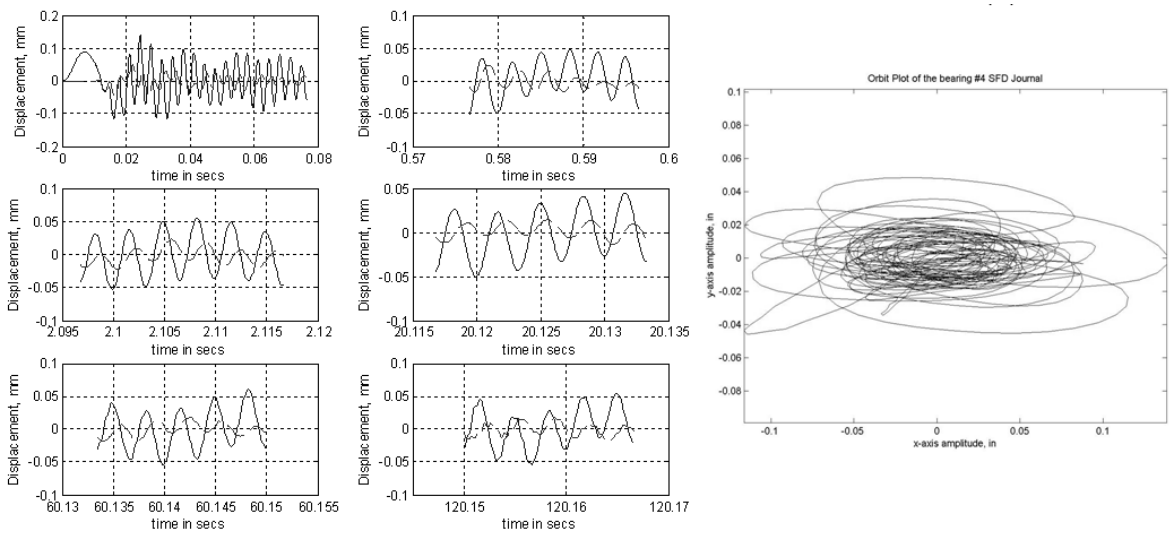


Fig. 7.4 (a) Transient response and (b) orbit plot of brg #4:—, *y*-axis; --, *z*-axis

The transient response of the bearing #4 and the orbit plot are shown in fig. 7.4 (a) and (b) respectively. It can be noticed that the steady state amplitude at bearing #0 is about 6 times greater than that at bearing #4. This is because the unbalanced load is applied very close to bearing #0 while it is 1.37 m (54") away from bearing #4. Figures 7.5, 7.6, 7.7 and 7.8 show the transient response and orbit plots of the gas generator bearings #ND, #1, #2 and #3 respectively. It can be seen that the deflection at these locations is very small and hence no temperature nodes are included. This is done to save computational time. Also, all the other plots at these locations will not be presented here since they are not very significant and comparable to the ones at bearing #4.

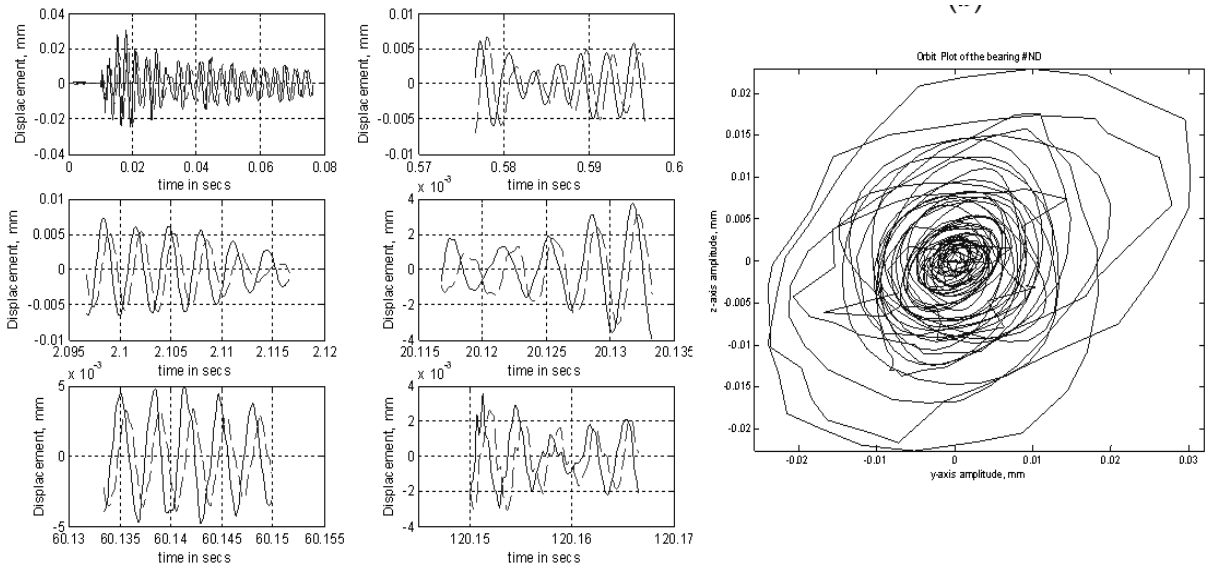


Fig. 7.5 (a) Transient response and (b) orbit plot of brg #ND:—, *y*-axis; --, *z*-axis

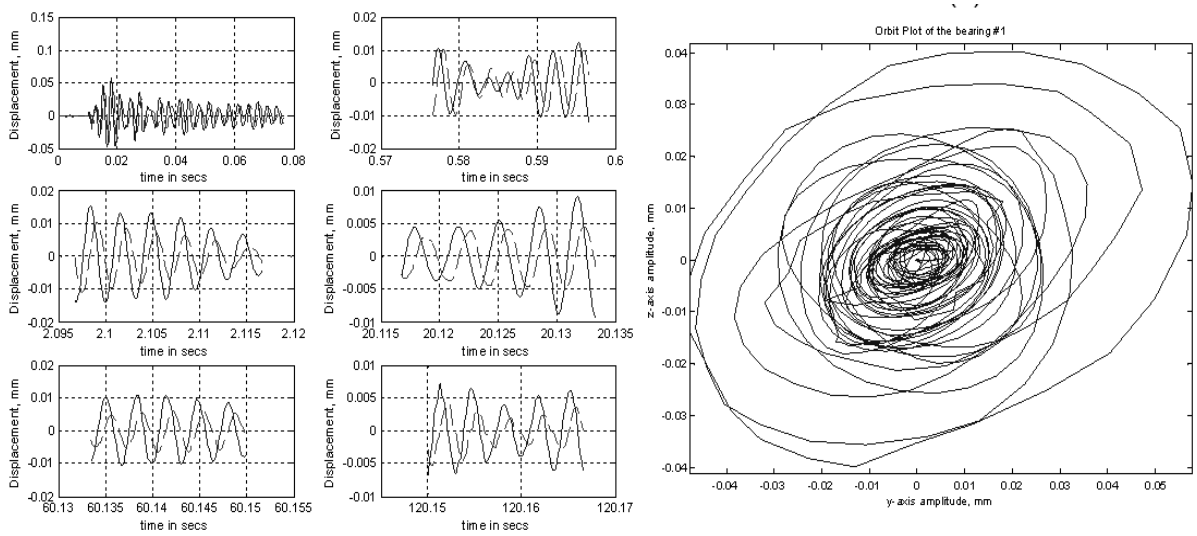


Fig. 7.6 (a) Transient response and (b) orbit plot of brg #1:—, *y*-axis; --, *z*-axis

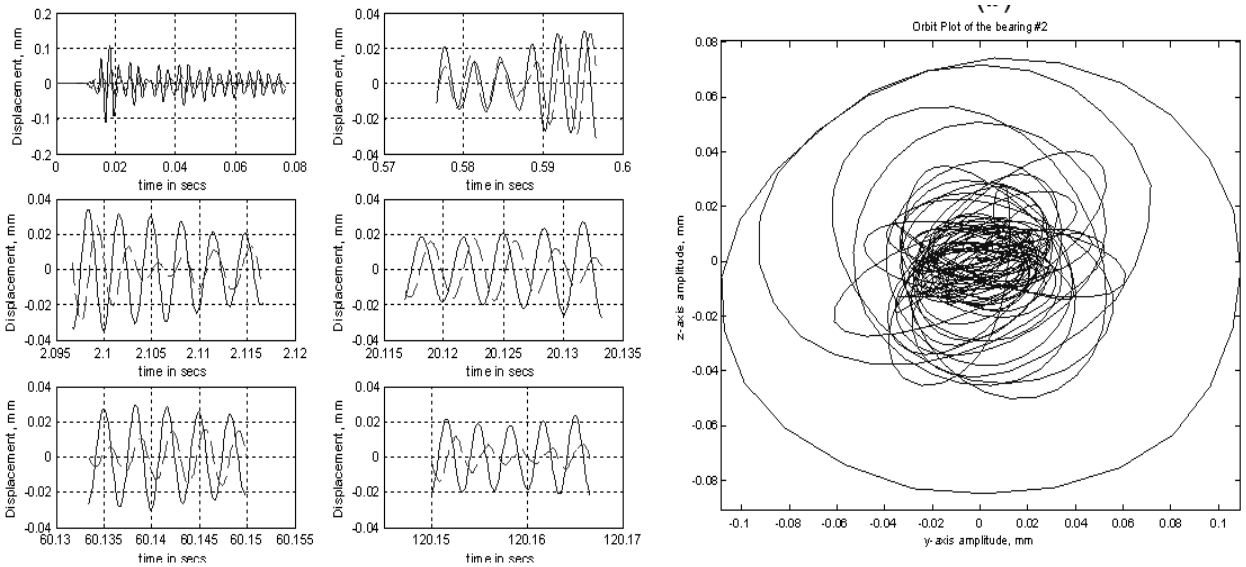


Fig. 7.7 (a) Transient response and (b) orbit plot of brg #2:—, *y*-axis; --, *z*-axis

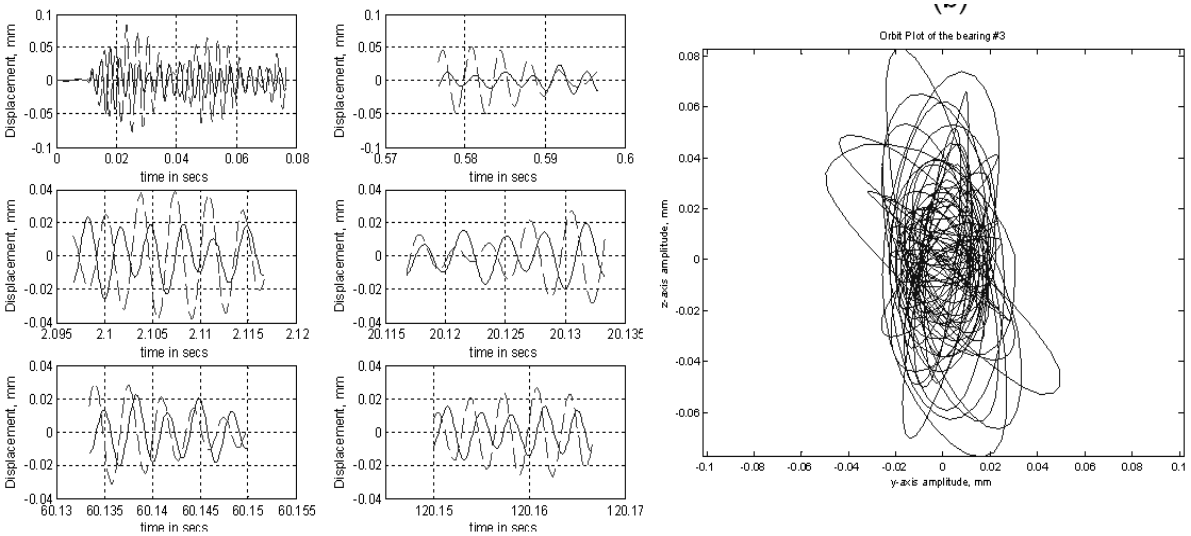


Fig. 7.8(a) Transient response and (b) orbit plot of brg #3: —, *y*-axis; --, *z*-axis

As defined in Chapter IV, transmissibility is the ratio of the force transmitted to the support system to the unbalanced force. Figure 7.9 shows the transmissibility plots at bearings #0 and #4. The transmissibility is very low at bearing #4 while it shoots to a peak value and oscillates around 0.2. The high value of transmissibility is due to the fact that when rub occurs, there is a high contact force applied which causes a large increase

in the SFD force. Thus, the numerator in eqn 4.27 increases tremendously while the imbalanced load in the denominator remains constant. In other words, the excessive non linear film force produced by high eccentricity can make the SFD lock up and cause the increase in transmissibility as shown in fig. 7.9.

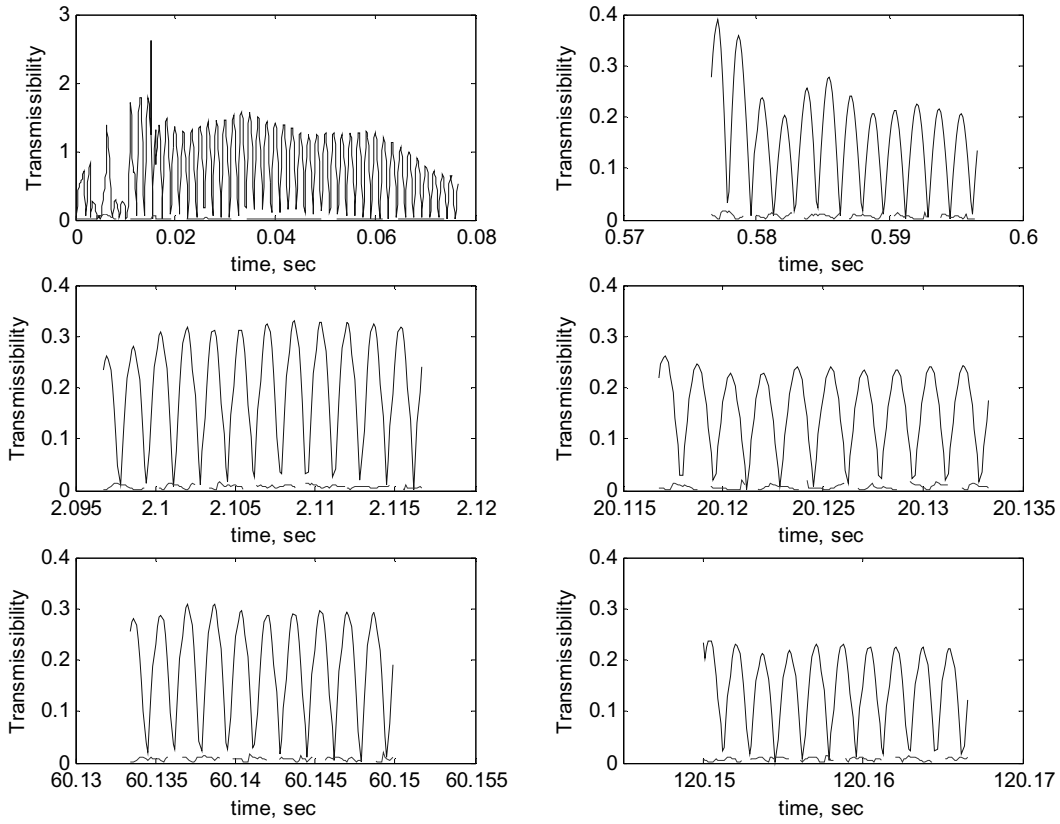


Fig. 7.9 Transmissibility:— brg #0 -- brg #4

Figures 7.10 and 7.11 shows the maximum stress due to compressive contact load at the inner and outer race for the two power turbine bearings respectively. As expected, the stress values peak when rub occurs and then reduces down. Figure 7.12 [17] describes the shake down diagram as applied to bearing stress limits. A cyclically applied load of such magnitude that the material yield stress has been exceeded causes permanent change in the material of bearing rings below rolling contact surfaces. The Shake down limit is one where permanent change occurs with plastic flow of material. The Incipient plastic flow limit is defined as one where no plastic flow occurs. This is the safe region to

prevent bearing damage. A value of 0.0001D permanent deformation limit where D is the ball diameter. For AISI 52100 (material for bearing rings), the yield stress limit is 260 ~ 290 kpsi. By comparing the stress plots with fig. 7.12, it is clear that bearing #0 undergoes permanent deformation when rub occurs whereas bearing #4 is well below the danger limit.

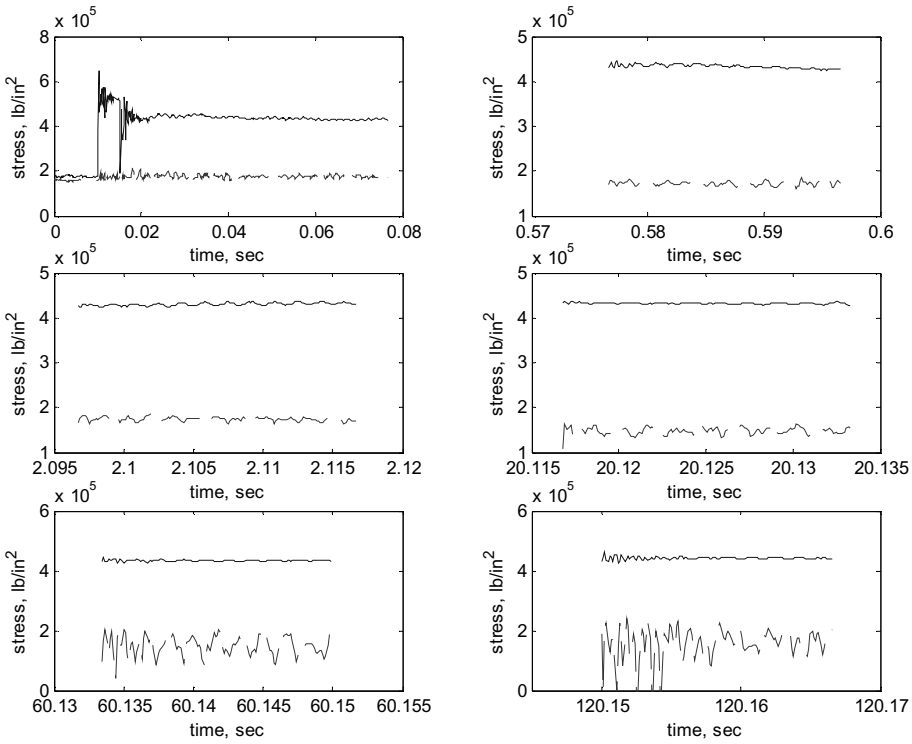


Fig. 7.10 Maximum contact stress at inner race :— brg #0 -- brg #4

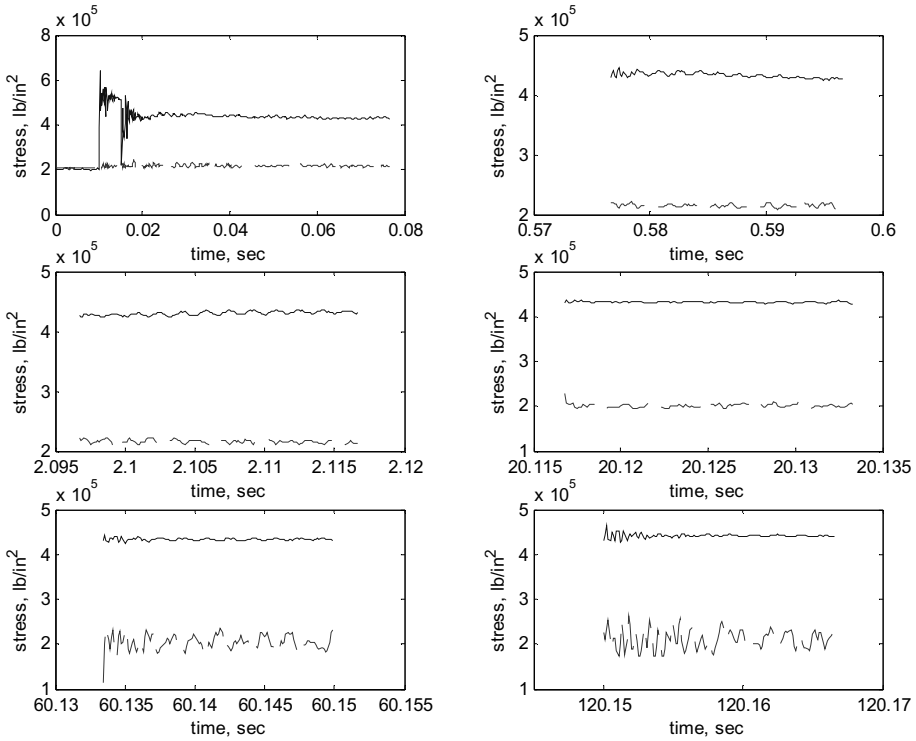


Fig. 7.11 Maximum contact stress at outer race :— brg #0 -- brg #4

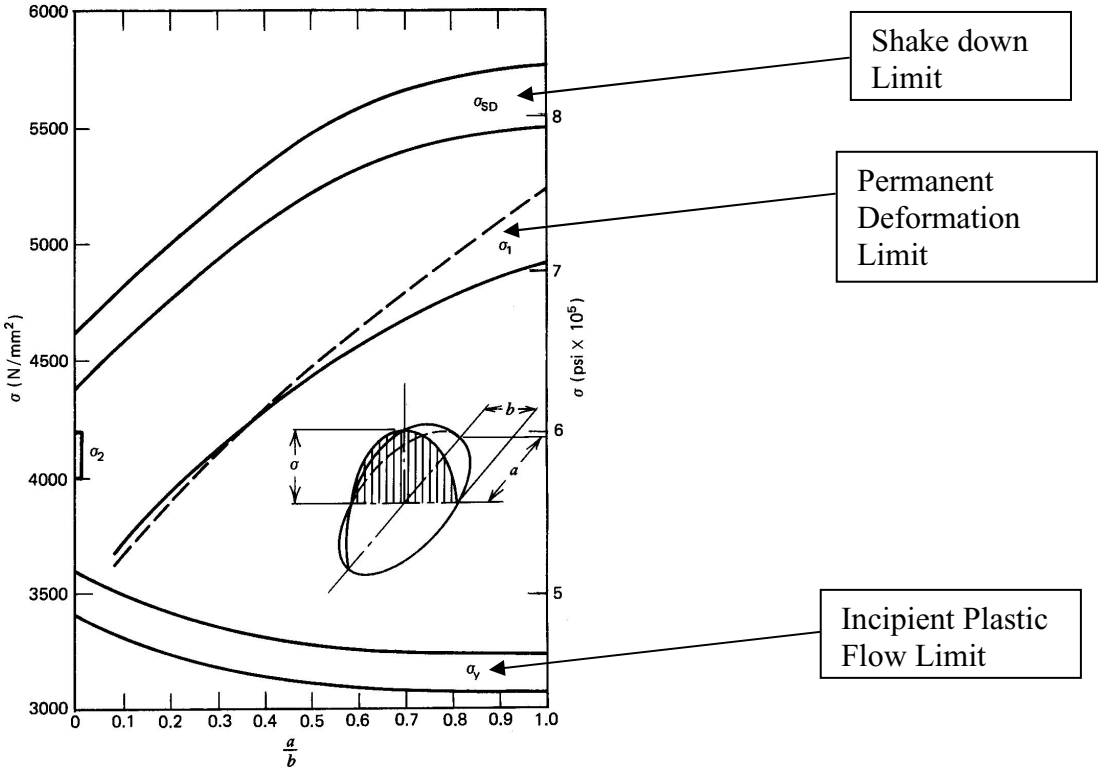


Fig. 7.12 Shakedown Diagram for Bearing Stress limits [17]

Figures 7.13 and 7.14 show the maximum and minimum pressure in the FE SFD. A supply pressure of 30 psi is used. Due to the high eccentricity, the maximum pressure at bearing #0 is much higher than that at the bearing #0. Here, zero pressure indicates oil cavitation. It is noticed that cavitation occurs in bearing #0 as soon as the blade loss event occurs till the end of the simulation while there is no oil cavitation at all in bearing #4.

Figure 7.15 shows the heat loss in the oil. This has a high value during the rub phase and reduces as the SFD journal reaches steady state at bearing #0. It is negligibly small at bearing #4. Figure 7.16 shows the power loss in the bearing. Even though there is some initial variation during the transient phase, it reaches a constant value after steady state is reached. This phenomenon is exploited in the Staggering Analysis Scheme as explained in Chapter V.

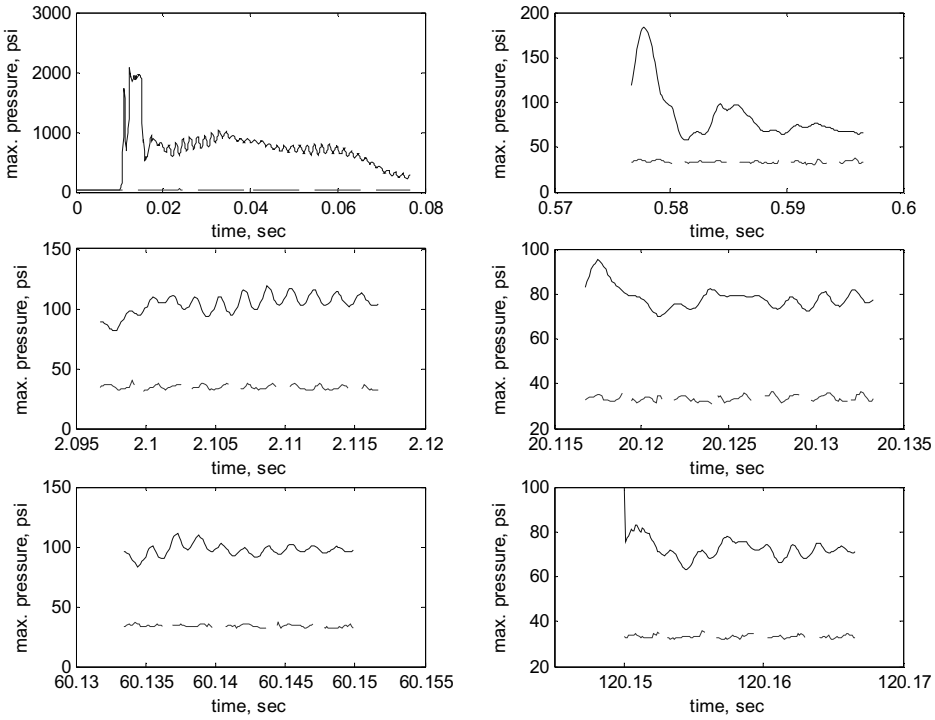


Fig. 7.13 Maximum pressure at:— brg #0 -- brg #4

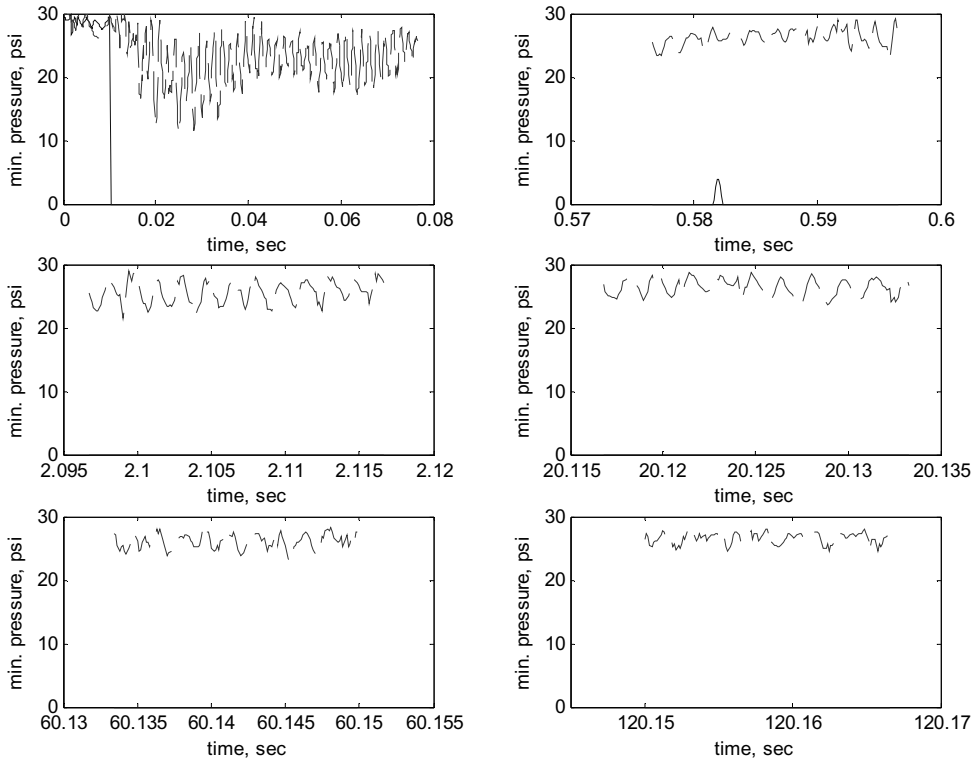


Fig. 7.14 Minimum pressure at:— brg #0 -- brg #4

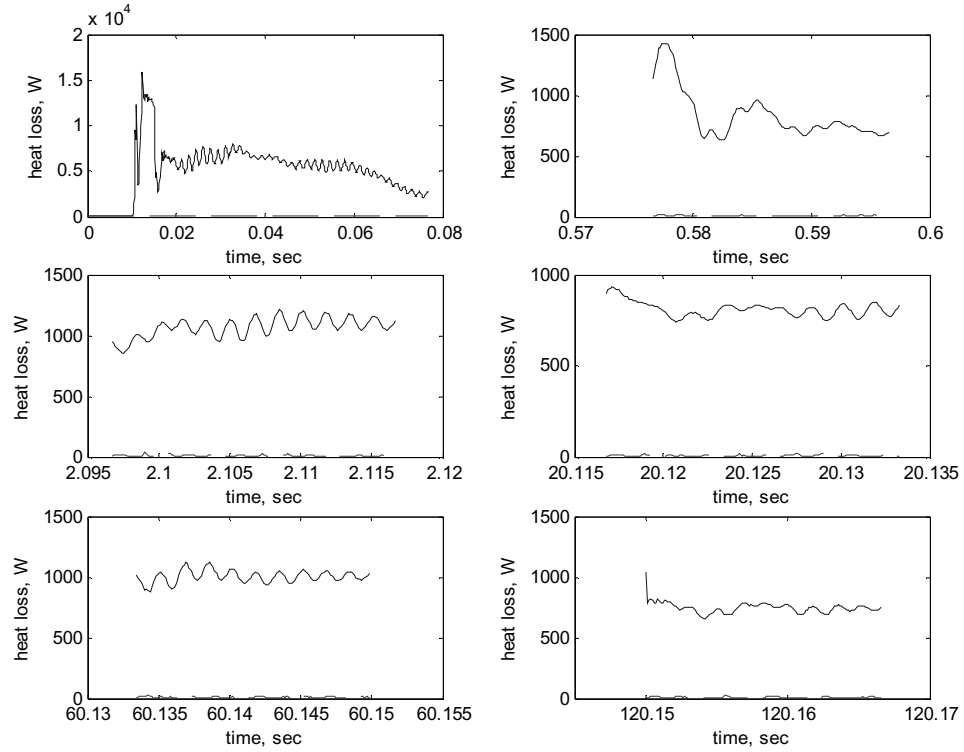


Fig. 7.15 Heat loss at:— brg #0 -- brg #4

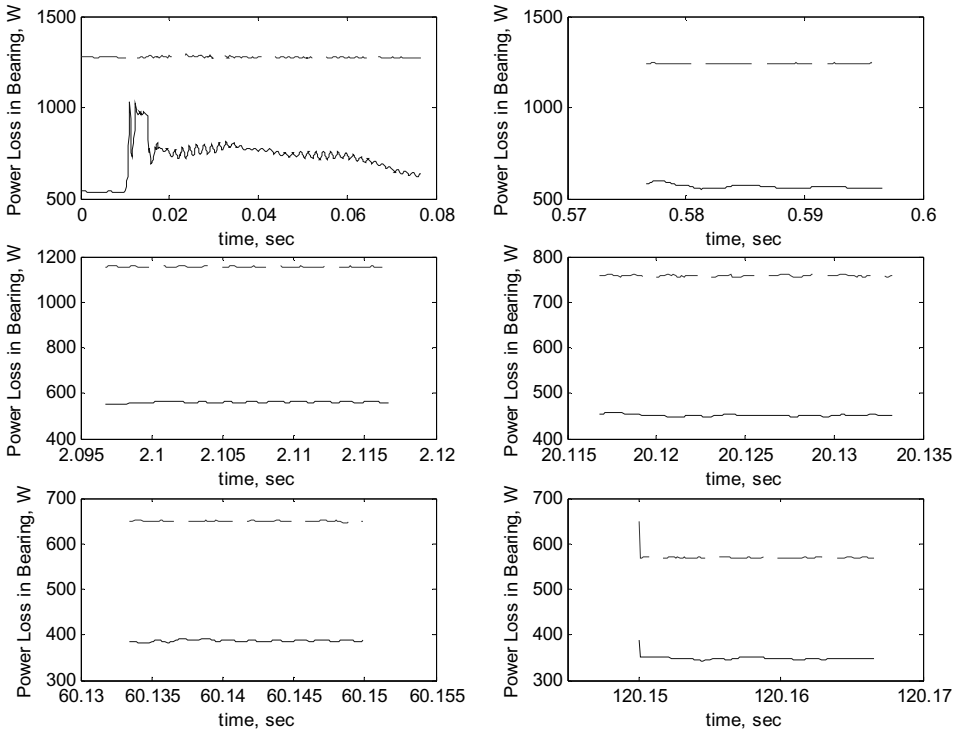


Fig. 7.16 Bearing power loss at:— brg #0 -- brg #4

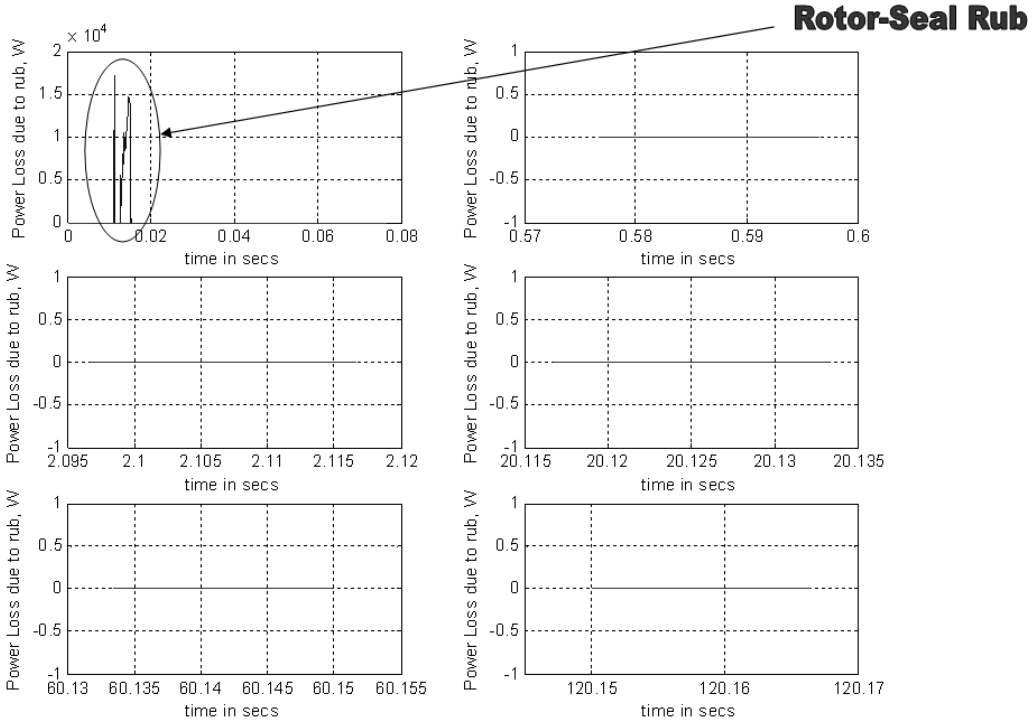


Fig. 7.17 Power loss due to rub at:— brg #0 -- brg #4

Figure 7.17 shows the power loss at the bearings #0 and #4 due to rub. It is clear from these plots that rub occurs at bearing #0 only during the initial transient phase. There is no rub at all at bearing #4 location throughout the analysis.

Figures 7.18 and 7.19 show the temperature plots for 120 sec at the bearing inner race, bearing ball, bearing outer race and oil film respectively. The inner race, the balls and the outer race reach about 200 F after 120 sec at bearing #0 and about 160 F at bearing #4. The final oil temperature is 155 F at bearing #0 and 105 F at bearing #4. It can also be observed the temperature plots are not smooth but have edges at the end of thermal only runs. This is because of the staggering scheme. Thus, short thermo-mechanical runs need to be done between the thermal only runs to help correct the error in the predicted temperature. This effect is exaggerated in the temperature plot of bearing #0. There is a sharp rise and fall in temperature initially with exaggerated drops. The oil is very sensitive and hence its temperature increases or falls drastically. Thus, the initial kink can be accounted for the high power loss at the rub phase. Even after steady state is reached, there are some sharp drops in temperature. This could be because a higher power loss is predicted and applied to the thermal only phase which is then corrected in the thermo-mechanical phase.

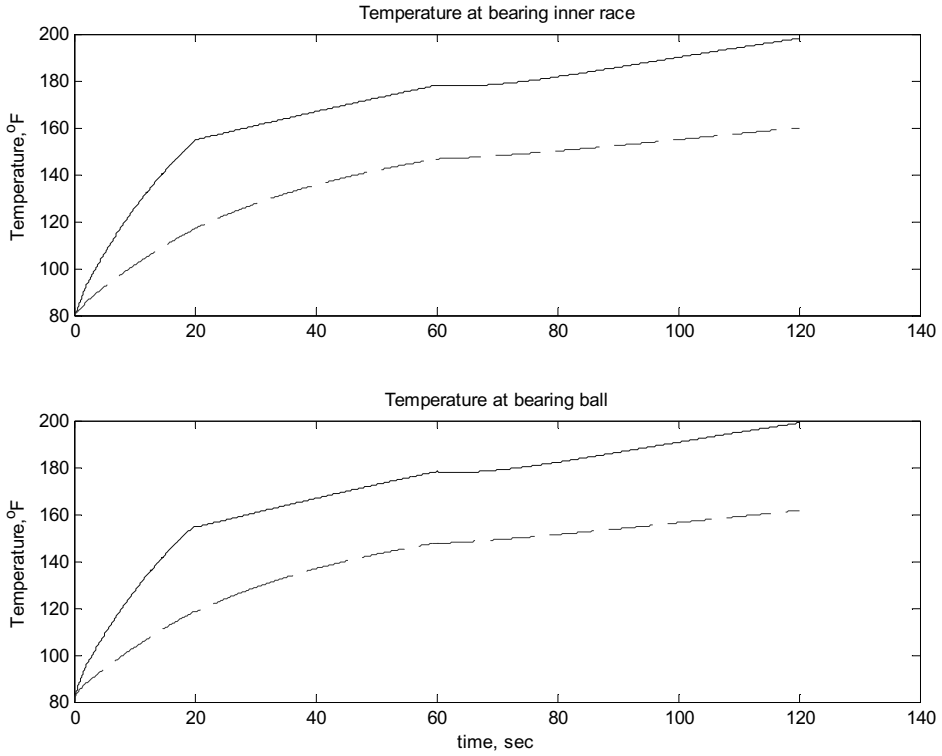


Fig. 7.18 Temperature of bearing inner race and bearing ball at: — brg #0 -- brg #4

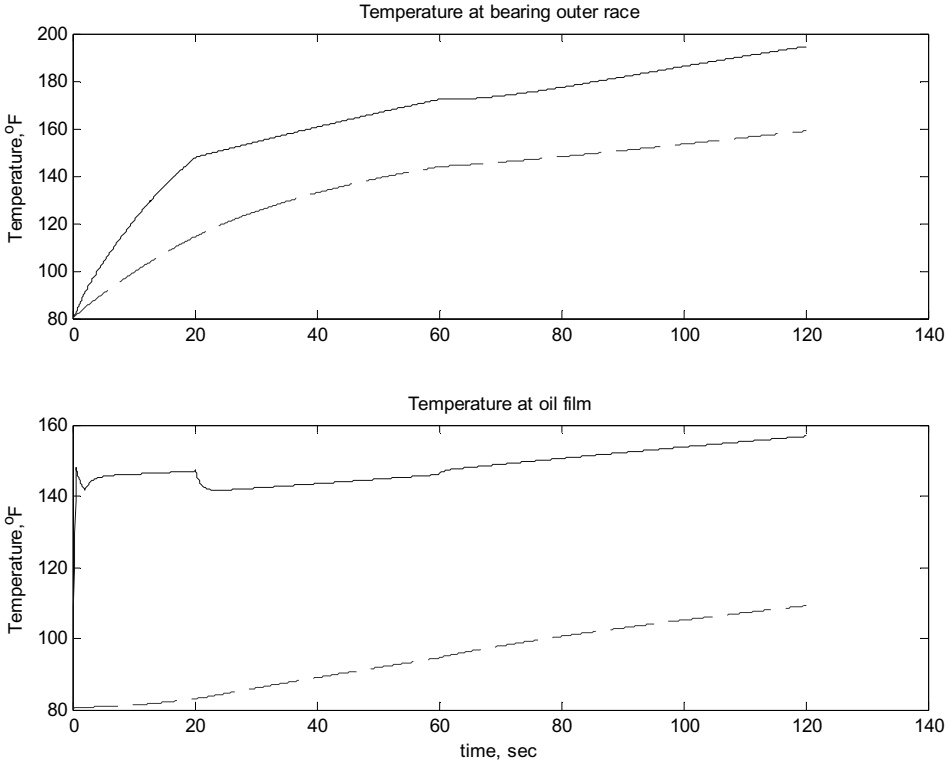


Fig. 7.19 Temperature of bearing outer race and oil film at: — brg #0 -- brg #4

# CHAPTER VIII
# CONCLUSIONS AND FUTURE WORK

In this thesis, an efficient algorithm for blade loss simulations is developed and applied to a large order rotor dynamics problem. Firstly, preliminary structural analyses are conducted to better understand the model. Then, blade loss simulations for the dual-rotor aircraft gas turbine engine are conducted using the MTA method and some standard modal based solution algorithms to verify the effectiveness of the method. The simulation results show that the SFD damps out the transient whirl amplitude of the power turbine rotor up to the unbalanced force 5694 N but the steady state whirl amplitudes after the unbalanced force 5694 N enormously increase because the SFD with high eccentricity locks up the rotor support system. This phenomenon is also shown in the maximum contact loads, which increase over 25 times higher than the contact loads at 5694 N, and in the transmissibility, which increases from 0.26 to 1.1. The maximum contact stress also increases proportionally with the 1/3 power of the contact load as the unbalanced force increases. The oil film cavitation at the bearing #4 close to the imbalanced load location occurs at the unbalanced force of 5694 N, while the cavitation at bearing #0 occurs at the unbalanced force of 8541 N.

In Chapter V, the Staggered Analysis scheme is developed and verified. This method is shown to have an efficiency of 4 times higher than the MTA method alone and loss in accuracy of less than 5%. The method is then applied to the overall system with six high-fidelity bearings, temperature model, seal rub and a flexible housing to simulate a blade-out event. A 120 sec simulation for this model using the new method requires only 8 hrs on a P3, 930 MHz, 512 MB RAM, Intel processor. The orbit plots clearly show that when the blade is lost, there is an initial overshoot causing the rotor to rub against the seal. After a couple of revolutions, the amplitude decreases and continues to decrease till it reaches the steady state amplitude of 0.3 mm (o-p). This is reflected in the transmissibility, stress, power / heat loss and the pressure plots. The stress plots are compared with the bearing stress limit plot to show that permanent deformation occurs in bearing #0 due to the initial overshoot. It can be observed in the temperature plots that the

staggering scheme is effective in that the errors that are developed in the thermal only phase are corrected in the thermo-mechanical phase.

The expected future works can be addressed as follows:

- Include the wind milling effect to help avoid excess vibration levels caused due to it.
- Conduct a blade loss test and corroborate test data with simulation results.
- Develop improved rotor structural models for thin walled, shell type rotor sections, i.e. axi-symmetric models with non-axisymmetric deformation.
- Install and simulate Magnetic Bearings.
- Develop GUI for the advanced TAMU code.

# REFERENCES


1. R.L. Ruhl, and J. F. Booker, 1972 *ASME Transactions* **17***,* 126–132. A Finite Element Model for Distributed Parameter Turborotor System.
2. E.S. Zorzi, and H.D. Nelson, 1977 *Journal of Engineering for Power* **8***,* ASME Transactions, 71–76. Finite Element Simulation of Rotor Bearing Systems with Internal Damping.
3. W.C. Hurty, 1965 *AIAA Journal* **3**, 678–685. Dynamic Analysis of Structural Systems Using Component Modes.
4. R.R Craig, and M.C.C. Bampton, 1968 *AIAA Journal* **6***,* 1313–1319. Coupling of Substructures for Dynamic Analysis.
5. J.M. Dickens, J.M. Nakagawa, and M.J. Wittbrodt, 1997 *Computers & Structures* **62,** 985-998. A Critique of Mode Acceleration and Modal Truncation Augmentation Methods for Modal Response Analysis.
6. J.M. Dickens and K.V. Pool, 1992 *Computers & Structures* **45**, 685-696. Modal Truncation Vectors and Periodic Time Domain Analysis Applied to a Cyclic Symmetry Structure.
7. R.R. Craig Jr., 1981 *Structural Dynamics*. Wiley, New York.
8. M.J. Stallone, V. Gallardo, A.F. Storace, L.J.Bach, G. Black, et al., 1983 *AIAA Journal* **21,** 1134-1138. Blade Loss Transient Dynamic Analysis of Turbomachinery.
9. M. Alam and H.D. Nelson 1985 *ASME Eng. for Gas Turbines & Power* **107,** 197-204. A Blade Loss Response Spectrum for Flexible Rotor Systems.
10. G. Sun, 2003 Ph.D. Dissertation, Texas A&M University, Texas. A High Fidelity Ball Bearing and Damper Model Including Thermal Effects for Magnetic Suspension Auxiliary Service and Blade Loss Simulation.
11. J.S. Przemieniecki, 1968 *Theory of Matrix Structural Analysis*. McGraw-Hill, New York.
12. K. Rouch, 1977 Ph.D. Dissertation, Marquette University, Wisconsin. Finite Element Analysis of Rotor Bearing Systems with Matrix Reduction.
13. D. Li, 1978 Ph.D. Dissertation, University of Virginia, Virginia. Dynamic Analysis of Complex Multi-Level Flexible Rotor Systems.

14. G. Sun, N. Kaushik, A.B. Palazzolo, A.J. Provenza, C. Lawrence, et al., 2003 *Proceedings of ASME International 19th Biennial Conference on Mechanical Vibration and Noise*. Efficient Algorithm for Blade Loss Simulation Using High Fidelity Ball Bearings and Damper Model.
15. J.N. Reddy, 1993 *An Introduction to the Finite Element Method*. McGraw-Hill, New York.
16. K.H. Hunt, F.R.E. Crossley, 1975 *Transactions of the ASME* **8***,* 440-445. Coefficient of Restitution Interpreted as Damping in Vibroimpact.
17. T.A. Harris , 1984 *Rolling Bearing Analysis*. Wiley, New York.
18. A. Palazzolo, 2002 *Lecture Notes for Mechanical Vibrations*. Texas A&M University, Texas.
19. *ANSYS Training Manual 2001* **1,** ANSYS Inc., Canonsburg, Pennsylvania.

# APPENDIX A

## A.1 Newmark – Beta Numerical Integration Method

This method has gained considerable popularity among vibration analysts and assumes that the acceleration is approximately constant within any time step.

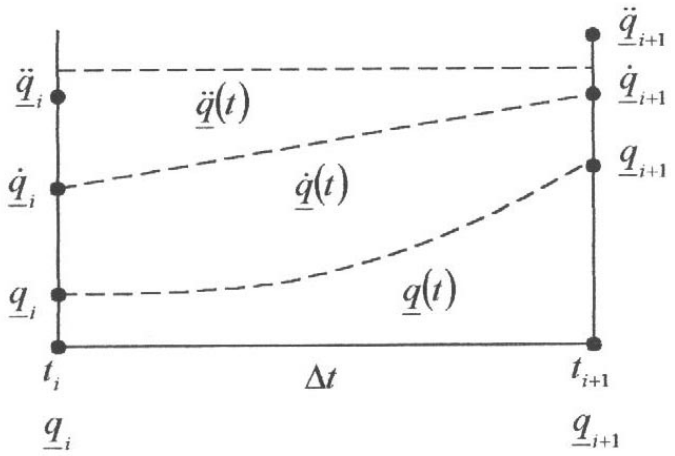


Fig A.1 Discretized time and response variables for newmark beta method [18]

A reasonable assumption for the variation of $\{\ddot{q}\}$ between $t_i$ and $t_{i+1}$ is that it is the constant vector

$$\{\ddot{q}(t)\} = \frac{\ddot{q}_i + \ddot{q}_{i+1}}{2} \qquad \text{A.1}$$

Newmark generalized this expression to the form

$$\ddot{q} = (1-\delta)\ddot{q}_i + \delta\ddot{q}_{i+1}, \quad t_i < t < t_{i+1} \qquad \text{A.2}$$

Note that Eqn. A.2 reduces to A.1 if δ=0.5. Integration of Eqn. A.2 yields

$$\dot{q}_{i+1} = \dot{q}_i + [(1-\delta)\ddot{q}_i + \delta\ddot{q}_{i+1}]\Delta t \qquad \text{A.3}$$

Integration again yields

$$q_{i+1} = q_i + \dot{q}_i\Delta t + \frac{\Delta t^2}{2}[(1-\delta)\ddot{q}_i + \delta\ddot{q}_{i+1}] \qquad \text{A.4}$$

Newmark generalized this result by replacing δ/2 by a constant α independent of δ. The Newmark approximations then become

$$\begin{aligned}
&\ddot{q} = (1-\delta)\ddot{q}_i + \delta\ddot{q}_{i+1}, t_i < t < t_{i+1} \\
&\dot{q}_{i+1} = \dot{q}_i + [(1-\delta)\ddot{q}_i + \delta\ddot{q}_{i+1}]\Delta t \\
&q_{i+1} = q_i + \dot{q}_i\Delta t + [(\frac{1}{2}-\alpha)\ddot{q}_i + \alpha\ddot{q}_{i+1}]\Delta t^2
\end{aligned} \qquad \text{A.5}$$

The recommended values for δ and α are

$$\delta = \frac{1}{2}; \alpha = \frac{1}{4} \qquad \text{A.6}$$

for which eqns. A.5 become

$$\begin{aligned}
&\dot{q}_{i+1} = \dot{q}_i + (\ddot{q}_i + \ddot{q}_{i+1})\frac{\Delta t}{2} \\
&q_{i+1} = q_i + \dot{q}_i\Delta t + (\ddot{q}_i + \ddot{q}_{i+1})\frac{\Delta t^2}{4}
\end{aligned} \qquad \text{A.7}$$

Consider the general system equilibrium equation at time $t_{i+1}$

$$M\ddot{q}_{i+1} + C\dot{q}_{i+1} + Kq_{i+1} = f(t_{i+1}) + g(t_{i+1}, q_i, \dot{q}_i) \qquad \text{A.8}$$

This equation has three unknowns at time $t_{i+1}$. Assume that these quantities are known at time $t_i$ and use eqn. A.5 to eliminate $\dot{q}_{i+1}$ and $\ddot{q}_{i+1}$ from Eqn. A.8. From the 3rd equation in A.5

$$\ddot{q}_{i+1} = \frac{1}{\alpha\Delta t^2}q_{i+1} - \frac{1}{\alpha\Delta t^2}q_i - \frac{1}{\alpha\Delta t}\dot{q}_i + (1-\frac{1}{2\alpha})\ddot{q}_i \qquad \text{A.9}$$

Substitute this result into the 2nd equation of A.5

$$\dot{q}_{i+1} = -\frac{\delta}{\alpha\Delta t}q_i + (-\frac{\delta\Delta t}{2\alpha} + \Delta t)\ddot{q}_i + \frac{\delta}{\alpha\Delta t}q_{i+1} + (1-\frac{\delta}{\alpha})\dot{q}_i \qquad \text{A.10}$$

Substitute A.9 and A.10 into A.8 to eliminate the $\dot{q}_{i+1}$ and $\ddot{q}_{i+1}$ terms and solve for $q_{i+1}$ to obtain

$$\begin{aligned}
(\frac{1}{\alpha\Delta t^2}M + \frac{\delta}{\alpha\Delta t}C + K)q_{i+1} &= f(t_{i+1}) + g(t_{i+1}, q_i, \dot{q}_i) \\
&+ M[\frac{1}{\alpha\Delta t^2}q_i + \frac{1}{\alpha\Delta t}\dot{q}_i + (\frac{1}{2\alpha}-1)\ddot{q}_i] \\
&+ C[\frac{\delta}{\alpha\Delta t}q_i + (\frac{\delta}{\alpha}-1)\dot{q}_i + (\frac{\delta\Delta t}{2\alpha}-\Delta t)\ddot{q}_i]
\end{aligned} \qquad \text{A.11}$$

# APPENDIX B

## B.1 SOLID45 Element – 3D Structural Solid

SOLID45 is used for the three-dimensional modeling of solid structures. The element is defined by eight nodes having three degrees of freedom at each node: translations in the nodal x, y, and z directions. The element has plasticity, creep, swelling, stress stiffening, large deflection, and large strain capabilities.

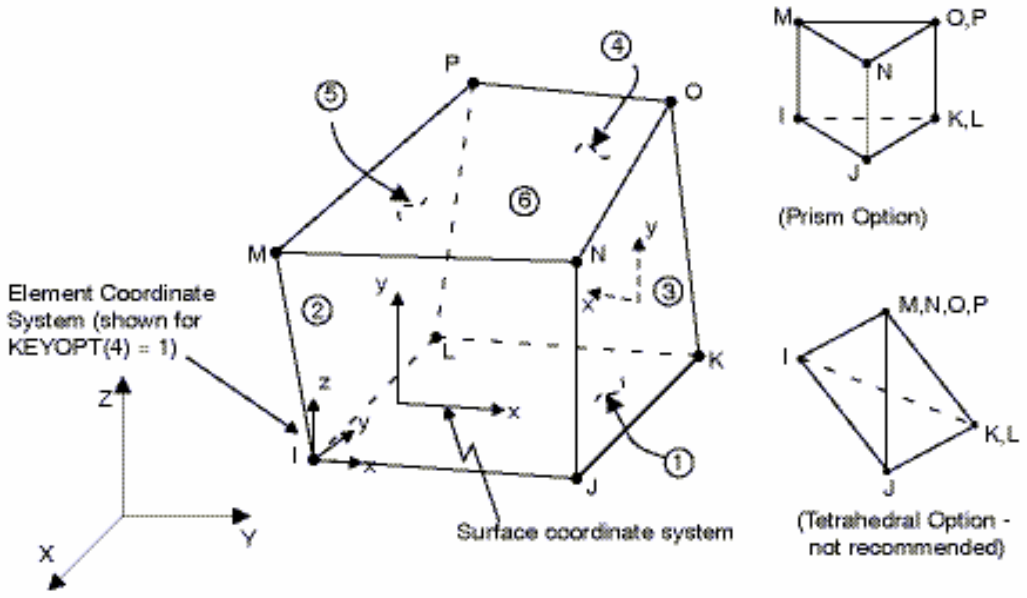


Fig. B.1. SOLID45 3-D structural solid [19]

The geometry, node locations, and the coordinate system for this element are shown in Fig. B.1. The element is defined by eight nodes and the orthotropic material properties. Orthotropic material directions correspond to the element coordinate directions.

Pressures may be input as surface loads on the element faces as shown by the circled numbers on Fig. B.1. Positive pressures act into the element. Temperatures and fluences may be input as element body loads at the nodes.

## B.2 BEAM4 Element – 3D Elastic Beam

BEAM4 is a uniaxial element with tension, compression, torsion, and bending capabilities. The element has six degrees of freedom at each node: translations in the nodal x, y, and z directions and rotations about the nodal x, y, and z axes. Stress stiffening and large deflection capabilities are included. A consistent tangent stiffness matrix option is available for use in large deflection (finite rotation) analyses.

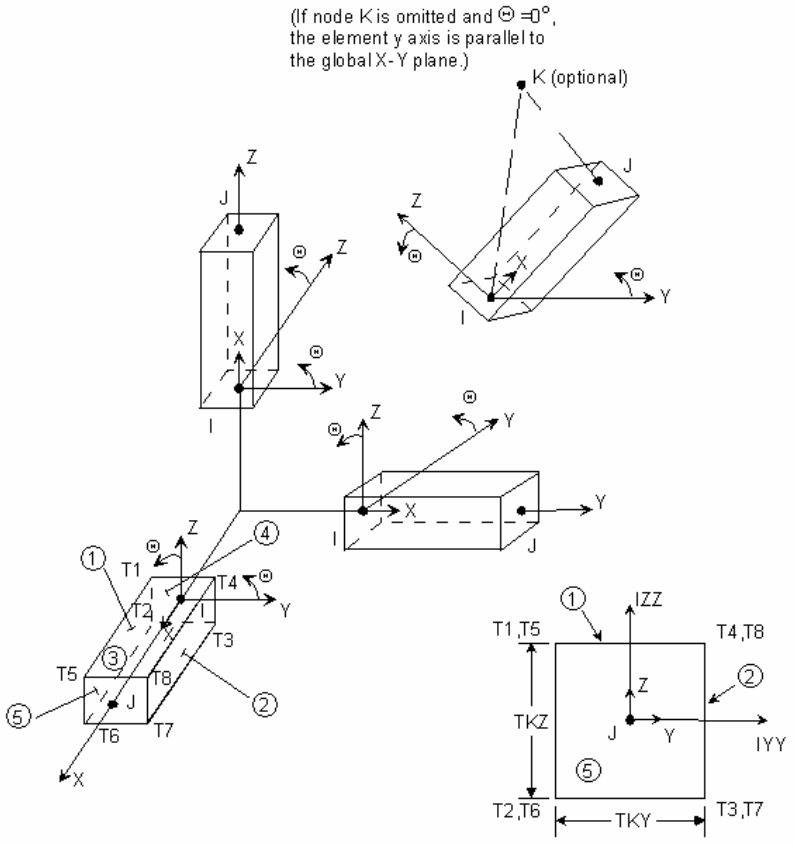


Fig. B.2. BEAM4 3-D elastic beam [19]

The geometry, node locations, and coordinate systems for this element are shown in Fig. B.2. The element is defined by two or three nodes, the cross-sectional area, two area moments of inertia (IZZ and IYY), two thicknesses (TKY and TKZ), an angle of orientation (θ) about the element x-axis, the torsional moment of inertia (IXX), and the material properties. If IXX is not specified or is equal to 0.0, it is assumed equal to the polar moment of inertia (IYY+IZZ).

## B.3 COMBIN14 Element – Spring Damper

COMBIN14 has longitudinal or torsional capability in one, two, or three dimensional applications. The longitudinal spring-damper option is a uniaxial tension-compression element with up to three degrees of freedom at each node: translations in the nodal x, y, and z directions. No bending or torsion is considered. The torsional spring-damper option is a purely rotational element with three degrees of freedom at each node: rotations about the nodal x, y, and z axes. No bending or axial loads are considered. The spring-damper element has no mass.

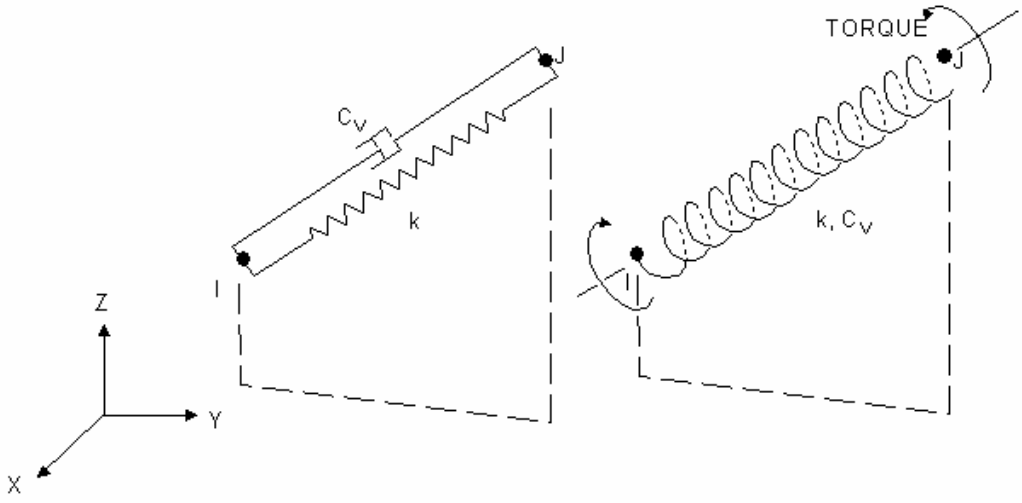


Fig. B.3 COMBIN14 spring-damper [19]

The geometry, node locations, and the coordinate system for this element are shown in Fig. B.3. The element is defined by two nodes, a spring constant (k) and damping coefficients $(c_v)_1$ and $(c_v)_2$. The damping capability is not used for static or undamped modal analyses. The longitudinal spring constant should have units of Force/Length, the damping coefficient units are Force*Time/Length. The torsional spring constant and damping coefficient have units of Force*Length/Radian and Force*Length*Time/Radian, respectively. For a two-dimensional axisymmetric analysis, these values should be on a full 360° basis.

# VITA

Nikhil Kaushik Parthasarathy was born on February 10, 1979 in Bombay, India. After graduating from Bangalore University (Bangalore, India) in December 2000, he entered the graduate program at the Mechanical Engineering Department in Texas A&M University (College Station, Texas) in August 2001. He has been working as a graduate research assistant in the Vibration Control and Electromechanics Lab under the supervision of Dr. Alan Palazzolo. He can be reached at the following address:

1505, Park Place, Apt 6,

College Station, TX 77840.